

**FREQUENCY DOMAIN TRANSMISSION LINE  
MATRIX METHOD AND ITS APPLICATIONS  
TO ELECTROMAGNETIC ANALYSIS**

by

Jifu Huang  
B.S., Southeast University, 1982  
M.S., Southeast University, 1987

A Dissertation Submitted in Partial Fulfillment of the  
Requirements for the Degree of

**DOCTOR OF PHILOSOPHY**

in the Department of Electrical and Computer Engineering

We accept this dissertation as conforming to the required standard

---

Dr. R. Vahldick, Supervisor (Dept. of Elec. & Comp. Eng.)

---

Dr. J. Bornemann, Dept. Member (Dept. of Elec. & Comp. Eng.)

---

Dr. S. Stuchly, Dept. Member (Dept. of Elec. & Comp. Eng.)

---

Dr. D. Oleskv. Outside Member (Dept. of Comp. Sci.)

---

Dr. P. Russer, External Examiner (Technical Univ. of Munich)

© JIFU HUANG, 1995  
University of Victoria

All rights reserved. Dissertation may not be reproduced in whole or in part, by  
photocopy or other means, without the permission of the author.

Supervisor: Dr. R. Vahldieck

## ABSTRACT

The finite difference time-domain (FDTD) method and the transmission line matrix (TLM) method are the two best known time-domain numerical techniques for modelling electromagnetic fields. Both algorithms provide time-domain as well as frequency-domain data. The latter is obtained from a Fourier transform of the time-domain impulse response. To achieve accurate frequency-domain data, some applications require long time iterations before a Fourier transform can be applied. This can be a problem when the computation time becomes excessive. In this case frequency-domain methods may be more suitable. Within the framework of the finite difference method one can always choose between the frequency-domain finite difference (FD) method and its time-domain (FDTD) counterpart without leaving the framework of the finite difference method. In the TLM method this was not possible until recently. In [16] a frequency-domain TLM (FDTLM) algorithm was introduced based on the time-domain TLM symmetrical condensed node. The new approach operates entirely in the frequency-domain eliminating the time iterative algorithm of the TLM method and establishing a duality between the time- and frequency-domain TLM method.

In this thesis the concept of the FDTLM method is further developed. While the first approach for the FDTLM was based on the time-domain symmetrical condensed node (SCN), it is shown in this thesis that the FDTLM nodes can be derived directly in the frequency-domain. A set of new 3D condensed nodes are established and their accuracy compared to other numerical techniques. Subsequently the nodes are applied to cylindrical coordinates.

Based on the symmetry properties of the characteristic admittance SCN, a novel decoupling procedure is introduced which makes it possible to represent the 12X12 node scattering matrix by two 6X6 scattering matrices. This step reduces the matrix size significantly and leads to a significantly faster algorithm.

Finally, the concept of the intrinsic scattering matrix is discussed for the case of 2D and 3D discontinuities. Based on a novel S-parameter extraction technique, S-parameters for a variety of planar, rectangular and circular waveguide discontinuities are computed and where possible compared with data from other numerical techniques and/or measurements to verify the accuracy of this new approach. In most cases very good agreement was found.

**Examiners:**

---

**Dr. R. Vahidieck, Supervisor (Dept. of Elec. & Comp. Eng.)**

---

**Dr. J. Bornemann, Dept. Member (Dept. of Elec. & Comp. Eng.)**

---

**Dr. S. Stuchly, Dept. Member (Dept. of Elec. & Comp. Eng.)**

---

**Dr. D. Olesky, Outside Member (Dept. of Comp. Sci.)**

---

**Dr. P. Russer, External Examiner (Technical Univ. of Munich)**

## Table of Contents

<b>Abstract</b>	<b>ii</b>
<b>Table of Contents</b>	<b>iv</b>
<b>List of Tables</b>	<b>vi</b>
<b>List of Figures</b>	<b>vii</b>
<b>Acknowledgments</b>	<b>xi</b>
<b>1. INTRODUCTION</b> .....	<b>1</b>
1.1 The need for numerical methods in electromagnetic analysis .....	1
1.2 Review of the transmission line matrix method.....	6
1.3 Organization of the thesis .....	8
<b>2. THE SYMMETRICAL CONDENSED NODE</b> .....	<b>10</b>
2.1 The SCN for time domain TLM simulations .....	10
2.2 On the construction of the frequency domain SCN through the time domain scattering procedure .....	17
2.3 A class of SCNs derived directly in the frequency domain .....	18
2.3.1 Introduction .....	18
2.3.2 Generation of the symbolic scattering matrix .....	19
2.3.3 Determination of node line parameters and s-matrix .....	23
2.4 Accuracy assessment and comparison of various SCNs.....	29
<b>3. THE FREQUENCY-DOMAIN TLM ALGORITHM</b> .....	<b>35</b>

	v
3.1 The concept of intrinsic scattering matrix.....	35
3.2 The FDTLM algorithm for 2D eigenvalue problems.....	39
3.3 The FDTLM algorithm for 3D discontinuity problems .....	41
3.4 Algorithm development — Decoupled frequency domain SCN and solution algorithm .....	44
<b>4. APPLICATIONS OF THE FDTLM METHOD .....</b>	<b>53</b>
4.1 Analysis of propagation characteristics of arbitrary waveguide structures .....	53
4.2 The FDTLM simulation of periodic structures in microwave and integrated optical circuits .....	58
4.3 The s-parameter calculation of arbitrary waveguide structures .....	66
4.4 The FDTLM analysis of the transition from rectangular to circular waveguides .....	74
<b>5. FDTLM METHOD IN 3D CYLINDRICAL COORDINATES .....</b>	<b>82</b>
5.1 Introduction .....	82
5.2 Cylindrical SCN and FDTLM algorithm .....	83
5.3 Applications .....	88
5.3.1 Microstrip discontinuities on cylindrical dielectric substrates.....	88
5.3.2 Field-theory-based analysis of circular waveguide bandpass filters .....	92
<b>6. CONCLUSIONS .....</b>	<b>100</b>
6.1 Discussion .....	100
6.2 Future research .....	102
<b>BIBLIOGRAPHY .....</b>	<b>103</b>
<b>APPENDIX .....</b>	<b>107</b>

## List of Tables

2.1 The dispersion characteristics $\lambda_0 / \lambda_g$ of a suspended stripline obtained with different symmetrical condensed nodes .....	33
4.1 Dispersion and loss characteristics of a microstrip with finite metallization thickness.....	57
4.3 The dimensions of transformers from rectangular to circular waveguides .....	79

## List of Figures

1.1	Yee's grid cell.....	4
2.1	Symmetrical condensed TLM node .....	10
2.2	Scattering matrix of the stub-loaded symmetrical condensed node.....	15
2.3	Scattering matrix of the hybrid symmetrical condensed node.....	16
2.4	Symmetrical condensed FDTLM node .....	22
2.5	Symbolic s-matrix for 3D condensed FDTLM node .....	23
2.6	(a) Cross-section of a suspended stripline; (b) Layout of the TLM graded mesh .....	32
3.1	(a) Space discretized by the TLM network with N exterior branches connecting the discontinuity space to the surrounding space .....	36
	(b) Space discretized by the TLM network with two exterior branches connecting the discontinuity space to the surrounding space .....	37
3.2	A slice of waveguide structure.....	40
3.3	Two-port waveguide discontinuity and equivalent network.....	41
3.4	The frequency domain symmetrical condensed node .....	50
3.5	Pair of 6-port condensed FDTLM nodes .....	50
3.6	The equivalent FDTLM networks of ridged waveguide.....	51
3.7	(a) Cross section and dimensions of a rectangular waveguide partially filled with a dielectric slab. (b) Layout of the TLM graded mesh, .....	52
4.1	Propagation constant versus frequency for a rectangular waveguide filled with a lossy dielectric .....	55
4.2	(a) Dispersion diagram for even and odd fundamental modes of coupled microstrip line.....	56

	(b) Microstrip with finite metallization thickness .....	57
4.3	(a) A vane-type periodic structure. (b) Dispersion diagram ( $a=90.0$ , $h=24.6$ , $b=20.0$ , $d=14.175$ , $t=3.175$ , $a=90.0$ mm).....	62
4.4	(a) Rectangular corrugated waveguide ( $a=b=25.0$ , $h_1=h_2=8.2$ , $d_1=3.0$ , $d_2=1.0$ [mm]); (b) Dispersion diagram (— this method; ----- mode matching method; .... measured data); (c) Isometric configurations of normalised transverse electrical fields of both the first slow mode and the second fast mode. ....	63
4.5	a) Schematic diagram of coplanar slow-wave structure. (b) Effect of slots on phase velocity ( Slotted line has dimensions: $b=9 \mu\text{m}$ , $d=50 \mu\text{m}$ , $g=200 \mu\text{m}$ , $h=80 \mu\text{m}$ , and $w=28 \mu\text{m}$ ; the smooth line has no slots with gap $b=h=9 \mu\text{m}$ ). ....	65
4.6	(a) Dielectric slab loaded waveguide of finite length; (b) S-parameters of the transition from rectangular waveguide to dielectric slab loaded waveguide. ....	68
4.7	Calculated and measured insertion-loss as a function of frequency of a Ka-band 3 resonator E-plane filter. ....	69
4.8	Frequency-dependent S-parameters of the microstrip step-in-width .....	70
4.9	A multichip module structure and simulation model of the chip interconnection using tape automated bonding technique .....	71
4.10	Frequency-dependent S-parameters of the interconnect shown in Fig.4.9 with different distance between pads ( $h_1=0.2\text{mm}$ , $h_2=0.4\text{mm}$ , $w=0.1\text{mm}$ , $w_1=0.2\text{mm}$ , $w_2=0.5\text{mm}$ , $w_3=1.0\text{mm}$ , $l_1=1.6\text{mm}$ , $l_2=0.2\text{mm}$ , $t_1=t_2=t=0$ , $\epsilon_{r,1}=9.8$ , $\epsilon_{r,2}=12.9$ ).....	72
4.11	Frequency-dependent S-parameters of the interconnect shown in Fig.4.9 with different rib widths. ( $h_1=0.2\text{mm}$ , $h_2=0.4\text{mm}$ , $w=0.1\text{mm}$ , $w_1=0.2\text{mm}$ , $w_2=0.5\text{mm}$ , $l=0.2\text{mm}$ , $l_1=1.6\text{mm}$ , $l_2=0.2\text{mm}$ , $t_1=t_2=t=0$ , $\epsilon_{r,1}=9.8$ , $\epsilon_{r,2}=12.9$ ) .....	73

4.12	Three types of transitions from rectangular to circular waveguides. (a) Slot coupled transition. (b) Ridged waveguide step transformer structure. (c) Direct stepped transformer structure. ....	76
4.13	Geometry and the effective dielectric constant of an empty C330 circular waveguide using a stepped approximation. ....	77
4.14	Variation of VSWR with frequency for the structure in Fig.4.12(a). Dimensions: $L=17.00$ mm, $W=1.07$ mm, $a=22.86$ mm, $b=10.16$ mm, and $r=11.85$ mm . ....	78
4.15	Input return loss of the transition shown in Fig.4.12(b). ( WR-28 and C330 standard waveguides; Ridge thickness $t = 0.2$ mm; for transformer dimensions, see Table 4.1.) ....	80
4.16	Input return loss of the transition shown in Fig.4.12(c). ( WR-28 and C330 standard waveguides; for transformer dimensions, see Table 4.1.) ....	81
5.1	(a) The cylindrical coordinate system and location of a node; (b) Symmetrical condensed FDTLM node for cylindrical geometry; (c) $r\theta$ - plane mesh of the symmetrical condensed FDTLM node ....	86
5.2	Frequency-dependent s-parameters of microstrip step-in-width on a half-circular rod substrate ( $r=2.0$ mm, $\epsilon_r=12.9$ ).....	89
5.3	Frequency-dependent s-parameters of microstrip step-in-width on a circular rod substrate embedded in a conducting ground plane ( $r=2.0$ mm, $\epsilon_r=12.9$ ).....	89
5.4	Frequency-dependent S-parameters of microstrip gap discontinuity ( $r_1=10$ mm, $r_2=10.625$ mm, $w=0.635$ mm, $g=0.2$ mm, $\epsilon_r=10$ ).....	90
5.5	Frequency-dependent S-parameters of microstrip transition on two sides of the substrate ( $r_1=4$ mm, $r_2=4.25$ mm, $\epsilon_r=2.2$ , $w_2/w_1=4.1$ , $w_1/(r_2-r_1)=1.0$ ) . ....	91
5.6	Performance versus frequency of a 3-resonator circular waveguide filter .....	94

- 5.7 **Evanescent-mode double-ridged circular waveguide bandpass filter.**  
 (a) Cross sectional view; (b) Longitudinal section dimensions. .... 95
- 5.8 **Insertion loss of the filter versus frequency for different diameters  $D$  of the ridge  $D_1=8.0$  mm,  $D_2=4.0$  mm,  $T=2.0$  mm,  $W_1=0.3$  mm,  $\theta=2.0$  deg.;** (a):  $D=1.0$  mm, (b):  $D=0.8$  mm, (c):  $D=0.6$  mm, (d):  $D=0.4$  mm. .... 96
- 5.9 **Insertion loss of the filter versus frequency for different widths  $W$  of the ridge.  $D_1=8.0$  mm,  $D_2=4.0$  mm,  $T=2.0$  mm,  $D=0.7$  mm,  $\theta=2.0$  deg.;** (a):  $w=0.4$  mm, (b):  $w=0.3$  mm, (c):  $w=0.2$  mm, (d):  $w=0.1$  mm. .... 97
- 5.10 **Insertion loss of the filter versus frequency for different distances  $T$ .  $D_1=8.0$  mm,  $D_2=4.0$  mm,  $W=0.3$  mm,  $D=0.7$  mm,  $\theta=2.0$  deg.;** (a):  $T=4.0$  mm, (b):  $T=3.0$  mm, (c):  $T=2.0$  mm, (d):  $T=1.5$  mm, (e):  $T=1.0$  mm. .... 98
- 5.11 **Insertion loss for the evanescent-mode circular waveguide filter loaded with two or three double-ridges ( $D_1=8.0$  mm,  $D_2=4.0$  mm,  $D=0.7$  mm,  $\theta=2.0$  deg.).** (a) Three double-ridges:  $T=1.55$  mm,  $T_1=T_2=4.6$  mm,  $W_1=W_2=W_3=0.41$  mm; (b) Two double-ridges:  $T=2.0$  mm,  $T_1=4.5$  mm,  $W_1=W_2=0.3$  mm. .... 99

## **Acknowledgments**

I would like to thank my supervisor, Dr. R. Vahldieck of the Department of Electrical and Computer Engineering, for his perpetual encouragement, guidance and advice. His undivided motivation, endeavor, and ability to create a congenial and informal atmosphere for discussion have been the major driving factors in the success of this research.

I thank the members of the LLiMic group, in particular Dr. H. Jin, who first introduced me to the frequency domain transmission line matrix method, for the many discussions that made this thesis better.

I thank Dr. J. Bornemann for aiding me with technical papers during the progress of this research. I would like to thank Dr. S. Stuchly for his kind assistance and enthusiasm.

Financial assistance received from Dr. R. Vahldieck (through NSERC) is gratefully acknowledged.

A word of gratitude to all my friends, in particular Dr. K. Wu, for their moral support, motivation, and encouragement.

And finally, a special thank to my wife, Jun Gao, and son, Chao Huang, for their support and encouragement.

# **Chapter 1**

## **INTRODUCTION**

### **1.1 The Need for Numerical Methods in 3D Electromagnetic Analysis**

With the rapid growth of the telecommunication market, the applications for microwave and high-speed devices are increasingly diversified. Responding to this trend, microwave circuit designs have taken on more importance. However, microwave and high-speed circuit packages usually have complicated three-dimensional structures. The complexity of the package structures makes it difficult to provide appropriate equivalent circuits, and the great variety of package structures requires case-to-case treatment. Therefore, the problem of microwave and high-speed circuit analysis may be summarized by two questions. Firstly, which analysis technique enables the design engineer to analyze such complex package structures? Secondly, how universal is the application of this analysis technique?

Electromagnetic numerical analysis is an attractive solution to these problems. Recently, remarkable progress has been made in computer technology which makes it possible to carry out large-scale computation for various microwave circuit designs. In fact, several numerical analysis software packages are already available on the market. Meanwhile, keeping pace with computer innovation, a number of full-wave numerical analysis methods of electromagnetic fields have been intensively pursued for years. Most readily available are software packages based on the finite element method (FEM), finite difference (FD) method, and transmission line matrix (TLM) method. This section is a brief description of these numerical methods.

**Finite element method** The basic principle of the finite element technique [1,2] is that a field region of interest can be divided into a number of discrete elements. The unknown electromagnetic field is then approximated by a linear combination of a complete set of interpolation functions to represent the variation of the field over the elements. Polynomials are often used as they are easy to integrate and differentiate, also greater accuracy is possible if higher order functions are used. Then, to determine the properties of each element, a variational, or energy-based functional is minimized, leading to a system of equations. Upon solving this system, the unknown nodal values of the field variables are obtained. Knowing these nodal values and geometry of the elements, the field values at any other point can be calculated easily. This means that the field or potential is defined explicitly everywhere, which leads to easy manipulation mathematically. For example, when evaluating spatial derivatives to give the field or impedance, often closed form expressions can be obtained, thus avoiding troublesome numerical integration and differentiation. Furthermore, when triangular elements are being used, a wide variety of odd-shaped geometries can be approximated. This is the main advantage of the FEM.

A disadvantage of the FEM is the potential for spurious modes (non-physical solutions). This problem and the fact that the formulation leads to large matrix equations make this method inconvenient for extraction of scattering parameters of microwave circuits. Furthermore, for scattering parameter calculation of a general two port circuit, the spatial discretization must not only resolve the two port itself but also the space sufficiently far away from the two port so that only one propagating mode can exist at the reference planes.

**Finite difference method** The finite difference technique [3] is based on numerical differences to approximate differentials. This method can be divided into three parts. Firstly, the solution domain is divided into a grid of node points. This grid is uniformly spaced with a shape that reflects the type of problem and its boundary conditions. Secondly, a partial differential equation must be transformed into the most convenient co-ordinate system and then be written as a partial difference equation. The difference formula is used to describe the

functional relationship between nearby nodes in the grid. Finally, the system of equations is solved using matrix algebra.

Discretizing the differential Maxwell equations in space and time is called the finite difference time-domain(FDTD) method [4,5], which has been used to perform time-domain simulation of pulse propagation in arbitrary three-dimensional structures. In the transient analysis of microwave circuits, a short Gaussian pulse is used to excite the circuit. The pulse propagating through the component or circuit is observed in a time iterative process. The frequency dependent data can be calculated by a Fourier transform of the time-domain response.

However, the use of time-domain methods in the analysis of sharp discontinuities requires a very small mesh size, which in turn leads to small time steps to satisfy the stability condition. As a result, the computational effort is significant to reach steady-state conditions.

The finite difference frequency-domain(FDFD) method [6] has been developed to overcome the Fourier transform necessary to give the frequency response of a circuit. It is used to discretize the time-harmonic Maxwell's equations. The space components of the electric and magnetic fields are defined in each elementary cell ( a "Yee"-grid [4]) shown in Fig.1.1. This kind of field allocation has the advantage of implicitly fulfilling the continuity conditions between two neighboring cells of different material. However, the spatial discretization of the complex 3D structure using the FDFD algorithm also leads to a large matrix equation, which has to be solved by using iterative matrix algorithm such as the Jacobi or biconjugate gradient method.

The FD method has been successfully applied to eigenvalue problems for calculating the propagation characteristics of arbitrarily filled guides as well as scattering parameters of arbitrary three-dimensional structures such as MMIC chip interconnections [6]. Comparing the time-domain FD method and the frequency-domain FD method, both approaches are complementary and, in the context of a single method, provide a tool to analyze time-domain as well as frequency-domain problems.

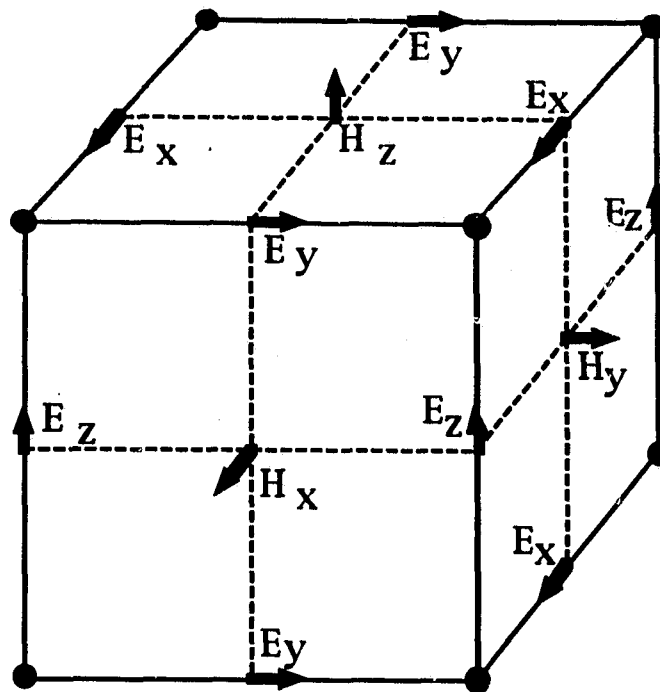


Fig. 1.1 Yee's grid cell

**Transmission line matrix method** The TLM method [7,8] is a numerical technique for solving field problems using equivalent circuits. The TLM method models Maxwell's equations by discretizing the space of interest with a three-dimensional mesh of intersecting transmission lines. The number of transmission line nodes necessary to accurately model a given problem is dependent on the particular geometry being examined and the desired accuracy of the solution. Direct analogies can be drawn between the voltages and currents at the nodes of the mesh and the electric and magnetic fields at these points in space. Similarly, the inductive, capacitive, and resistive properties of the transmission lines correspond to the permeability, permittivity, and conductivity of the space being modeled. By properly terminating the transmission lines, boundaries can be modeled. Thus, the solution of Maxwell's equations is reduced to solving for the currents and voltages at each node in the mesh and this is accomplished via a time-domain iterative process or advanced frequency-domain matrix algorithm.

While the origins of the FEM, FD and TLM methods are different, they are related methods[9,14,18]. These methods are extremely general and flexible. They model the intrinsic behavior of electromagnetic fields without reference to specific boundary and material configuration. They can be formulated either for time-harmonic or time-varying fields in two- or three-dimensional space, thus forming the basis for either frequency-domain steady state or time-domain transient analysis of electromagnetic problems.

In developing a numerical method one should always consider efficiency (i.e. CPU time and memory space), accuracy and flexibility (i.e. capability to model a large variety of structures). On the other hand, the choice of a numerical method is also strictly dependent on the problem at hand. No method can be thought of as the best one. Each can have advantages over the others. The contribution of the TLM method is that the TLM node can be represented as a passive transmission line network for which the scattering matrix is known. Since the node scattering matrix only relates the reflected and incident wave voltages at the surface (boundary) of each node, the reflected and incident wave voltages at different nodes are then interconnected by imposing the boundary conditions at the interfaces of nodes. Therefore, in the frequency-domain TLM node, the voltage variables at the interface between nodes can be easily eliminated when nodes are interconnected. The resulting scattering matrix only relates the variables at the exterior branches of the guided structure, i.e. the size of the final general scattering matrix is only dependent on the area of the boundary surface of the structure regardless of the complexity and the volume of the structure within the boundary surface. This feature is particularly useful in the analysis of microwave circuits where the boundary surface (usually the reference plane in the circuit analysis) consists of the cross sections of the uniform guided structure which are usually much smaller in comparison with the total volume of the circuit. This makes it possible for the TLM method to handle complicated and large structures through matrix algebra. In fact, eliminating the voltage (field) variables at the interior node branches will reduce the size of the operating matrix and hence reduce the CPU time significantly.

Considering the above attractive feature of the frequency domain TLM node and algorithm, the motivation of this thesis is to develop method further and to

apply it to practical microwave circuit problems. We first begin with a detailed review of the TLM method.

## 1.2 Review of the Transmission Line Matrix Method

Back in 1944, an equivalent electrical network had been developed by Kron [10] representing the field equations of Maxwell. In the same year, Whinnery and Ramo [11] successfully applied this equivalent network to the solution of high frequency field problems using a two-dimensional Cartesian mesh. Inspired by the above ideas, Johns and Beurle first developed the transmission line matrix method, by which very good results were obtained for the solution of two-dimensional waveguide problems in 1971 [7]. Subsequent papers [2,8] applied this method to inhomogeneous and lossy problems and also extended this method to three-dimensional cases. Various features and improvements were also added by other researchers in a short period of time. The theory and application of the TLM method for time-domain electromagnetic simulation are described in a review paper[2] and a chapter on TLM by Hoefler[8].

It should be mentioned that the symmetrical condensed node, as first proposed by Johns in 1986 [12], has contributed to the method to make it a more accurate and computationally more efficient technique for three-dimensional electromagnetic field analysis in the time domain. Since then some new concepts like the time-domain diakoptics [13], the time-domain Green's function [15] have further improved the method.

While the time-domain TLM(TDTLM) algorithm provides direct solutions for transient analysis and visualization of electromagnetic wave phenomena, frequency-domain data can only be obtained from a Fourier transform of the impulse response of the network. For many applications, however, only a steady-state circuit analysis and design is required and only a small frequency range is of interest. Hence, in computational comparison to some methods which work entirely in the frequency-domain, time-domain methods are at a disadvantage. There are several reasons for this. The most prominent among all is that the TDTLM algorithm is a simple time iterative process for solving a system of linear equations with scattering and connection matrices as well as initial values. This

procedure is naturally slow since many advanced matrix algebra techniques cannot be applied. Furthermore, the transformation from the time-domain into the frequency-domain introduces errors which are not always negligible. For example, to extract the microwave scattering parameters over a wide range of frequencies from a single TLM simulation, wideband absorbing boundaries must be modeled in the time-domain. Unfortunately, there are no perfect and wideband absorbing boundaries. Practically every absorbing boundary will produce a few percent of reflection, particularly in structures supporting non-TEM modes of propagation. Thus, even though the time-domain results may be reasonably accurate, the frequency-domain results obtained from their Fourier transform may not be acceptable, since the Fourier transform of the time-domain response is very sensitive to imperfect boundary treatment. Thus, the time-domain simulation of absorbing boundary conditions is crucial for accurate computation of scattering parameters.

In order to retain the flexibility of the TLM method and, at the same time, avoid the problems that occur when transforming from one domain into another, the FDTLM method has been developed by Jin and Vahldieck [16]. In this method, the space is discretized by the same transmission line network as in the conventional TDTLM method. However, instead of exciting the network with a single impulse, an impulse train of sinusoidally modulated magnitude is assumed. At any time step, this new excitation retains the form of an impulse but its modulated envelope contains the information of the structure at a particular modulation frequency. Hence, the frequency-domain information of the system is directly obtained from the impulse response amplitude rather than through the Fourier transform. Since the entire solution procedure is carried out in the frequency-domain, this method takes advantage of the numerous advanced frequency-domain techniques, such as the diakoptics and matrix algebra techniques, to greatly enhance its computational efficiency.

Historically, the TLM method was developed from lumped electrical network theory, which has been used to represent electromagnetic fields for many years as a standard frequency-domain analogue technique. For a given structure, the FDTLM method starts with discretizing the space with a transmission line matrix or periodic arrays of nodes similar to the TDTLM method. Thus, the FDTLM algorithm does not leave the framework of the TLM method. However, since the

FDTLM method operates entirely in the frequency-domain, the less restrictive requirements in constructing the FDTLM nodes allow a wider range of transmission line networks to be used. In conjunction with a novel scattering parameter extraction technique [16], a very powerful and flexible numerical modeling tool can be developed for frequency domain design problems. As such, the FDTLM method represents a true frequency domain counterpart to the time domain TLM method.

Based on the current state and original contributions of the TLM method, the purpose of this thesis work is to describe and develop systematically the physical modeling process, the formulation, and the implementation of the FDTLM method. This new numerical technique combines the flexibility and versatility of the time-domain TLM method with the computational efficiency of conventional frequency-domain methods. A general-purpose computer program for the full-wave electromagnetic analysis is applied to calculate a variety of 2D and 3D electromagnetic problems.

### **1.3 Organization of this Thesis**

This thesis is divided into six chapters which are outlined below:

Chapter 2 describes the origin of the symmetrical condensed TLM node for the time-domain simulation. Then, it is illustrated that the nodes used in the FDTLM method can be constructed through either the time-domain scattering procedure or derived directly in the frequency domain. The corresponding scattering matrices are given. Finally, a comparison of the different available nodes is made. The best use of the various nodes is discussed.

Chapter 3 first introduces the concept of the intrinsic scattering matrix. Then, the FDTLM algorithm is established for solving waveguide eigenvalue problems and spatial three-dimensional discontinuity problems. An efficient method to develop the algorithm is also introduced for reducing the computer storage and run-time.

Chapter 4 deals with the applications of the FDTLM method for the calculation of propagating characteristics of arbitrary waveguide structures as

well as scattering parameters of arbitrary spatial discontinuities. As a special case, the FDTLM algorithm is implemented to analyze the characterization of periodic structures in microwave and integrated optical circuits.

Chapter 5 develops a generalized treatment of the FDTLM method in a cylindrical coordinate system in order to facilitate modeling of cylindrical guided structures. Furthermore, microstrip discontinuities on cylindrical dielectric substrates as well as circular waveguide bandpass filters are calculated using the cylindrical FDTLM algorithm.

Chapter 6 concludes this thesis and discusses possible future research .

## Chapter 2

# THE SYMMETRICAL CONDENSED NODE

### 2.1 The SCN for Time Domain TLM Simulation

The symmetrical condensed node (SCN) has been developed by Johns in 1986[12,17]. He develops first the SCN without stubs (Fig. 2.1) for modeling a homogeneous space with identical cubic space nodes. This approach has obviously limited application. After presenting the concept, he extends the analysis to generate a node with inductive and capacitive stubs to model inhomogeneous space and graded mesh.

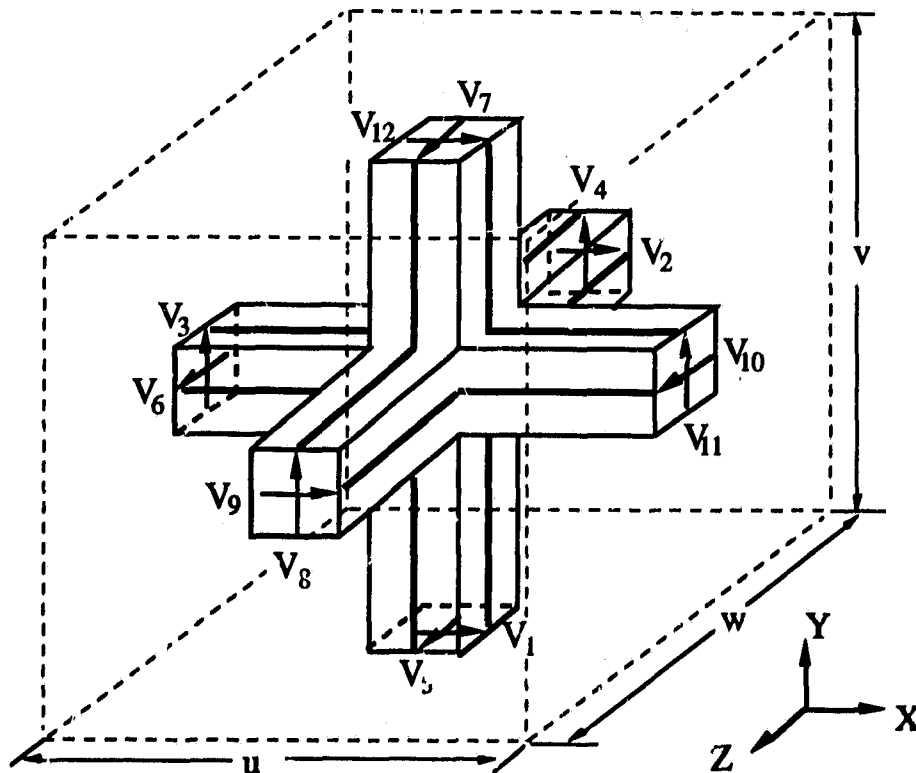


Fig. 2.1 Symmetrical condensed TLM node

The SCN has significantly advanced the TLM method. Unlike former nodes, which are traditionally represented as a passive transmission line network, the SCN is essentially an algebraic object: a novel physical picture of the discretized Maxwell equations. Over the years, significant improvements of this node have been published [19-22]. Moreover, reference [18] demonstrates that the SCN can be formulated directly from Maxwell's equations using centered differencing and averaging. Based on the derivation presented, one finds that the SCN always preserves a second-order accuracy regardless of a uniform or graded mesh. Reference [37] also gives the field theoretical derivation of TLM using the Method of Moments. In fact, the SCN is a unique finite difference scheme. Therefore, it can be considered as either a physical model of the FD method or a mathematical model of the TLM method.

Usually, it is convenient to express a numerical algorithm in terms of a network model. The physical picture given can often help us to visualize the properties of the method. Hence, in this section, the emphasis will be on the network modeling approach of the SCN for the TDTLM algorithm. As shown in Fig. 2.1, each of the six branches represents two transmission lines carrying the two possible polarizations of the wave traveling in a given direction. The characteristic impedance of these lines is that of free space. The voltages indicated in the figure are the voltages across the transmission lines at each of the twelve ports. The dimensions of the node are  $u, v$  and  $w$  in the  $x, y$  and  $z$  directions, respectively. The approximate differential equations that govern the behavior of voltages and currents at each node are given in time-varying form:

$$\begin{aligned}
 v \frac{\partial I_x}{\partial y} - w \frac{\partial I_y}{\partial z} &= C_x \frac{\partial V_x}{\partial t} & v \frac{\partial V_x}{\partial y} - w \frac{\partial V_y}{\partial z} &= -L_x \frac{\partial I_x}{\partial t} \\
 w \frac{\partial I_x}{\partial z} - u \frac{\partial I_z}{\partial x} &= C_y \frac{\partial V_y}{\partial t} & w \frac{\partial V_x}{\partial z} - u \frac{\partial V_z}{\partial x} &= -L_y \frac{\partial I_y}{\partial t} \\
 u \frac{\partial I_y}{\partial x} - v \frac{\partial I_z}{\partial y} &= C_z \frac{\partial V_z}{\partial t} & u \frac{\partial V_y}{\partial x} - v \frac{\partial V_z}{\partial y} &= -L_z \frac{\partial I_z}{\partial t}
 \end{aligned} \tag{2.1}$$

where  $L_x, L_y$ , and  $L_z$  are the total inductances associated with the  $x, y$ , and  $z$  directed transmission lines and  $C_x, C_y$ , and  $C_z$  are the total capacitances.  $I_x, I_y$ , and  $I_z$  are the net currents flowing in the  $x, y$ , and  $z$  directions. The voltages  $V_x, V_y$ , and  $V_z$  are defined to be the total  $x, y$ , and  $z$  directed voltages at the node.

Now the following equivalences are established relating voltages and currents to the electric and magnetic fields:

$$\begin{aligned}
 E_x &\equiv V_x / u & H_x &\equiv I_x / u \\
 E_y &\equiv V_y / v & H_y &\equiv I_y / v \\
 E_z &\equiv V_z / w & H_z &\equiv I_z / w
 \end{aligned} \tag{2.2}$$

Substituting these into (2.1), the following set of differential equations is obtained:

$$\begin{aligned}
 \frac{\partial H_x}{\partial y} - \frac{\partial H_y}{\partial z} &= C_x \frac{u}{wv} \frac{\partial E_x}{\partial t} & \frac{\partial E_z}{\partial y} - \frac{\partial E_y}{\partial z} &= -L_x \frac{u}{wv} \frac{\partial H_x}{\partial t} \\
 \frac{\partial H_x}{\partial z} - \frac{\partial H_z}{\partial x} &= C_y \frac{v}{uw} \frac{\partial E_y}{\partial t} & \frac{\partial E_x}{\partial z} - \frac{\partial E_z}{\partial x} &= -L_y \frac{v}{uw} \frac{\partial H_y}{\partial t} \\
 \frac{\partial H_y}{\partial x} - \frac{\partial H_x}{\partial y} &= C_z \frac{w}{uv} \frac{\partial E_z}{\partial t} & \frac{\partial E_y}{\partial x} - \frac{\partial E_x}{\partial y} &= -L_z \frac{w}{uv} \frac{\partial H_z}{\partial t}
 \end{aligned} \tag{2.3}$$

Comparing equation (2.1) with (2.3) yields the following equivalence between the parameters:

$$\begin{aligned}
 C_x &\equiv \epsilon \frac{wv}{u} & L_x &\equiv \mu \frac{wv}{u} \\
 C_y &\equiv \epsilon \frac{uw}{v} & L_y &\equiv \mu \frac{uw}{v} \\
 C_z &\equiv \epsilon \frac{uv}{w} & L_z &\equiv \mu \frac{uv}{w}
 \end{aligned} \tag{2.4}$$

Then equation (2.3) exactly corresponds to the time-varying Maxwell's curl equations, *i.e.*,

$$\begin{aligned}
 \nabla \times \vec{E} &= -\mu \frac{\partial \vec{H}}{\partial t} \\
 \nabla \times \vec{H} &= \epsilon \frac{\partial \vec{E}}{\partial t}
 \end{aligned} \tag{2.5}$$

In order to solve the transmission line mesh with impulses and obtain the scattering procedure for the time-domain node, the most important condition is the space-time synchronism, which means that the wave impulses must reach the

nodes or boundaries at the same phase delay, regardless of the distance they cover between any two consecutive nodes in any direction. Therefore, any solution must assume that the propagation velocity of the voltage waves is proportional to the line length. This requires that the distributed inductance,  $L_d$ , and capacitance,  $C_d$ , be the same on all of the transmission lines in the network. Therefore, in order for (2.4) to be satisfied, it is necessary to add inductances and/or capacitances to certain nodes in the mesh in order to model the material properties and shape of a given node. The required additional inductances and capacitances are usually added to the nodes using short and open circuited transmission line stubs attached to the center of each node. The other alternative is that the branch lines are allowed to assume different characteristic impedances such that they incorporate all of the required inductances or capacitances. Stubs are still needed but fewer than in the first case. The first option results in a node loaded with two kinds of stubs (stub-loaded node) developed by Johns in 1987 [17], which leads to a  $(18 \times 18)$  node scattering matrix with 12 main branches and 6 stubs. The second gives a node with lines of different characteristic impedances and at least one kind of stub (hybrid node) described by Scaramuzza and Lowery 1990 [19], which leads to a  $(15 \times 15)$  node scattering matrix also with 12 main branches but only 3 stubs. The complete scattering matrices for both stub-loaded and hybrid nodes are given in Fig. 2.2 and Fig. 2.3.

Now the problem of solving for the vector electric and magnetic field quantities has been simplified to that of solving for the voltages and currents on a 3D transmission line mesh. This is accomplished most conveniently by performing an impulse analysis of the mesh. The mesh is initially excited with ideal voltage and/or current impulses corresponding to the desired excitation field values. These initial impulses are then tracked in time as they travel between and scatter at the nodes in the mesh. The pulses reflected from a node at time step  $k$  are given by

$${}_k V^r = S \cdot {}_k V^i \quad (2.6)$$

where  ${}_k V^r$  is the vector of reflected voltages at time  $k$ ,  ${}_k V^i$  is the vector of voltages incident on the node at time step  $k$ , and  $S$  is the scattering matrix for a TLM node. The pulses reflected from a particular node in the mesh become incident on

neighboring nodes at the next time step. This transfer is represented by a connection matrix  $C$ ,

$${}_{k+1}V^i = C \cdot {}_kV^r \quad (2.7)$$

This scatter and connect time-stepping procedure is continued until the desired steady state is reached. Obviously, by combining (2.6) and (2.7), the TDTLM algorithm is essentially a simple time iteration procedure.

Again, since the excitation is by ideal impulses, the output consists of a stream of impulses in time for a given field component which corresponds to the impulse response of the mesh for a particular excitation. This output impulse response can be Fourier transformed to yield frequency domain information, or it may be convolved, in the time domain, with any arbitrary excitation function.

However, it should be recognized that accurate frequency-domain data obtained from a Fourier transform of the TLM impulse response requires long iteration times. Sometimes this can result in excessive computation time which renders the TDTLM inconvenient for frequency-domain design and optimization problems. In order to avoid the shortcomings of the TDTLM algorithm while retaining its great flexibility and versatility, the FDTLM algorithm has been developed to represent a true frequency-domain counterpart to the time-domain TLM method. This new FDTLM algorithm is based on either the time-domain TLM node or, for more efficient computation, on a new class of FDTLM nodes.

	1	2	3	4	5	6	7	8	9	10	11	12	13	14	15	16	17	18
(Y)	x	x	y	y	z	z	z	y	x	z	y	x	x	y	z			
(Z)	z	y	z	x	x	y	x	x	y	y	z	z				x	y	z
1	x	z	a	b	d				b	-d	c	e						f
2	x	y	b	a		d			c	-d	b	e					-f	
3	y	z	d		a	b		b			c	-d	e					-f
4	y	x		b	a	d		-d	c		b		e			f		
5	z	x			d	a	b	c	-d		b			e	-f			
6	z	y		d		b	a	b		-d	c			e		f		
7	z	x			-d	c	b	a	d		b			e	f			
8	y	x		b	c	-d		d	a		b		e		-f			
9	x	y	b	c			-d		a	d		b	e			f		
10	z	y	-d			b	c	b		d	a			e		-f		
11	y	z		c	b			b			a	d	e					f
12	x	z	c	b	-d				b		d	a	e					-f
13	x		e	e					e			e	g					
14	y			e	e			e			e			g				
15	z				e	e	e			e					g			
16	x			f	-f		f	-f								h		
17	y	-f				f			f	-f							h	
18	z	f	-f								f	-f						h

(Y) (Z)

The matrix element:

$$a = \frac{-Y}{2(4+Y)} + \frac{Z}{2(4+Z)}, \quad b = \frac{2}{Y+4}$$

$$c = \frac{-Y}{2(4+Y)} - \frac{Z}{2(4+Z)}, \quad d = \frac{2}{Z+4}$$

$$g = \frac{Y-4}{Y+4}, \quad h = \frac{4-Z}{4+Z}, \quad e = \sqrt{Y} \cdot b, \quad f = \sqrt{Z} \cdot d$$

The values of the inductive (Z) and capacitive (Y) Stubs:

$$Y_x = 4\left(\epsilon_x \frac{vw}{u\Delta l} - 1\right), \quad Y_y = 4\left(\epsilon_y \frac{uw}{v\Delta l} - 1\right), \quad Y_z = 4\left(\epsilon_z \frac{uv}{w\Delta l} - 1\right)$$

$$Z_x = 4\left(\mu_x \frac{vw}{u\Delta l} - 1\right), \quad Z_y = 4\left(\mu_y \frac{uw}{v\Delta l} - 1\right), \quad Z_z = 4\left(\mu_z \frac{uv}{w\Delta l} - 1\right)$$

Fig. 2.2 Scattering matrix of the stub-loaded symmetrical condensed node

$Y_1$	y	z	x	z	y	x	y	z	z	x	x	y								
$Y_1$	z	y	z	x	x	y	x	x	y	y	z	z								
$Y_2$	x	x	y	y	z	z	z	y	x	z	y	x	x	y	z					
$Y_s$	1	2	3	4	5	6	7	8	9	10	11	12	13	14	15					
x	1	a	b	d					b	-d	a	g								
x	2	b	a			d			a	-d	b	g								
y	3	d		a	b			b			a	-d	g							
y	4			b	a	d		-d	a		b		g							
z	5			d	a	b	a	-d		b						g				
z	6		d		b	a	b		-d	a						g				
z	7				-d	a	b	a	d		b					g				
y	8			b	a	-d		d	a		b		g							
x	9	b	a				-d			a	d		b	g						
z	10		-d			b	a	b		d	a					g				
y	11	-d		a	b				b			a	d		g					
x	12	a	b	-d						b		d	a	g						
x	13	b	b							b		b	h							
y	14			b	b				b			b		h						
z	15					b	b	b		b					h					

The matrix elements:

$$a = \frac{-Y_s + 2(Y_1 - Y_2)}{2[Y_s + 2(Y_1 + Y_2)]}, \quad b = \frac{2Y_1}{Y_s + 2(Y_1 + Y_2)}$$

$$d = \frac{1}{2}, \quad g = b \frac{Y_s}{Y_1}, \quad h = \frac{Y_s - 2(Y_1 + Y_2)}{Y_s + 2(Y_1 + Y_2)}$$

The values of the characteristic admittance and capacitive ( $Y_s$ ) Stubs:

$$Y_x = \frac{u\Delta l}{\mu_x v w}, \quad Y_y = \frac{v\Delta l}{\mu_y u w}, \quad Y_z = \frac{w\Delta l}{\mu_z u v}$$

$$Y_{sx} = \frac{4\epsilon_x}{\mu_x Y_x} - 2(Y_y + Y_z), \quad Y_{sy} = \frac{4\epsilon_y}{\mu_y Y_y} - 2(Y_x + Y_z), \quad Y_{sz} = \frac{4\epsilon_z}{\mu_z Y_z} - 2(Y_x + Y_y)$$

Fig. 2.3 Scattering matrix of the hybrid symmetrical condensed node

## 2.2 On the Construction of the Frequency Domain SCN through the Time Domain Scattering Procedure

As in the TDTLM method, the FDTLM algorithm discretizes the space to be analyzed by a transmission line network. The difference to the TDTLM method, however, is that the network excitation is done by a pulse train with time-harmonic (sinusoid) wave amplitude. Therefore, the resulting frequency-domain solution can be regarded as a particular case of the transient solution. Since a time-domain solution can also be considered as a superposition of frequency-domain steady-state solutions with different frequencies, it follows that, in principle, the same space discretization may be used for both time-domain and frequency-domain simulations. The frequency-domain node is not only similar to the time-domain node but also preserves the basic properties of the time-domain node.

Based on this consideration, the FDTLM node can be constructed by modifying the existing TDTLM nodes. Without losing generality, we may write the scattering matrix equation for two kinds of symmetrical condensed nodes (stub-loaded node and hybrid node) as follows:

$$\begin{bmatrix} V_m^r \\ V_s^r \end{bmatrix} = [S] \cdot \begin{bmatrix} V_m^i \\ V_s^i \end{bmatrix} = \begin{bmatrix} S_{mm} & S_{ms} \\ S_{sm} & S_{ss} \end{bmatrix} \cdot \begin{bmatrix} V_m^i \\ V_s^i \end{bmatrix} \quad (2.8)$$

where  $V_m^r, V_s^r$  are the vectors of the reflected voltages at the main branches and stubs, respectively, while  $V_m^i, V_s^i$  denote the vectors of incident voltages.  $S$  is the node scattering matrix. The matrix coefficients are given in Fig.2.2 and Fig.2.3 for the general case with graded mesh and anisotropic materials.

By assuming that  $d$  is the minimum of all the node dimensions throughout the mesh, the propagation factor is defined as  $e^{-jk_0 d}$ , where  $k_0$  is the wave number of free space. Therefore, for the stubs, the reflected voltages are related to the incident voltages at the center of the nodes in the following way:

$$V_s^i = e^{-jk_0 d} \cdot \Gamma_s \cdot V_s^r \quad (2.9)$$

where  $\Gamma_s$  is a diagonal matrix with the  $i^{\text{th}}$  element being either 1 or -1, depending on whether the  $i^{\text{th}}$  stub is open or short circuited. From equations (2.8) and (2.9),

the relationship between the incident and reflected voltages at the main branches can be obtained by

$$V_m^r = [S_{mm} + e^{-jk_0d} \cdot S_{ms} \cdot \Gamma_s \cdot (I - e^{-jk_0d} \cdot S_{ss} \cdot \Gamma_s)^{-1} \cdot S_{sm}] \cdot V_m^i \quad (2.10)$$

equation (2.10) relates the reflected and incident voltages of the main branches at the center of the node. Then moving the reference plane from the center of the node to the boundary of the node, *i.e.* the ports of the main branches, yields

$${}_pV_m^r = e^{-jk_0d} \cdot [S_{mm} + e^{-jk_0d} \cdot S_{ms} \cdot \Gamma_s \cdot (I - e^{-jk_0d} \cdot S_{ss} \cdot \Gamma_s)^{-1} \cdot S_{sm}] {}_pV_m^i \quad (2.11)$$

Equation (2.11) provides a direct expression for the scattering matrix of the symmetrical condensed FDTLM node. The scattering matrix relates the reflected and incident voltages at the ports of the main branches of the node and its property is completely dependent upon both the propagation factor and the node scattering matrix.

It is obvious that any kind of nodes used in the TDTLM algorithm can be readily used for the FDTLM method, with some slight modifications. The main procedure of constructing the frequency-domain node from the existing time-domain node is to eliminate the stubs and then move the reference planes from the center of the node to the boundary of the node. Thus, any full-wave three-dimensional TLM node can be expressed in the frequency-domain by a  $(12 \times 12)$  scattering matrix.

## 2.3 A Class of SCNs Derived Directly in the Frequency Domain

### 2.3.1 Introduction

The concept of the frequency-domain TLM (FDTLM) method was first introduced by Jin and Vahldieck in [16]. The theoretical foundation of the FDTLM algorithm in conjunction with a scattering parameter extraction technique is well established and has been tested for a large variety of microwave

structures. The FDTLM node may be constructed from the existing time-domain TLM node, which is formulated from general time-varying Maxwell's curl equations. To preserve the space-time synchronism or the conservation of charge and magnetic flux in the time-domain node, the choice of values of the electric parameters on the link transmission lines of the node is limited. Therefore, whenever necessary, stubs are added for compensation. In the derivation of the FDTLM algorithm, the stub lines of these nodes are absorbed into the link lines of the node. As a result, the scattering matrix of the FDTLM node becomes an implicit expression. In addition, as shown in section 2.2, the procedure to eliminate the stub lines of the TDTLM node will add computer run-time.

However, if the FDTLM nodes are derived directly in the frequency domain using Maxwell's equations in time-harmonic forms, then the time-domain detour is not necessary. This is indeed possible, because in the frequency domain the space-time synchronism is not required and, therefore, an extra degree of freedom is added which can be used to choose freely the propagation constants and characteristic admittances on the link transmission lines of the node as to represent the properties of the discretized space correctly. Thus stubs are no longer needed in the FDTLM node. Since stubs need not to be considered in the frequency domain node, the determination of scattering coefficients becomes rather simple to handle. This makes the newly developed frequency domain node presented in this section very attractive.

### **2.3.2 Generation of the symbolic scattering matrix**

Starting from the frequency domain symmetrical condensed node shown in Fig.2.4, the corresponding symbolic scattering matrix is shown in Fig.2.5. This node is the intersection of six link transmission lines. Note that these lines have certain propagation constants and characteristic admittances. Without losing generality, we first assume that the characteristic admittances of link lines for 6 polarized directions of the wave are as follows:

Line Polarized Direction	Admittance
+xy , -xy	Y <sub>d1</sub>
+xz , -xz	Y <sub>d2</sub>
+yz , -yz	Y <sub>d3</sub>
+yx , -yx	Y <sub>d4</sub>
+zx , -zx	Y <sub>d5</sub>
+zy , -zy	Y <sub>d6</sub>

Since the SCN is a 12-port lossless junction at the centre of the node, the energy conservation condition leads to

$$[S]^T \cdot [Y_d] \cdot [S]^* = [Y_d] \quad (2.12)$$

where  $[S]$  is the symbolic scattering matrix of the node, and  $[Y_d]$  is the diagonal admittance matrix including 12 link line characteristic admittances. Applying equation (2.12) with current and voltage conservation laws yields the 30 equations in appendix. As there are only 24 variables, this matrix is solveable. Furthermore, it is observed that the variables of each row of the symbolic scattering matrix may be solved independently. Thus the solution procedure becomes rather simple. As an example, a set of nonlinear simultaneous equations are obtained by considering  $\pm xy$  polarized directions, i.e.,

$$\begin{aligned} Y_{d1}(a_1^2 + c_1^2) + 2Y_{d6}b_1^2 + 2Y_{d4}d_1^2 &= Y_{d1} \\ Y_{d1}a_1c_1 + Y_{d6}b_1^2 - Y_{d4}d_1^2 &= 0 \\ Y_{d1}(a_1 + c_1) + 2Y_{d6}b_1 &= Y_{d1} \\ Y_{d1}(a_1 - c_1) + 2Y_{d4}d_1 &= Y_{d1} \end{aligned} \quad (2.13)$$

After some manipulations, one finds three useful solutions which correspond to the shunt node, series node and condensed node, respectively. The solution of the condensed node is

$$\begin{aligned}
a_1 &= \frac{Y_{d1} - Y_{d6}}{2(Y_{d1} + Y_{d6})} + \frac{Y_{d1} - Y_{d4}}{2(Y_{d1} + Y_{d4})} \\
c_1 &= \frac{Y_{d1} - Y_{d6}}{2(Y_{d1} + Y_{d6})} - \frac{Y_{d1} - Y_{d4}}{2(Y_{d1} + Y_{d4})} \\
b_1 &= \frac{Y_{d1}}{Y_{d1} + Y_{d6}} \quad , \quad d_1 = \frac{Y_{d1}}{Y_{d1} + Y_{d4}}
\end{aligned} \tag{2.14a}$$

Similarly, the remaining variables of the symbolic scattering matrix may be found by taking other polarized directions. The complete solutions are given by

$$\begin{aligned}
a_2 &= \frac{Y_{d2} - Y_{d3}}{2(Y_{d2} + Y_{d3})} + \frac{Y_{d2} - Y_{d5}}{2(Y_{d2} + Y_{d5})} \\
c_2 &= \frac{Y_{d2} - Y_{d3}}{2(Y_{d2} + Y_{d3})} - \frac{Y_{d2} - Y_{d5}}{2(Y_{d2} + Y_{d5})} \\
b_2 &= \frac{Y_{d2}}{Y_{d2} + Y_{d3}} \quad , \quad d_2 = \frac{Y_{d2}}{Y_{d2} + Y_{d5}}
\end{aligned} \tag{2.14b}$$

$$\begin{aligned}
a_3 &= \frac{Y_{d3} - Y_{d2}}{2(Y_{d3} + Y_{d2})} + \frac{Y_{d3} - Y_{d6}}{2(Y_{d3} + Y_{d6})} \\
c_3 &= \frac{Y_{d3} - Y_{d2}}{2(Y_{d3} + Y_{d2})} - \frac{Y_{d3} - Y_{d6}}{2(Y_{d3} + Y_{d6})} \\
b_3 &= \frac{Y_{d3}}{Y_{d3} + Y_{d2}} \quad , \quad d_3 = \frac{Y_{d3}}{Y_{d3} + Y_{d6}}
\end{aligned} \tag{2.14c}$$

$$\begin{aligned}
a_4 &= \frac{Y_{d4} - Y_{d5}}{2(Y_{d4} + Y_{d5})} + \frac{Y_{d4} - Y_{d1}}{2(Y_{d4} + Y_{d1})} \\
c_4 &= \frac{Y_{d4} - Y_{d5}}{2(Y_{d4} + Y_{d5})} - \frac{Y_{d4} - Y_{d1}}{2(Y_{d4} + Y_{d1})} \\
b_4 &= \frac{Y_{d4}}{Y_{d4} + Y_{d5}} \quad , \quad d_4 = \frac{Y_{d4}}{Y_{d4} + Y_{d1}}
\end{aligned} \tag{2.14d}$$

$$\begin{aligned}
a_5 &= \frac{Y_{d5} - Y_{d4}}{2(Y_{d5} + Y_{d4})} + \frac{Y_{d5} - Y_{d2}}{2(Y_{d5} + Y_{d2})} \\
c_5 &= \frac{Y_{d5} - Y_{d4}}{2(Y_{d5} + Y_{d4})} - \frac{Y_{d5} - Y_{d2}}{2(Y_{d5} + Y_{d2})} \\
b_5 &= \frac{Y_{d5}}{Y_{d5} + Y_{d4}} \quad , \quad d_5 = \frac{Y_{d5}}{Y_{d5} + Y_{d2}}
\end{aligned} \tag{2.14e}$$

$$\begin{aligned}
 a_6 &= \frac{Y_{d6} - Y_{d1}}{2(Y_{d6} + Y_{d1})} + \frac{Y_{d6} - Y_{d3}}{2(Y_{d6} + Y_{d3})} \\
 c_6 &= \frac{Y_{d6} - Y_{d1}}{2(Y_{d6} + Y_{d1})} - \frac{Y_{d6} - Y_{d3}}{2(Y_{d6} + Y_{d3})} \\
 b_6 &= \frac{Z_{d6}}{Y_{d6} + Y_{d1}}, \quad d_6 = \frac{Y_{d6}}{Y_{d6} + Y_{d3}}
 \end{aligned}
 \tag{2.14f}$$

The FDTLM method is a space discretization technique. The local electromagnetic field is represented at the ports of the FDTLM node. Each node can be constructed independently of its environment and characterized by a scattering matrix. A general scattering matrix at the centre of the node is obtained from the conservation laws. Furthermore, to construct the entire FDTLM algorithm by joining all scattering matrices of the nodes in the discretized space, the reference planes for the scattering matrix must be moved from the centre of the node to the ports of the node. To do so, the node link line parameters must be determined. This procedure follows in the next section.

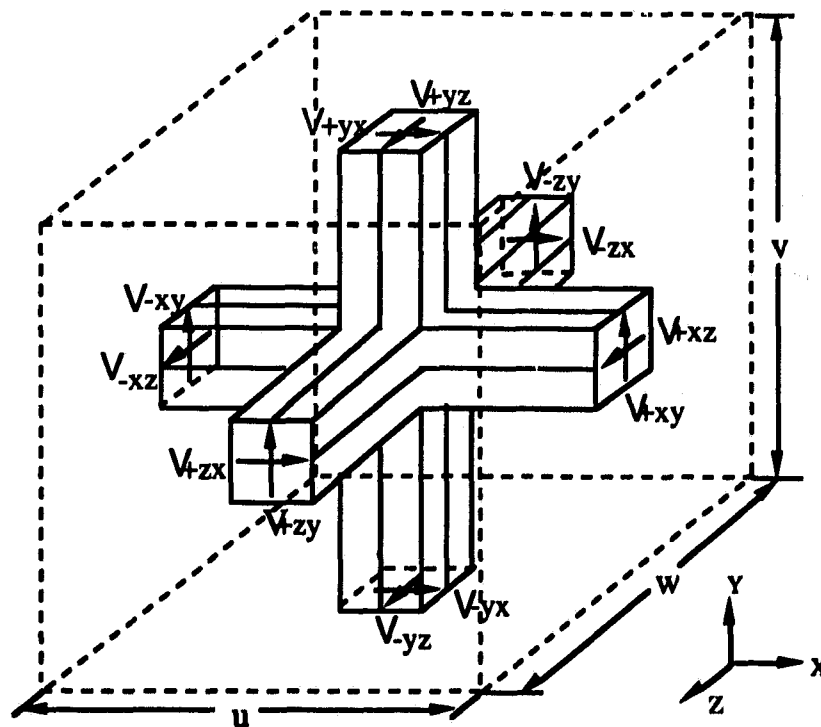


Fig. 2.4 Symmetrical condensed FDTLM node



line network. Again, equation (2.15) corresponds exactly to the time-harmonic Maxwell's curl equations. According to equation (2.4), we can now equate the total inductance and capacitance of the discretized medium to the distributed inductance and capacitance of the link lines. In all six polarized directions, the distributed inductances and capacitances of link lines are denoted as follows:

$$C_{dxy}, C_{dxx}, C_{dyx}, C_{dyz}, C_{dxy}, C_{dxx}$$

$$L_{dxy}, L_{dxx}, L_{dyx}, L_{dyz}, L_{dxy}, L_{dxx}$$

Hence

$$\begin{aligned} \varepsilon \frac{vw}{u} &= C_{dyx}v + C_{dxx}w & \mu \frac{vw}{u} &= L_{dyz}v + L_{dxy}w \\ \varepsilon \frac{uw}{v} &= C_{dxy}u + C_{dxy}w & \mu \frac{uw}{v} &= L_{dxx}u + L_{dxx}w \\ \varepsilon \frac{uv}{w} &= C_{dxx}u + C_{dyz}v & \mu \frac{uv}{w} &= L_{dxy}u + L_{dyx}v \end{aligned} \quad (2.16)$$

where  $\varepsilon$  and  $\mu$  are the permittivity and permeability of the space in which the node is located. The characteristic admittance and propagation constant on the link lines of the node are defined by

$$Y_d = \sqrt{\frac{C_d}{L_d}} \quad (2.17)$$

$$\gamma_d = \omega \sqrt{L_d C_d}$$

and the intrinsic admittance and propagation constant in the discretized medium of the node are

$$Y_0 = \sqrt{\frac{\varepsilon}{\mu}} \quad (2.18)$$

$$k_0 = \omega \sqrt{\varepsilon \mu}$$

Combining equations (2.16) with (2.17) and (2.18), the whole node line parameters and scattering matrix can be solved by choosing the different conditions. In this section, three optional approaches to construct the condensed FDTLM nodes are presented.

**The Characteristic Admittance Node** As the simplest case, we assume that the characteristic admittance of each link line is the same. The diagonal admittance matrix of equation (2.12) is reduced to a unit matrix, and the coefficients of the symbolic scattering matrix for the condensed node are reduced to  $a_n = c_n = 0$ ,  $b_n = d_n = 0.5$ ,  $n = 1 \sim 6$ . Assuming that the characteristic admittance of each link line equals the intrinsic admittance of the medium and the propagation constants on each branch are the same for both orthogonal polarisations, then the propagation constants are solved from a system of equations (2.16) - (2.18), i.e.,

$$\begin{aligned}\gamma_x &= \frac{k_0}{2} \left( \frac{v^2 + w^2}{vw} - \frac{vw}{u^2} \right) \\ \gamma_y &= \frac{k_0}{2} \left( \frac{u^2 + w^2}{uw} - \frac{uw}{v^2} \right) \\ \gamma_z &= \frac{k_0}{2} \left( \frac{u^2 + v^2}{uv} - \frac{uv}{w^2} \right)\end{aligned}\tag{2.19}$$

where  $\gamma_x, \gamma_y, \gamma_z$  are the propagation constants in  $x$ ,  $y$ , and  $z$  directions, respectively. In general, the propagation constants could be complex if  $\epsilon$  and  $\mu$  are complex numbers to model electric and magnetic losses.

Knowing the propagation constants on all link transmission lines, we move the reference planes from the centre of the node to the ports of the node. Thus,

$${}_p V^r = [S_p] \cdot {}_p V^i\tag{2.20}$$

where  ${}_p V^r, {}_p V^i$  are, respectively, the vectors of the reflected and incident voltages at the 12 ports of the node.  $S_p$  is the complete scattering matrix of the symmetrical condensed FDTLM node which is shown as follows:

$$S_p = \frac{1}{2} \begin{array}{c} \begin{array}{cccccccccccc} +xy & +xz & -xy & -xz & +yz & +yx & -yz & -yx & +zx & +zy & -zx & -zy \\ & & & & & \lambda_{xy} & & -\lambda_{xy} & & \lambda_{xz} & & \lambda_{xz} \\ & & & & \lambda_{xy} & & \lambda_{xy} & & \lambda_{xz} & & -\lambda_{xz} & & \lambda_{xz} \\ & & & & -\lambda_{xy} & & & \lambda_{xy} & & \lambda_{xz} & & \lambda_{xz} & & \lambda_{xz} \\ & & & & \lambda_{xy} & & & & & \lambda_{yz} & & \lambda_{yz} & & -\lambda_{yz} \\ & \lambda_{xy} & & & & & & & & \lambda_{yz} & & \lambda_{yz} & & \lambda_{yz} \\ -\lambda_{xy} & \lambda_{xy} & -\lambda_{xy} & & & & & & & & & & & \lambda_{yz} \\ & \lambda_{xz} & & & & & & & & & & & & \lambda_{yz} \\ \lambda_{xz} & & \lambda_{xz} & -\lambda_{xz} & & \lambda_{yz} & & & \lambda_{yz} & & & & & \lambda_{yz} \\ & -\lambda_{xz} & & & & \lambda_{yz} & & & -\lambda_{yz} & & & & & \lambda_{yz} \\ \lambda_{xz} & & \lambda_{xz} & & -\lambda_{yz} & & \lambda_{yz} & & & & & & & \lambda_{yz} \end{array} \\ \begin{array}{c} +xy \\ +xz \\ -xy \\ -xz \\ +yz \\ +yx \\ -yz \\ -yx \\ +zx \\ +zy \\ -zx \\ -zy \\ +xy \\ +xz \\ -xy \\ -xz \\ +yz \\ +yx \\ -yz \\ -yx \\ +zx \\ +zy \\ -zx \\ -zy \end{array} \end{array} \quad (2.21)$$

where

$$\begin{aligned} \lambda_{xy} &= e^{-j(\gamma_x \cdot u/2 + \gamma_y \cdot v/2)} \\ \lambda_{xz} &= e^{-j(\gamma_x \cdot u/2 + \gamma_z \cdot w/2)} \\ \lambda_{yz} &= e^{-j(\gamma_y \cdot v/2 + \gamma_z \cdot w/2)} \end{aligned}$$

**The Propagation Constant Node** In contrast to the previous approach, we now chose different characteristic admittances of the link lines and then satisfying:

$$\begin{aligned} Y_{d1} &= \frac{w}{v} Y_0, & Y_{d2} &= \frac{v}{w} Y_0 \\ Y_{d3} &= \frac{u}{w} Y_0, & Y_{d4} &= \frac{w}{u} Y_0 \\ Y_{d5} &= \frac{v}{u} Y_0, & Y_{d6} &= \frac{u}{v} Y_0 \end{aligned} \quad (2.22)$$

Combining equations (2.22) with (2.16) - (2.18), it is evident that the propagation constants of all link lines are the same and equal to 1/2 the intrinsic propagation constant  $k_0$ . Hence, the complete scattering matrix of the propagation constant node is given as:

$$S_p = \begin{pmatrix} a_1\lambda_{xx} & & c_1\lambda_{xx} & & d_4\lambda_{xy} & & -d_4\lambda_{xy} & & b_6\lambda_{xz} & & b_6\lambda_{xz} \\ & a_2\lambda_{xx} & & c_2\lambda_{xx} & b_3\lambda_{xy} & & b_3\lambda_{xy} & & d_5\lambda_{xz} & & -d_5\lambda_{xz} \\ c_1\lambda_{xx} & & a_1\lambda_{xx} & & -d_4\lambda_{xy} & & d_4\lambda_{xy} & & b_6\lambda_{xz} & & b_6\lambda_{xz} \\ & c_2\lambda_{xx} & & a_2\lambda_{xx} & b_3\lambda_{xy} & & b_3\lambda_{xy} & & -d_5\lambda_{xz} & & d_5\lambda_{xz} \\ & b_2\lambda_{xy} & & b_2\lambda_{xy} & a_3\lambda_{yy} & & c_3\lambda_{yy} & & d_6\lambda_{yz} & & -d_6\lambda_{yz} \\ d_1\lambda_{xy} & & -d_1\lambda_{xy} & & a_4\lambda_{yy} & & c_4\lambda_{yy} & & b_5\lambda_{yz} & & b_5\lambda_{yz} \\ & b_2\lambda_{xy} & & b_2\lambda_{xy} & c_3\lambda_{yy} & & a_3\lambda_{yy} & & -d_6\lambda_{yz} & & d_6\lambda_{yz} \\ -d_1\lambda_{xy} & & d_1\lambda_{xy} & & c_4\lambda_{yy} & & a_4\lambda_{yy} & & b_5\lambda_{yz} & & b_5\lambda_{yz} \\ & d_2\lambda_{xz} & & -d_2\lambda_{xz} & b_4\lambda_{yz} & & b_4\lambda_{yz} & & a_5\lambda_{zz} & & c_5\lambda_{zz} \\ d_1\lambda_{xz} & & b_1\lambda_{xz} & & d_3\lambda_{yz} & & -d_3\lambda_{yz} & & a_6\lambda_{zz} & & c_6\lambda_{zz} \\ & -d_2\lambda_{xz} & & d_2\lambda_{xz} & b_4\lambda_{yz} & & b_4\lambda_{yz} & & c_5\lambda_{zz} & & a_5\lambda_{zz} \\ b_1\lambda_{xz} & & b_1\lambda_{xz} & & -d_3\lambda_{yz} & & d_3\lambda_{yz} & & c_6\lambda_{zz} & & a_6\lambda_{zz} \end{pmatrix} \quad (2.23)$$

where

$$\begin{aligned} \lambda_{xx} &= e^{-j\frac{k_0}{2}u} & \lambda_{xy} &= e^{-j\frac{k_0}{4}(u+v)} \\ \lambda_{yy} &= e^{-j\frac{k_0}{2}v} & \lambda_{xz} &= e^{-j\frac{k_0}{4}(u+w)} \\ \lambda_{zz} &= e^{-j\frac{k_0}{2}w} & \lambda_{yz} &= e^{-j\frac{k_0}{4}(v+w)} \end{aligned}$$

### The Hybrid Node

The SCN in Fig.2.4 can also be considered as three shunt nodes and three series nodes that are coupled with each other at the center of the node [38]. Hence, we can define three characteristic admittances corresponding to three series nodes, i.e.,

$$\begin{aligned} Y_{d1} &= Y_{d4} = \frac{sw}{uv} \sqrt{\frac{\epsilon}{\mu}} \\ Y_{d2} &= Y_{d5} = \frac{sv}{uw} \sqrt{\frac{\epsilon}{\mu}} \\ Y_{d3} &= Y_{d6} = \frac{su}{vw} \sqrt{\frac{\epsilon}{\mu}} \end{aligned} \quad (2.24)$$

where  $s = \sqrt{(u^2v^2 + u^2w^2 + v^2w^2) / (u^2 + v^2 + w^2)}$ .  $Y_{d1}, Y_{d4}$  are associated with the z-direction series node including the  $\pm xy$  and  $\pm yx$  polarized directions;  $Y_{d2}, Y_{d5}$  are associated with the y-direction series node including the  $\pm xz$  and  $\pm zx$  polarized directions; and  $Y_{d3}, Y_{d6}$  are associated with the z-direction series node including the  $\pm yz$  and  $\pm zy$  polarized directions. Therefore the variables of the symbolic scattering matrix is now simplified as follows:

$$\begin{aligned}
 a_1 &= \frac{Y_{d1} - Y_{d6}}{2(Y_{d1} + Y_{d6})} , & c_1 &= a_1 & a_2 &= \frac{Y_{d2} - Y_{d3}}{2(Y_{d2} + Y_{d3})} , & c_2 &= a_2 \\
 b_1 &= \frac{Y_{d1}}{Y_{d1} + Y_{d6}} , & d_1 &= \frac{1}{2} & b_2 &= \frac{Y_{d2}}{Y_{d2} + Y_{d3}} , & d_2 &= \frac{1}{2} \\
 a_3 &= \frac{Y_{d3} - Y_{d2}}{2(Y_{d3} + Y_{d2})} , & c_3 &= a_3 & a_4 &= \frac{Y_{d4} - Y_{d5}}{2(Y_{d4} + Y_{d5})} , & c_4 &= a_4 \\
 b_3 &= \frac{Y_{d3}}{Y_{d3} + Y_{d2}} , & d_3 &= \frac{1}{2} & b_4 &= \frac{Y_{d4}}{Y_{d4} + Y_{d5}} , & d_4 &= \frac{1}{2} \\
 a_5 &= \frac{Y_{d5} - Y_{d4}}{2(Y_{d5} + Y_{d4})} , & c_5 &= a_5 & a_6 &= \frac{Y_{d6} - Y_{d1}}{2(Y_{d6} + Y_{d1})} , & c_6 &= a_6 \\
 b_5 &= \frac{Y_{d5}}{Y_{d5} + Y_{d4}} , & d_5 &= \frac{1}{2} & b_6 &= \frac{Y_{d6}}{Y_{d6} + Y_{d1}} , & d_6 &= \frac{1}{2}
 \end{aligned} \tag{2.25}$$

Again, a similar analysis may be carried out to find the propagation constants on the link lines for the hybrid node. The propagation constants of all link transmission lines are derived to give

$$\begin{aligned}
 \gamma_{xy} &= \frac{su}{u^2 + v^2} k_0 , & \gamma_{yx} &= \frac{sv}{u^2 + v^2} k_0 \\
 \gamma_{xz} &= \frac{uv^2}{s(u^2 + v^2)} k_0 , & \gamma_{zx} &= \frac{w(u^2 + v^2 - s^2)}{s(u^2 + v^2)} k_0 \\
 \gamma_{yz} &= \frac{vu^2}{s(u^2 + v^2)} k_0 , & \gamma_{zy} &= \gamma_{zx}
 \end{aligned} \tag{2.26}$$

Finally, the complete scattering matrix of the hybrid node is obtained as:

$$S_p = \begin{vmatrix} a_1\lambda_{11} & & c_1\lambda_{11} & & d_4\lambda_{41} & & -d_4\lambda_{41} & & b_6\lambda_{61} & & b_6\lambda_{61} \\ & a_2\lambda_{21} & & c_2\lambda_{21} & b_3\lambda_{31} & & b_3\lambda_{31} & & d_5\lambda_{51} & & -d_5\lambda_{51} \\ c_1\lambda_{11} & & a_1\lambda_{11} & & -d_4\lambda_{41} & & d_4\lambda_{41} & & b_6\lambda_{61} & & b_6\lambda_{61} \\ & c_2\lambda_{21} & & a_2\lambda_{21} & b_3\lambda_{31} & & b_3\lambda_{31} & & -d_5\lambda_{51} & & d_5\lambda_{51} \\ & b_2\lambda_{22} & & b_2\lambda_{22} & a_3\lambda_{32} & & c_3\lambda_{32} & & d_6\lambda_{62} & & -d_6\lambda_{62} \\ d_1\lambda_{12} & & -d_1\lambda_{12} & & a_4\lambda_{42} & & c_4\lambda_{42} & & b_5\lambda_{52} & & b_5\lambda_{52} \\ & b_2\lambda_{22} & & b_2\lambda_{22} & c_3\lambda_{32} & & a_3\lambda_{32} & & -d_6\lambda_{62} & & d_6\lambda_{62} \\ -d_1\lambda_{12} & & d_1\lambda_{12} & & c_4\lambda_{42} & & a_4\lambda_{42} & & b_5\lambda_{52} & & b_5\lambda_{52} \\ & d_2\lambda_{23} & & -d_2\lambda_{23} & b_4\lambda_{43} & & b_4\lambda_{43} & & a_5\lambda_{53} & & c_5\lambda_{53} \\ b_1\lambda_{13} & & b_1\lambda_{13} & & d_3\lambda_{33} & & -d_3\lambda_{33} & & a_6\lambda_{63} & & c_6\lambda_{63} \\ & -d_2\lambda_{23} & & d_2\lambda_{23} & b_4\lambda_{43} & & b_4\lambda_{43} & & c_5\lambda_{53} & & a_5\lambda_{53} \\ b_1\lambda_{13} & & b_1\lambda_{13} & & -d_3\lambda_{33} & & d_3\lambda_{33} & & c_6\lambda_{63} & & a_6\lambda_{63} \end{vmatrix} \quad (2.27)$$

where

$$\begin{aligned} \lambda_{11} &= e^{-j\gamma_{xy}u}, \quad \lambda_{12} = e^{-j(\gamma_{xy}u/2 + \gamma_{yx}v/2)}, \quad \lambda_{13} = e^{-j(\gamma_{xy}u/2 + \gamma_{yx}w/2)} \\ \lambda_{21} &= e^{-j\gamma_{yx}u}, \quad \lambda_{22} = e^{-j(\gamma_{yx}u/2 + \gamma_{xy}v/2)}, \quad \lambda_{23} = e^{-j(\gamma_{yx}u/2 + \gamma_{xy}w/2)} \\ \lambda_{32} &= e^{-j\gamma_{yx}v}, \quad \lambda_{31} = e^{-j(\gamma_{yx}v/2 + \gamma_{xy}u/2)}, \quad \lambda_{33} = e^{-j(\gamma_{yx}v/2 + \gamma_{xy}w/2)} \\ \lambda_{42} &= e^{-j\gamma_{yx}v}, \quad \lambda_{41} = e^{-j(\gamma_{yx}v/2 + \gamma_{xy}u/2)}, \quad \lambda_{43} = e^{-j(\gamma_{yx}v/2 + \gamma_{xy}w/2)} \\ \lambda_{53} &= e^{-j\gamma_{yx}w}, \quad \lambda_{51} = e^{-j(\gamma_{yx}w/2 + \gamma_{xy}u/2)}, \quad \lambda_{52} = e^{-j(\gamma_{yx}w/2 + \gamma_{xy}v/2)} \\ \lambda_{63} &= e^{-j\gamma_{yx}w}, \quad \lambda_{61} = e^{-j(\gamma_{yx}w/2 + \gamma_{xy}u/2)}, \quad \lambda_{62} = e^{-j(\gamma_{yx}w/2 + \gamma_{xy}v/2)} \end{aligned}$$

We have considered three characteristic admittances for three series nodes to construct the hybrid FDTLM node. A similar analysis can also be performed by considering three shunt nodes.

## 2.4 Accuracy Assessment and Comparison of Various SCNs

If space continuous equations such as Maxwell's equations are discretized, some error is introduced. Like all other numerical techniques that are based on space discretization, also the TLM method is subject to the various sources of error due to this approximation and must be applied with caution in order to yield reliable and accurate results. In general, there are three types of errors in

the TLM simulation using the SCN: the truncation error, the velocity error, and the coarseness error.

A truncation error, which is the truncation of the time iteration, occurs only in the TDTLM simulation. This error does not occur in the FDTLM simulation.

A velocity error is introduced due to the fact that the velocity of waves through the mesh depends on both the frequency and the direction of propagation. Therefore, the space to be discretized and the frequency range of interest should be considered during the layout of the TLM mesh.

The coarseness error is directly related to the space resolution. To reduce this error, a fine mesh must be used to resolve rapid variations of the field distribution.

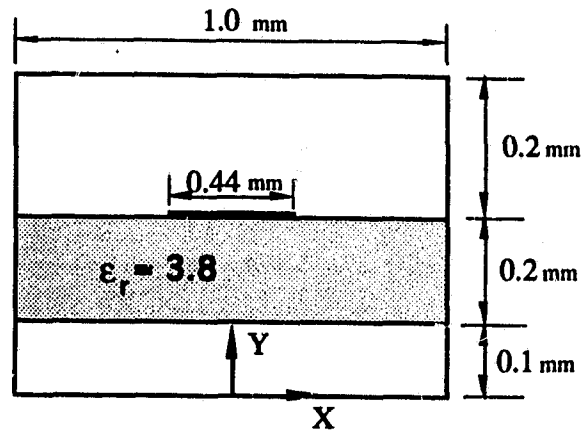
A measure of the accuracy of the TLM modeling is given by the value of the propagation constant of a plane wave traveling through the mesh along the coordinate axis direction. This analysis has been done for the 3D symmetrical condensed node [20]. However, the dispersion error analysis is only associated with a single node, that is, the procedure is local.

To test the various frequency-domain nodes, the structure in Fig.2.6 has been chosen. It is noted that the dominant mode has an even symmetry of the tangential electric field at  $x=0$ . The layout of the TLM mesh for half of the structure is shown in Fig.2.6(b). To allow a better comparison, the mesh size is first chosen deliberately large. The number of nodes in  $x$ -direction is 4, with a graded mesh size ranging from (from the centre to the right wall) 0.11mm, 0.11mm, 0.12mm, 0.16mm, respectively. The number of nodes in  $y$ -direction is 5, with the mesh size ranging from (from bottom to top) 0.1mm, 0.12mm, 0.08mm, 0.08mm, 0.12mm, respectively. Table 2.1(a) illustrates that the numerical solutions for all frequency-domain condensed nodes are slightly higher than the results given by the standard spectral-domain approach (SDA). The results obtained from the frequency-domain hybrid node (#1) are closer to the SDA results than those obtained with the others. At low frequency, the error is due mainly to the coarseness error. Results from the propagation constant node (#3) and the modified time-domain condensed node (#4) are slightly better than those from the characteristic admittance node (#2). But when the frequency increases,

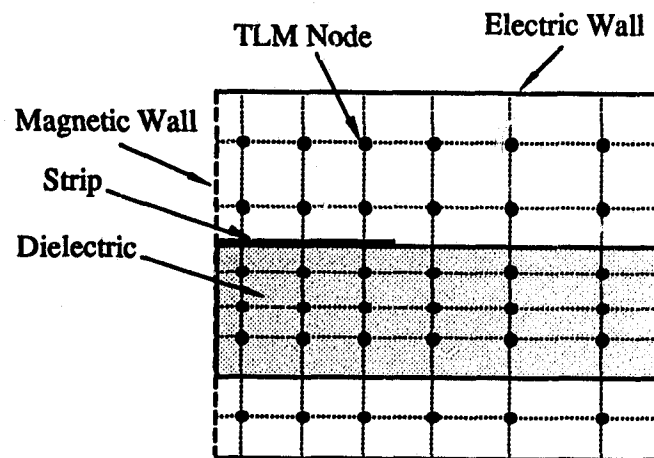
the velocity error clearly appears in the case of all the nodes. For the #2 node the velocity error is maximum.

Table 2.1(b) shows results for a large number of mesh points. The number of nodes in x-direction is 8, with a graded mesh size ranging from (from the centre to the right wall ) 0.055mm, 0.055mm, 0.055mm, 0.055mm, 0.055mm, 0.065mm, 0.075mm, 0.085mm, respectively. The number of nodes in y-direction is 7, with the mesh size ranging from (from bottom to top) 0.1mm, 0.08mm, 0.07mm, 0.05mm, 0.05mm, 0.07mm, 0.08mm, respectively. It can be seen that the results converge better to the SDA results. Table 2.1(b) also shows that the FDTLM results of all the nodes agree to within 5.5% with the results of the SDA at all frequency points. This error can be further reduced to any level desired by the use of a finer mesh.

In this section the four kinds of 3D FDTLM nodes available to date have been tested. The characteristic admittance node is by far the simplest resulting in a node scattering matrix which is symmetrical. This property can be exploited to decouple the FDTLM algorithm (the detailed procedure will be given in the next chapter). On the other hand, this node also produces the largest node dispersion. The frequency-domain hybrid node is slightly more accurate than the others. A drawback is that the link lines have different characteristic admittances and propagation constants which leads to the most complex node scattering matrix. Thus, all nodes have advantages and drawbacks. The choice is essentially governed by the structure under study and by the computer resource available. For example, for the TLM mesh discretization of the rectangular waveguide, an accurate solution can be obtained by using the simplest characteristic admittance node with the least CPU time and memory space. This is because of the simple mode field distributions (TE and TM modes) of the rectangular waveguide. The error of the node dispersion will be not obvious for these rectangular waveguide modes. However, for planar transmission line structures like the microstrip, the high concentration of the electric field near the corner of the conductor (Fig.2.6) requires a dense mesh, and thus a large ratio between the size of the smallest to the largest node is needed, which leads to large node dispersion error. Therefore, the use of the hybrid node is the best choice.



(a)



(b)

Fig. 2.6 (a) Cross-section of a suspended stripline  
(b) Layout of the TLM graded mesh

Table 2.1(a)

*The dispersion characteristics  $\lambda_0 / \lambda_g$  of a suspended stripline  
obtained with the different symmetrical condensed node*

F (GHz)	Results of different SCNs with (4 x 5) mesh				Results of SDA	Errors compared with the SDA (%)			
	#1	#2	#3	#4		#1	#2	#3	#4
40	1.4472	1.4799	1.4697	1.4663	1.3491	6.46	8.84	8.21	7.99
60	1.4629	1.5000	1.4900	1.4866	1.3602	7.02	9.32	8.71	8.50
80	1.4866	1.5297	1.5166	1.5133	1.3784	7.29	9.89	9.11	8.91
100	1.5166	1.5653	1.5492	1.5460	1.4036	7.45	10.33	9.40	9.21
120	1.5492	1.6062	1.5875	1.5843	1.4283	7.81	11.08	10.03	9.85
140	1.5875	1.6523	1.6310	1.6279	1.4560	9.28	11.88	10.73	10.56

#1 : The frequency domain hybrid node  
 #2 : The frequency domain characteristic admittance node  
 #3 : The frequency domain propagation constant node  
 #4 : The modified time domain symmetrical condensed node

Table 2.1(b)

*The dispersion characteristics  $\lambda_0 / \lambda_g$  of a suspended stripline  
obtained with the different symmetrical condensed node*

F (GHz)	Results of different SCNs with ( 8 x 7 ) mesh				Results of SDA	Errors compared with theSDA ( % )			
	#1	#2	#3	#4		#1	#2	#3	#4
40	1.3928	1.4107	1.4071	1.4071	1.3491	3.14	4.37	4.13	4.13
60	1.4107	1.4283	1.4248	1.4212	1.3602	3.58	4.77	4.54	4.30
80	1.4318	1.4491	1.4457	1.4457	1.3784	3.60	4.88	4.65	4.65
100	1.4560	1.4765	1.4731	1.4697	1.4036	3.73	4.94	4.72	4.70
120	1.4900	1.5067	1.5033	1.5000	1.4283	3.99	5.20	4.99	4.78
140	1.5166	1.5395	1.5362	1.5330	1.4560	4.14	5.42	5.22	5.02

#1 : The frequency domain hybrid node  
 #2 : The frequency domain characteristic admittance node  
 #3 : The frequency domain propagation constant node  
 #4 : The modified time domain symmetrical condensed node

## Chapter 3

# THE FREQUENCY-DOMAIN TLM ALGORITHM

### 3.1 The Concept of Intrinsic Scattering Matrix

The FDTLM algorithm is based on the concept of the intrinsic scattering matrix, which is defined as the coefficient matrix relating the reflected and incident waves at the exterior branches of a TLM network. By establishing the intrinsic scattering matrix, the original large network problem is transformed into a matrix algebra one, and all the properties of the structure can be readily computed through matrix operations. This offers the possibility to use numerous advanced techniques in matrix algebra to enhance the computational efficiency of the FDTLM algorithm. Furthermore, the diakoptics technique may be easily implemented in the algorithm. The entire structure may be broken up into several substructures. The intrinsic scattering matrix for each substructure is calculated and the one for the entire structure is obtained through simple matrix operations. Due to this property of the FDTLM algorithm, the computer storage required in the computation is only linearly proportional to the volume of the structure. This makes the FDTLM method very attractive and efficient in handling structures with complex configurations and large volumes.

Reviewing the original work in [16], Jin and Vahldieck consider a space discretized by the TLM network with  $N$  exterior branches connecting the space to the surrounding space (Fig.3.1a). Therefore, the following relationship between incident and reflected waves holds:

$$V_r^i = S_{ISM} \cdot V_e^i \quad (3.1)$$

where  $V_e^i$  and  $V_r^i$  are the vectors of the incident and reflected waves at the exterior branches.  $S_{ISM}$  is defined as the intrinsic scattering matrix of the structure. To derive  $S_{ISM}$ , all the branches in the TLM mesh with SCN are classified into three types: interior, exterior and stub branches. Interior branches

connect the nodes within the mesh, while exterior branches connect the nodes in the mesh to the surrounding space. Stub branches are absorbed in one time step.

We define

$$\begin{bmatrix} V_i^r \\ V_e^r \\ V_s^r \end{bmatrix} = \begin{bmatrix} S_{11} & S_{12} & S_{13} \\ S_{21} & S_{22} & S_{23} \\ S_{31} & S_{32} & S_{33} \end{bmatrix} \cdot \begin{bmatrix} V_i^i \\ V_e^i \\ V_s^i \end{bmatrix} \quad (3.2)$$

where  $V_i^{i(r)}$ ,  $V_e^{i(r)}$  and  $V_s^{i(r)}$ , respectively, are the incident (reflected) voltage vectors of the interior, exterior and stub branches. To eliminate the  $V_i^i$  and  $V_s^i$ , we use the following relationship:

$$\begin{aligned} V_s^i &= \gamma \cdot V_e^i \\ V_i^i &= \gamma \cdot C \cdot V_i^r \end{aligned} \quad (3.3)$$

Therefore, from (3.2) and (3.3), a relationship can be established between  $V_e^i$  and  $V_e^r$ :

$$\begin{aligned} V_e^r &= S_{ISM} \cdot V_e^i = \{\gamma[S_{21} + \gamma S_{23} \cdot G \cdot S_{31}] \cdot C \cdot [1 - \gamma(S_{11} + \gamma S_{13} \cdot G \cdot S_{31}) \cdot C]^{-1} \\ &\quad \cdot [S_{12} + \gamma S_{13} \cdot G \cdot S_{32}] + S_{22} + \gamma S_{23} \cdot G \cdot S_{32}\} \cdot V_e^i \end{aligned} \quad (3.1)$$

where  $G = (1 - \gamma S_{33})^{-1}$ ,  $\gamma$  is the propagation factor on the node link lines.  $C$  is the connection matrix relating the interior branches.

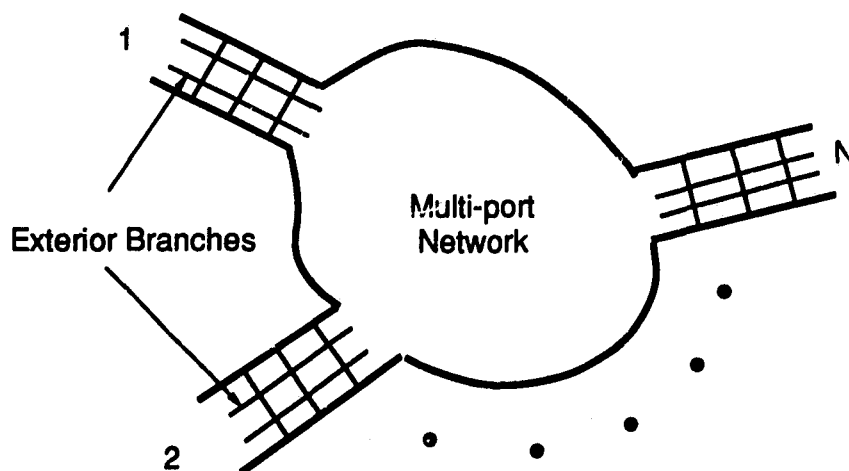


Fig. 3.1(a) Space discretized by the TLM network with  $N$  exterior branches connecting the discontinuity space to the surrounding space

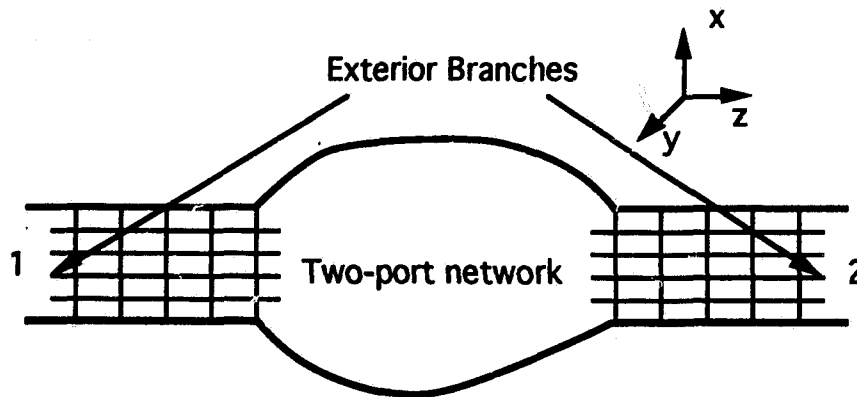


Fig. 3.1(b) Space discretized by the TLM network with two exterior branches connecting the discontinuity space to the surrounding space

Equation (3.1) provides an explicit expression of the intrinsic scattering matrix  $S_{ISM}$  for a multi-port network. For a two-port network problem (i.e. Fig.3.1b), the intrinsic scattering matrix can be simplified so that the size of the matrix of equation (3.1) is reduced. We define the coordinate z-axis as the propagation direction of the wave. The link lines of the symmetrical condensed FDTLM node (Fig.2.4) are classified into two types:

- exterior branches:      +zx, +zy, -zx, -zy.
- interior branches:      +xy, +xz, -xy, -xz;
- +yz, +yx, -yz, -yx.

The exterior branches point into the propagation direction of the wave, while the interior branches between neighboring nodes are connected through the following relationship

$$\begin{aligned} V_x^i &= C_x \cdot V_x^r \\ V_y^i &= C_y \cdot V_y^r \end{aligned} \quad (3.4)$$

Where  $C_x$  and  $C_y$  are the connection matrices which connect the neighboring branches in the x- and y- directions, respectively.  $V_{x,y}^i$ ,  $V_{x,y}^r$  are the incident and reflected voltages between neighboring nodes. Therefore, a modified intrinsic scattering matrix can be defined as follows:

$$\begin{bmatrix} V_z^r \\ V_x^r \\ V_y^r \end{bmatrix} = \begin{bmatrix} S_{zz} & S_{zx} & S_{zy} \\ S_{xz} & S_{xx} & S_{xy} \\ S_{yz} & S_{yx} & S_{yy} \end{bmatrix} \begin{bmatrix} V_z^i \\ V_x^i \\ V_y^i \end{bmatrix} \quad (3.5)$$

From equations (3.4) and (3.5), we can now find a relationship between incident and reflected voltages of exterior branches, which are the branches that point in propagation direction:

$$V_z^r = [S_{ISM}] \cdot V_z^i \quad (3.5a)$$

where

$$\begin{aligned} S_{ISM} = & S_{zz} + S_{zx} \cdot C_x \cdot P \cdot (M \cdot S_{zz} + M \cdot S_{zy} \cdot C_y \cdot N \cdot S_{yz}) \\ & + S_{zy} \cdot C_y \cdot Q \cdot (N \cdot S_{yz} + N \cdot S_{yx} \cdot C_x \cdot M \cdot S_{xz}) \end{aligned} \quad (3.5b)$$

and

$$\begin{aligned} M &= (I - S_{xx} \cdot C_x)^{-1} \\ N &= (I - S_{yy} \cdot C_y)^{-1} \\ P &= (I - M \cdot S_{xy} \cdot C_y \cdot N \cdot S_{yx} \cdot C_x)^{-1} \\ Q &= (I - N \cdot S_{yx} \cdot C_x \cdot M \cdot S_{xy} \cdot C_y)^{-1} \end{aligned}$$

Equation (3.5b) provides a simplified explicit expression for the intrinsic scattering matrix  $S_{ISM}$  in terms of the scattering and connection matrices of the network. For example, if we consider the cross-section of a guided structure discretized with the SCN mesh, then the size of the largest operating matrix  $S_{11}$  of equation (3.1) is  $8 \times n_x \times n_y$ , where  $n_x$  and  $n_y$  are the number of nodes in x- and y-directions, respectively. In contrast, in equation (3.5a), the size of the largest operating matrix is reduced to  $4 \times n_x \times n_y$ .

The intrinsic scattering matrix  $S_{ISM}$  fully characterizes the structure and plays a central role in the FDTLM algorithm. Once equation (3.5a) is obtained, the eigenvalues of a guiding structure can be determined and the scattering parameters for two guiding structures connected through a discontinuity can be computed. Details of this procedure for 2D and 3D problems will be described in the following two sections.

### 3.2 The FDTLM Algorithm for 2D Eigenvalue Problems

The FDTLM discretizes any guided structure as an infinitely long periodic network with a structural periodicity of  $d$  in the propagation direction ( along the  $z$ -axis ). Therefore, the intrinsic scattering matrix is constructed from only one slice of waveguide which contains only one node in the propagation direction as shown in Fig.3.2. For this case, the intrinsic scattering matrix of the unit cell reads:

$$\begin{bmatrix} V'_A \\ V'_B \end{bmatrix} = \begin{bmatrix} S_{AA} & S_{AB} \\ S_{AB} & S_{BB} \end{bmatrix} \cdot \begin{bmatrix} V^i_A \\ V^i_B \end{bmatrix} \quad (3.6)$$

where  $V^i_{A,B}$  denotes the incident voltage vector and  $V'_{A,B}$  the reflected voltage vector. To determine propagation constants and the transverse mode distribution in the guide, a transfer matrix, which is related to the scattering matrix, is obtained as follows:

$$\begin{bmatrix} V_A \\ I_A \end{bmatrix} = A \cdot \begin{bmatrix} V_B \\ I_B \end{bmatrix} = \begin{bmatrix} SR^{-1} & SR^{-1}S - R \\ R^{-1} & R^{-1}S \end{bmatrix} \cdot \begin{bmatrix} V_B \\ I_B \end{bmatrix} \quad (3.7)$$

where

$$\begin{aligned} S &= [(I - S_{AA}) - S_{AB}(I - S_{AA})^{-1}S_{AB}]^{-1}(I + S_{AA}) \\ &\quad - [(I - S_{AA})S_{AB}^{-1}(I - S_{AA}) - S_{AB}]^{-1}S_{AB} \\ R &= [(I - S_{AA}) - S_{AB}(I - S_{AA})^{-1}S_{AB}]^{-1}S_{AB} \\ &\quad - [(I - S_{AA})S_{AB}^{-1}(I - S_{AA}) - S_{AB}]^{-1}(I + S_{AA}) \end{aligned}$$

Let the propagation constant in  $z$ -direction be  $\theta$ , then the periodic boundary conditions based on Floquet's theorem imply that

$$\begin{bmatrix} V_B \\ I_B \end{bmatrix} = e^{j\theta d} \cdot \begin{bmatrix} V_A \\ I_A \end{bmatrix} \quad (3.8)$$

Thus, the transfer matrix of the unit cell must satisfy the eigenvalue equation

$$A \cdot \begin{bmatrix} V \\ I \end{bmatrix} = e^{j\theta d} \cdot \begin{bmatrix} V \\ I \end{bmatrix} \quad (3.9)$$

The solution of the eigenvalue equation (3.9) is simplified if we consider the analytical properties of the matrix  $A$ . We observe first of all that if (3.9) is satisfied, then the following eigenvalue equation is also satisfied.

$$\frac{1}{2}(A + A^{-1}) \cdot \begin{bmatrix} V \\ I \end{bmatrix} = \frac{1}{2}(e^{\theta d} + e^{-\theta d}) \cdot \begin{bmatrix} V \\ I \end{bmatrix} = \cosh(\theta d) \cdot \begin{bmatrix} V \\ I \end{bmatrix} \quad (3.10)$$

Inspection of equation (3.7) shows that the inverse matrix of  $A$  can be easily obtained by

$$A^{-1} = \begin{bmatrix} SR^{-1} & R - SR^{-1}S \\ -R^{-1} & R^{-1}S \end{bmatrix} \quad (3.11)$$

So that

$$\frac{1}{2}(A + A^{-1}) = \begin{bmatrix} SR^{-1} & 0 \\ 0 & R^{-1}S \end{bmatrix} \quad (3.12)$$

Thus, it is sufficient to consider the reduced eigenvalue equation

$$(SR^{-1}) \cdot V = \cosh(\theta d) \cdot V \quad (3.13)$$

Equation (3.13) is the standard form of an eigenvalue problem which, when solved, yields the transverse field distributions and the propagation constants of the modes supported by the structure at a given frequency. All modes of interest can thus be obtained by solving a single eigenvalue problem at a given frequency.

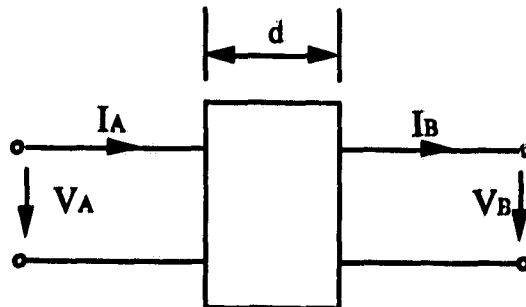


Fig. 3.2 A slice of waveguide structure

### 3.3 The FDTLM Algorithm for 3D Discontinuity Problems

The discontinuity under consideration is divided into the areas: 1) discontinuity region, and 2) longitudinal homogeneous waveguide attached to the discontinuity as the input and output ports. The first step in the S-parameter calculation is the solution of the cross-section eigenvalue problem for the chosen input and output waveguide structures. This yields the necessary mode field distributions over the cross-section. In the second step, the intrinsic scattering matrices of the discontinuity and the input and output waveguides are determined. In the third step, one of the ports is excited by the proper mode field distribution. From the reflected and the transmitted mode amplitudes the S-parameters can be found.

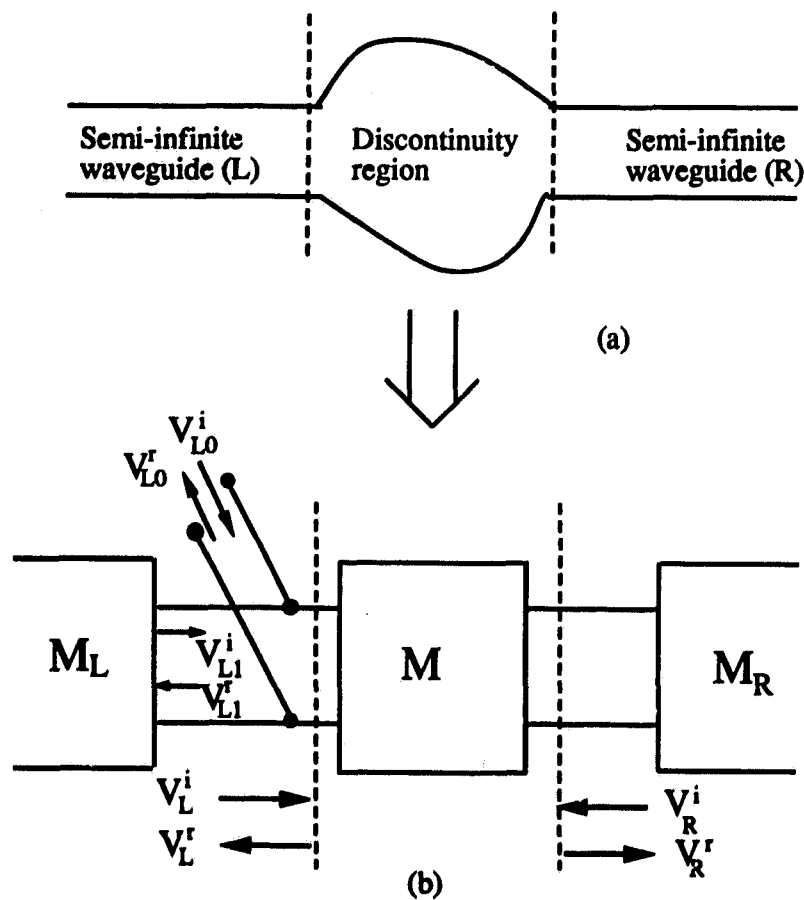


Fig. 3.3 Two-port waveguide discontinuity and equivalent network

For the case of a two-port waveguide discontinuity problem (Fig.3.3a), the method for evaluating the S-parameters is described extensively in [16,21], but for reasons of completeness the main steps are presented in the following.

The intrinsic scattering matrices for the discontinuity region and the two attached semi-infinite waveguides are denoted as  $M$ ,  $M_L$  and  $M_R$ , respectively. Matrix  $M_L$  or  $M_R$  can be constructed from the modes of the waveguide by taking a slice of the input or output waveguides. As described in the previous section, all the eigenvectors (modes) of a waveguide can be obtained by solving a single eigenvalue problem. Then an arbitrary wave can be expanded in the form of these eigenvectors. Assuming there are  $N$  pairs of solutions  $V_n^i, V_n^r$  ( $n=1,2,\dots,N$ ), the arbitrary wave is expanded as

$$V^i = [V_n^i] \cdot K \quad (3.14)$$

$$V^r = [V_n^r] \cdot K \quad (3.15)$$

where  $V^i$  and  $V^r$  are the incident and reflected wave vectors, matrices  $[V_n^i]$  and  $[V_n^r]$  are the collections of the column eigenvector  $V_n^i$  and  $V_n^r$ , respectively.  $K$  is the vector containing all the modal field coefficients of  $N$  pairs of waveguide modes. Eliminating  $K$  in (3.14) and (3.15), we establish the relationship between  $V^i$  and  $V^r$ :

$$V^r = [V_n^r] \cdot [V_n^i]^{-1} \cdot V^i \quad (3.16)$$

Thus, the matrices  $M_L$  and  $M_R$  for the input and output semi-infinite waveguides are defined by:

$$M_L = [V_{Ln}^r] \cdot [V_{Ln}^i]^{-1} \quad (3.17)$$

$$M_R = [V_{Rn}^r] \cdot [V_{Rn}^i]^{-1} \quad (3.18)$$

After the intrinsic scattering matrices of the discontinuity region and the two semi-infinite waveguides are found, the problem is simplified to a matrix algebra problem as illustrated in Fig.3.3b. The incident and reflected waves at the interfaces to the discontinuity region and the attached waveguides are related as follows:

$$\begin{bmatrix} V_L^r \\ V_R^r \end{bmatrix} = M \cdot \begin{bmatrix} V_L^i \\ V_R^i \end{bmatrix} = \begin{bmatrix} m_{LL} & m_{LR} \\ m_{RL} & m_{RR} \end{bmatrix} \cdot \begin{bmatrix} V_L^i \\ V_R^i \end{bmatrix} \quad (3.19)$$

where  $V_L^i, V_L^r$  are the incident and reflected wave vectors at the interface of the left-hand waveguide and the discontinuity region; while  $V_R^i, V_R^r$  are the incident and reflected wave vectors at the interface of the right-hand waveguide and the discontinuity region.

For the right-hand semi-infinite waveguide,  $V_R^i$  represents the incident wave vector, while  $V_R^r$  represents the reflected wave vector, hence:

$$V_R^i = M_R \cdot V_R^r \quad (3.20)$$

The excitation of the system,  $V_{L0}^i$  and  $V_{L0}^r$ , is incident at the interface between the left-hand waveguide and the discontinuity region (Fig.3.3b).  $V_{L0}^i$  and  $V_{L0}^r$  are the incident wave vector and reflected wave vector of the initial exciting modes, which can be obtained from the 2D eigenvalue analysis (section 3.2) of the left-hand waveguide. They can be related by:

$$V_{L0}^r = M_L \cdot V_{L0}^i \quad (3.21)$$

When the initial excitation injects at the interface between the left-hand waveguide and the discontinuity region, the reflected modes are introduced there. The incident and reflected wave vectors  $V_{L1}^i$  and  $V_{L1}^r$ , associated with the reflected modes are related by:

$$V_{L1}^i = M_L \cdot V_{L1}^r \quad (3.22)$$

Thus the total wave vectors  $V_L^i$  and  $V_L^r$  at the left-hand port is the sum of two parts:

$$V_L^i = V_{L0}^i + V_{L1}^i \quad (3.23)$$

$$V_L^r = V_{L0}^r + V_{L1}^r \quad (3.24)$$

Combining equations from (3.19) through (3.24), the reflected wave vector  $V_{L1}^r$  associated with the reflected modes at the left-hand port and the reflected wave vector  $V_R^r$  associated with the transmitted modes at the right-hand port are found from

$$V_{L1}^r = (M_L \cdot T_r - 1)^{-1} \cdot (M_L - T_r) \cdot V_{L0}^i \quad (3.25)$$

$$V_R^r = T_t \cdot (M_L \cdot V_{L1}^r + V_{L0}^i) \quad (3.26)$$

where

$$T_r = m_{LL} + m_{LR} \cdot M_R \cdot T_t$$

$$T_t = (1 - m_{RR} \cdot M_R)^{-1} \cdot m_{RL}$$

Note that the reflected wave vectors given by (3.25) and (3.26) are the total reflected fields containing all modes (including propagating modes and evanescent modes) of the corresponding waveguides. The modal field coefficients of a specific mode can be extracted by use of (3.15). In order to extract the scattering parameters, we normalize the modal field  $V_n^i$  and  $V_n^r$  such that the complex power carried in each of the modes equals 1. For example, the S-parameters of the first mode ( $V_{L0,1}^i$  and  $V_{L0,1}^r$ ) excitation are

$$S_{11} = k_1^r = [V_{Ln}^r]_{n=1}^{-1} \cdot V_{L1}^r \quad (3.27)$$

$$S_{21} = k_1^t = [V_{Rn}^r]_{n=1} \cdot V_{R,1}^r \quad (3.28)$$

where  $k_1^r$  and  $k_1^t$  are the first elements of  $K$  in (3.15).

### 3.4 Algorithm Development

#### — Decoupled Frequency Domain SCN and Solution Algorithm

The computational efficiency of the frequency-domain TLM method depends directly on the size of the matrix equations such as (3.1b) and (3.6). In particular, for cases in which the entire problem solution requires a fine space resolution (i.e. structures with inhomogeneous cross-sections, like microstrip lines etc.), the computation time can increase significantly. Although the computational efficiency of the FDTLM algorithm is still better than most known space discretization techniques, because several advanced matrix computation techniques can be implemented into the FDTLM algorithm [16,21], there is still a need to improve the computation time and memory space requirements in order

to make the method better suitable for optimization of passive microwave components.

To achieve this we are introducing a new FDTLM node representation, which is derived from the condensed characteristic admittance node. The node contains twelve link transmission lines and their interconnections are described by a scattering matrix of order 12. This scattering matrix represents an algebraic block, which must be connected to other blocks in the discretized space. To do this, we need to solve a large-scale interconnected network. Sometimes the order of this network matrix and the number of variables exceeds the available computer capacity even if sparse matrix solution techniques are being used.

In our new approach, however, we decouple the  $12 \times 12$  node scattering matrix into a pair of independent  $6 \times 6$  sub-matrices. This is possible by exploiting the symmetry properties of the 12-port characteristic admittance node s-matrix and the fact that in the FDTLM method stubs are no longer needed.

To explain this new algorithm, one has to remember that the FDTLM scattering procedure can be divided into 3 separated steps: step 1, incident waves propagate from the ports of the node to the center of the node; step 2, incident waves are scattered at the center of the node; step 3, reflected waves propagate from the center of the node to the ports. The first and third steps are equivalent to multiplying incident and reflected waves with an appropriate phase shift  $\gamma \Delta l / 2$ , where  $\gamma$  is the corresponding propagation constant and  $\Delta l$  is the mesh size. In the second step, the reflected waves are linearly related to the incident waves by a constant matrix. This matrix is identical to the scattering matrix given by P.B.Johns in the time domain TLM method for free space without stubs [17]. This matrix can be decoupled into two independent  $6 \times 6$  sub-matrices, and therefore the entire FDTLM algorithm can be constructed based on these two  $6 \times 6$  sub-matrices instead of the original  $12 \times 12$  matrix. As a result, the computer memory and CPU-time can be reduced. A detailed description of the decoupling procedure and the corresponding FDTLM algorithm is given in the following.

**Decoupling Procedure**

Once again we start from the frequency domain symmetrical condensed node shown in Fig.3.4. The frequency domain scattering matrix of the 12-port characteristic admittance node is rewritten here for convenience.

$$S = \frac{1}{2} \begin{matrix} \begin{matrix} +xy & +xz & -xy & -xz & +yz & +yx & -yz & -yx & +zx & +zy & -zx & -zy \\ \lambda_{xy} & \lambda_{xy} & -\lambda_{xy} & \lambda_{xy} & \lambda_{xy} & -\lambda_{xy} & \lambda_{xy} & \lambda_{xy} & -\lambda_{xz} & \lambda_{xz} & -\lambda_{xz} & \lambda_{xz} \\ -\lambda_{xy} & \lambda_{xz} & \lambda_{xz} & -\lambda_{xz} & \lambda_{yz} & \lambda_{yz} & -\lambda_{yz} & \lambda_{yz} & \lambda_{yz} & -\lambda_{yz} & \lambda_{yz} & \lambda_{yz} \\ \lambda_{xz} & -\lambda_{xz} & \lambda_{xz} & \lambda_{xz} & -\lambda_{yz} & \lambda_{yz} & \lambda_{yz} & -\lambda_{yz} & \lambda_{yz} & \lambda_{yz} & -\lambda_{yz} & \lambda_{yz} \\ \lambda_{xz} & \lambda_{xz} & -\lambda_{yz} & \lambda_{yz} & \lambda_{yz} & \lambda_{yz} & -\lambda_{yz} & \lambda_{yz} & \lambda_{yz} & \lambda_{yz} & -\lambda_{yz} & \lambda_{yz} \end{matrix} \end{matrix} \quad (3.29)$$

It is evident that the scattering matrix is symmetrical, which naturally leads to the use of diagonal voltage components to decompose the matrix as in [22]. The diagonal voltage components consist of the sum and the difference of two orthogonal polarized ports at the original node. This decomposition procedure is straightforward since the scattering matrix  $S$  is symmetrical, and thus there always exists an orthogonal matrix  $Q$  to perform the  $45^\circ$  rotation like  $Q \cdot S \cdot Q^{-1}$ . For the present case,  $Q$  is given by :

$$Q = \frac{1}{\sqrt{2}} \begin{bmatrix} 1 & 1 & 0 & 0 & 0 & 0 & 0 & 0 & 0 & 0 & 0 & 0 \\ 0 & 0 & 1 & -1 & 0 & 0 & 0 & 0 & 0 & 0 & 0 & 0 \\ 0 & 0 & 0 & 0 & 1 & 1 & 0 & 0 & 0 & 0 & 0 & 0 \\ 0 & 0 & 0 & 0 & 0 & 0 & 1 & -1 & 0 & 0 & 0 & 0 \\ 0 & 0 & 0 & 0 & 0 & 0 & 0 & 0 & 1 & 1 & 0 & 0 \\ 0 & 0 & 0 & 0 & 0 & 0 & 0 & 0 & 0 & 0 & 1 & -1 \\ 1 & -1 & 0 & 0 & 0 & 0 & 0 & 0 & 0 & 0 & 0 & 0 \\ 0 & 0 & 1 & 1 & 0 & 0 & 0 & 0 & 0 & 0 & 0 & 0 \\ 0 & 0 & 0 & 0 & 1 & -1 & 0 & 0 & 0 & 0 & 0 & 0 \\ 0 & 0 & 0 & 0 & 0 & 0 & 1 & 1 & 0 & 0 & 0 & 0 \\ 0 & 0 & 0 & 0 & 0 & 0 & 0 & 0 & 1 & -1 & 0 & 0 \\ 0 & 0 & 0 & 0 & 0 & 0 & 0 & 0 & 0 & 0 & 1 & 1 \end{bmatrix} \quad (3.30)$$

and the new scattering matrix after  $45^\circ$  rotation is given by:

$$Q \cdot S \cdot Q^{-1} = \frac{1}{2} \begin{bmatrix} 0 & 0 & \lambda_{xy} & \lambda_{xy} & \lambda_{xz} & -\lambda_{xz} & 0 & 0 & 0 & 0 & 0 & 0 \\ 0 & 0 & -\lambda_{xy} & -\lambda_{xy} & \lambda_{xz} & -\lambda_{xz} & 0 & 0 & 0 & 0 & 0 & 0 \\ \lambda_{xy} & \lambda_{xy} & 0 & 0 & \lambda_{yz} & \lambda_{yz} & 0 & 0 & 0 & 0 & 0 & 0 \\ \lambda_{xy} & \lambda_{xy} & 0 & 0 & -\lambda_{yz} & -\lambda_{yz} & 0 & 0 & 0 & 0 & 0 & 0 \\ \lambda_{xz} & \lambda_{xz} & \lambda_{yz} & -\lambda_{yz} & 0 & 0 & 0 & 0 & 0 & 0 & 0 & 0 \\ -\lambda_{xz} & -\lambda_{xz} & \lambda_{yz} & -\lambda_{yz} & 0 & 0 & 0 & 0 & 0 & 0 & 0 & 0 \\ 0 & 0 & 0 & 0 & 0 & 0 & 0 & 0 & -\lambda_{xy} & -\lambda_{xy} & -\lambda_{xz} & \lambda_{xz} \\ 0 & 0 & 0 & 0 & 0 & 0 & 0 & 0 & \lambda_{xy} & \lambda_{xy} & -\lambda_{xz} & \lambda_{xz} \\ 0 & 0 & 0 & 0 & 0 & 0 & -\lambda_{xy} & \lambda_{xy} & 0 & 0 & -\lambda_{yz} & -\lambda_{yz} \\ 0 & 0 & 0 & 0 & 0 & 0 & -\lambda_{xy} & \lambda_{xy} & 0 & 0 & \lambda_{yz} & \lambda_{yz} \\ 0 & 0 & 0 & 0 & 0 & 0 & -\lambda_{xz} & -\lambda_{xz} & -\lambda_{yz} & \lambda_{yz} & 0 & 0 \\ 0 & 0 & 0 & 0 & 0 & 0 & \lambda_{xz} & \lambda_{xz} & -\lambda_{yz} & \lambda_{yz} & 0 & 0 \end{bmatrix} \quad (3.31)$$

Correspondingly, the incident and reflected waves  $V^i$  and  $V^r$  at the ports of the node are transformed into

$$\begin{aligned} U^i &= Q \cdot V^i \\ U^r &= Q \cdot V^r \end{aligned} \quad (3.32)$$

It is readily shown that vectors  $U^i$  and  $U^r$  are related by:

$$U^r = Q \cdot S \cdot Q^{-1} \cdot U^i \quad (3.33)$$

A direct result of the transformation above is that the new vectors  $U^i$  and  $U^r$  can be decoupled into two independent groups which are related, respectively, by:

$$\begin{aligned} U_A^r &= S_A \cdot U_A^i \\ U_B^r &= S_B \cdot U_B^i \end{aligned} \quad (3.34)$$

where

$$U_A^{i(r)} = \begin{bmatrix} V_{+xy}^{i(r)} + V_{+xz}^{i(r)} \\ V_{-xy}^{i(r)} - V_{-xz}^{i(r)} \\ V_{+yz}^{i(r)} + V_{+yz}^{i(r)} \\ V_{-yz}^{i(r)} - V_{-yz}^{i(r)} \\ V_{+xz}^{i(r)} + V_{+yz}^{i(r)} \\ V_{-xz}^{i(r)} - V_{-yz}^{i(r)} \end{bmatrix} \quad S_A = \frac{1}{2} \begin{bmatrix} 0 & 0 & \lambda_{xy} & \lambda_{xy} & \lambda_{xz} & -\lambda_{xz} \\ 0 & 0 & -\lambda_{xy} & -\lambda_{xy} & \lambda_{xz} & -\lambda_{xz} \\ \lambda_{xy} & -\lambda_{xy} & 0 & 0 & \lambda_{yz} & \lambda_{yz} \\ \lambda_{xy} & -\lambda_{xy} & 0 & 0 & -\lambda_{yz} & -\lambda_{yz} \\ \lambda_{xz} & \lambda_{xz} & \lambda_{yz} & -\lambda_{yz} & 0 & 0 \\ -\lambda_{xz} & -\lambda_{xz} & \lambda_{yz} & -\lambda_{yz} & 0 & 0 \end{bmatrix}$$

$$U_B^{i(r)} = \begin{bmatrix} V_{+xy}^{i(r)} - V_{+xz}^{i(r)} \\ V_{-xy}^{i(r)} + V_{-xz}^{i(r)} \\ V_{+yz}^{i(r)} - V_{+zx}^{i(r)} \\ V_{-yz}^{i(r)} + V_{-zx}^{i(r)} \\ V_{+xz}^{i(r)} - V_{+xy}^{i(r)} \\ V_{-xz}^{i(r)} + V_{-xy}^{i(r)} \end{bmatrix} \quad S_B = \frac{1}{2} \begin{bmatrix} 0 & 0 & -\lambda_{xy} & -\lambda_{xy} & -\lambda_{xz} & \lambda_{xz} \\ 0 & 0 & \lambda_{xy} & \lambda_{xy} & -\lambda_{xz} & \lambda_{xz} \\ -\lambda_{xy} & \lambda_{xy} & 0 & 0 & -\lambda_{yz} & -\lambda_{yz} \\ -\lambda_{xy} & \lambda_{xy} & 0 & 0 & \lambda_{yz} & \lambda_{yz} \\ -\lambda_{xz} & -\lambda_{xz} & -\lambda_{yz} & \lambda_{yz} & 0 & 0 \\ \lambda_{xz} & \lambda_{xz} & -\lambda_{yz} & \lambda_{yz} & 0 & 0 \end{bmatrix}$$

Hence, the 12-port SCN (Fig.3.4) is now decoupled into a pair of independent 6-port nodes (*A* and *B*) as shown in Fig.3.5. It should be noted that matrix  $S_A$  is simply the negative of matrix  $S_B$ , which allows to derive the entire FDTLM algorithm from the discretization of the structure with the two pairs of 6-port nodes independently. This is a major advantage over the approach in section 3.3, where 12-port nodes needed to be connected, and the resulting matrix inversion was performed on a matrix twice the size of the one used in this new algorithm.

**Solution Algorithm** The 2D case is used to illustrate the implementation of the new FDTLM algorithm using the pair of independent 6-port nodes, which involves only one slice of the structure analyzed. The resulting equivalent electrical network is shown in Fig.3.6 (in this case we use the example of a ridged waveguide). It should be mentioned that nodes *A* and *B* should be arranged in such a way that each of them is followed by the other as indicated in Fig.3.6. The reason for this is that the vector  $U$  at the ports of node *A* is always orthogonal to the vector  $U$  at the same ports of node *B*. Also, the vector  $U$  at one port is always orthogonal to the vector at the opposing port. Consecutive arrangement of nodes *A* and *B* must be done in such a way as to ensures that the vector  $U$  at the node boundary has the same direction as the one of the adjacent node.

It has been shown (i.e. [21]) that the main procedure in the FDTLM algorithm is to calculate the intrinsic scattering matrix. This step consumes large portions of the overall CPU-time. Thus, the decoupling procedure introduced above represents an efficient method to reduce the size of the operating matrices and hence computation time. The procedure for the calculation of the intrinsic scattering matrix in the new FDTLM method using a pair of  $6 \times 6$  nodes is as follows. First, the structure analyzed is discretized by filling the space with an array of nodes *A* and *B* as shown in Fig.3.6(a). The corresponding intrinsic

scattering matrix is then obtained. Next, with the same mesh layout but the positions of nodes *A* and *B* changed as shown in Fig.3.6(b), the intrinsic scattering matrix is calculated again. Both matrices are then combined, which gives the complete intrinsic scattering matrix.

To test the procedure numerically, the propagation constant of the dominant mode for a standard rectangular waveguide partially filled with a dielectric slab (Fig.3.7a) was computed at 10 GHz. It is noted that the dominant mode in the structure is the distorted  $TE_{10}$  mode in the unloaded rectangular waveguide. This mode has an even symmetry of the tangential electric field at  $x=a/2$ . Thus utilizing the symmetry of the structure, the number of nodes in *x* direction is 6, with graded mesh sizes ranging from (from the center to the right wall) 1.70mm, 1.73 mm, 1.80 mm, 2.00 mm, 2.00 mm, 2.20 mm, respectively. The number of nodes in *y* direction is 5, with the mesh size ranging from (from bottom to top) 1.70mm, 1.69 mm, 1.69 mm, 2.54 mm, 2.54 mm, respectively. The layout of the TLM mesh is shown in Fig.3.7(b). For this problem, the conventional intrinsic scattering matrix algorithm in section 3.3 ended up with a matrix size of  $240 \times 240$ . In comparison, the new approach only resulted in a  $120 \times 120$  matrix. This clearly illustrates the reduction of operating matrix size with this new algorithm.

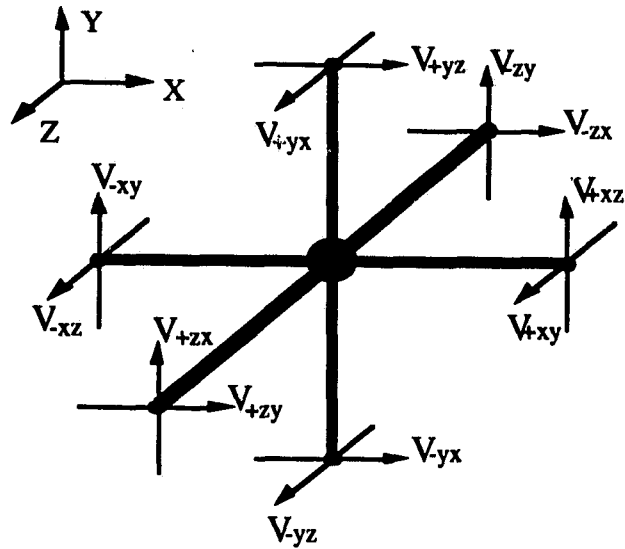


Fig. 3.4 The frequency domain symmetrical condensed node

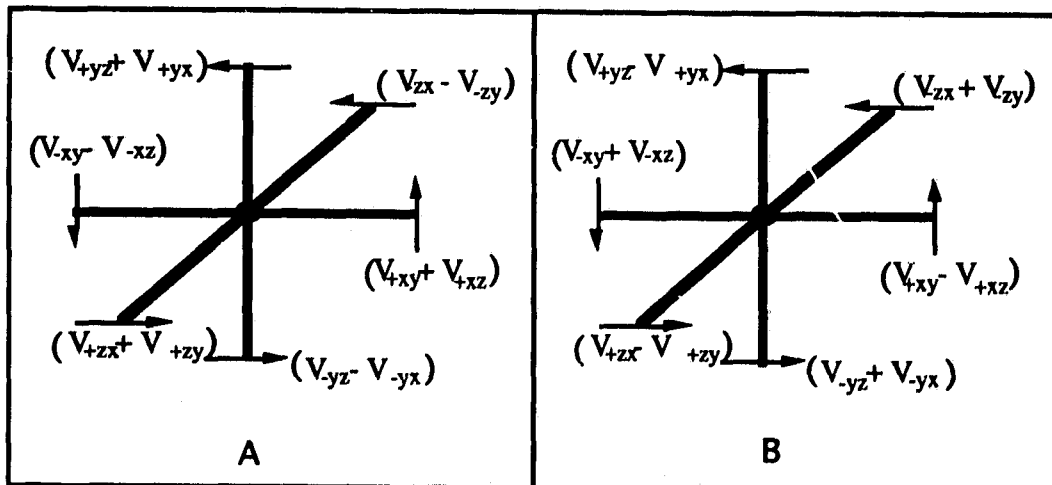
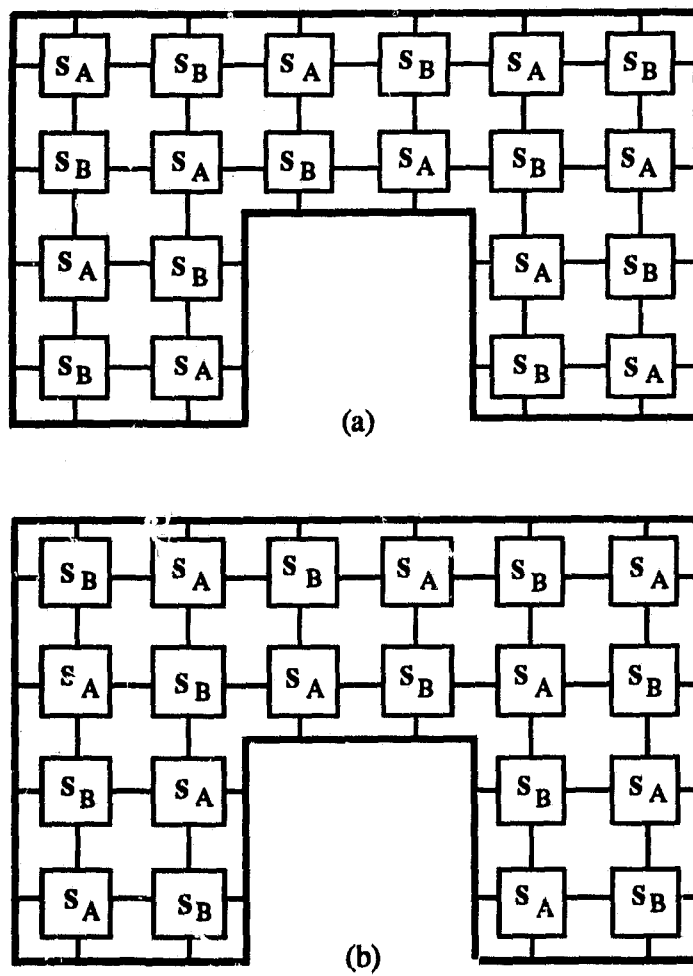
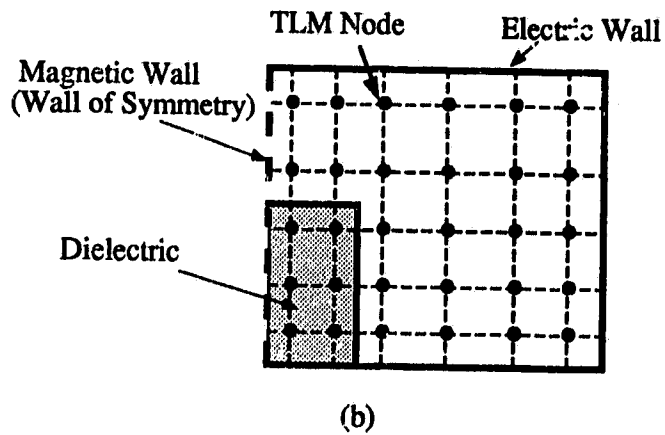
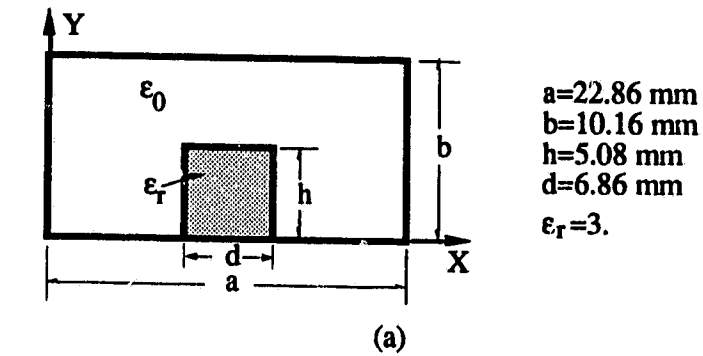


Fig. 3.5 Pair of 6-port condensed FDTLM nodes



*Fig.3.6 The equivalent FDTLM networks of ridged waveguide*



*Fig.3.7 (a) Cross section and dimensions of a rectangular waveguide partially filled with a dielectric slab. (b) Layout of the TLM graded mesh.*

## Chapter 4

### APPLICATIONS OF THE FDTLM METHOD

The great flexibility and versatility of the FDTLM method resides in the fact that the FDTLM node is a scattering node incorporating the properties of electromagnetic fields and their interaction with the boundaries and surrounding media. This local feature makes the FDTLM scattering node essentially an algebraic object: a novel propagator of discretized Maxwell's equations. Hence, the electromagnetic problem need not be reformulated for every new structure. A general purpose program has been developed. This program has great flexibility since only the parameters of the geometry of the structure need to be entered for computation. In the following some 2D and 3D problems will be investigated by using the FDTLM algorithm.

#### 4.1 Analysis of Propagation Characteristics of Arbitrary Waveguide Structures

For the analysis of a 2D eigenvalue problem, an arbitrary waveguide structure is discretized to form a periodic network. The study of electromagnetic wave propagation in this periodic network is performed using Floquet's theorem, which reduces the theoretically infinite number of network cells to a single unit cell (a slice of waveguide in propagation direction) as shown in Fig.3.2. The resulting matrix eigenvalue equation (3.13) is solved numerically using the well-known matrix eigensystem routines such as the *QR*-procedure, *i.e.* decomposing the eigen-matrix into a product of a unitary matrix  $Q$  and the upper right triangular matrix  $R$ , the eigenvalues and corresponding eigenvectors are then found by an iterative process.

In order to test the program, two typical structures are computed for dispersion characteristics. Firstly, the rectangular waveguide filled with a lossy dielectric is chosen to illustrate results for the phase constant  $\beta$  and the attenuation constant  $\alpha$  as a function of frequency. As shown in Fig.4.1, the numerical results are identical with the exact solution choosing only 5 nodes in  $x$ -axis direction.

Secondly, to demonstrate the versatility of this method, the frequency dependent even- and odd-mode phase constants are calculated for the coupled microstrip lines on anisotropic substrate. Fig.4.2(a) shows the dispersion characteristics, as obtained with the FDTLM method. Results calculated with the time-domain TLM method [23] are also shown in the same figure. In the time-domain method, the mesh sizes are :  $a=17 \Delta l$ ,  $h=3 \Delta l$ ,  $b=6 \Delta l$ ,  $s=3 \Delta l$ ,  $w=3 \Delta l$ , and  $\Delta l=0.5\text{mm}$ , while in the FDTLM method, the total number of nodes is only  $10 \times 6$  in the cross-section. This clearly illustrates the accuracy of the FDTLM algorithm in situations where non-TEM modes propagate. Furthermore, the FDTLM algorithm is quite robust with respect to the mesh size. The ratio of mesh sizes of adjacent nodes may change in a wide range without causing any numerical problem. For example, Fig.4.2(b) shows a microstrip on alumina substrate with finite metallization thickness  $t=0.012\text{mm}$ . Both dielectric and ohmic losses are considered with  $\epsilon_r=9.35$ ,  $s_d=2.36 \times 10^{-5} \text{ s/mm}$ , and  $s_c=1.7 \times 10^4 \text{ s/mm}$ ,  $w=1.245 \text{ mm}$ ,  $h=0.508 \text{ mm}$ . It is noted that the dominant mode has an even symmetry of the tangential electric field at  $x=0$ . The number of the nodes in  $x$ -direction is 8, with a graded mesh size ranging from (from the centre to the right wall) 0.2mm, 0.16mm, 0.1313mm, 0.1312mm, 0.15mm, 0.3mm, 1.0mm, 5.0mm, respectively. The number of nodes in  $y$ -direction is 9, with the mesh size (from bottom to top) 0.2mm, 0.2mm, 0.054mm, 0.054mm, 0.012mm, 0.054mm, 0.1mm, 0.4mm, 2.5mm, respectively. Table 4.1 illustrates that the numerical results of the FDTLM algorithm for the effective dielectric constant  $\epsilon_{\text{eff}}$  and the attenuation constant  $\alpha$  compare well with the SDA [39] and experimental data[36].

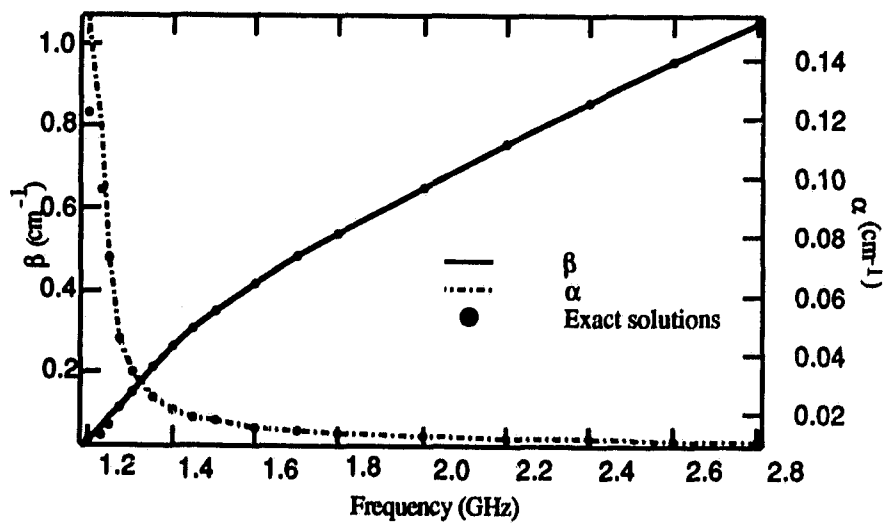
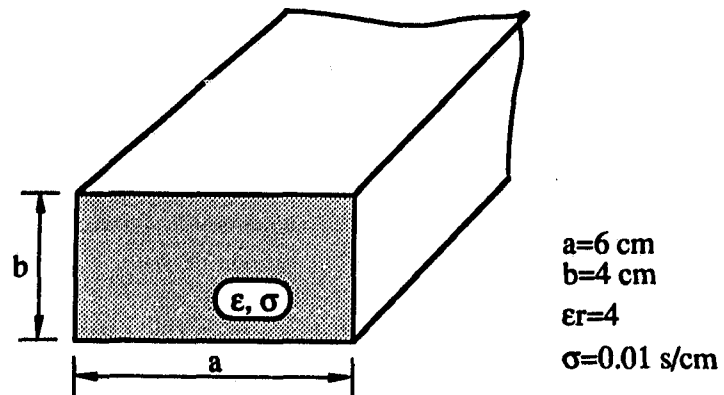


Fig. 4.1 Propagation constant versus frequency for a rectangular waveguide filled with a lossy dielectric

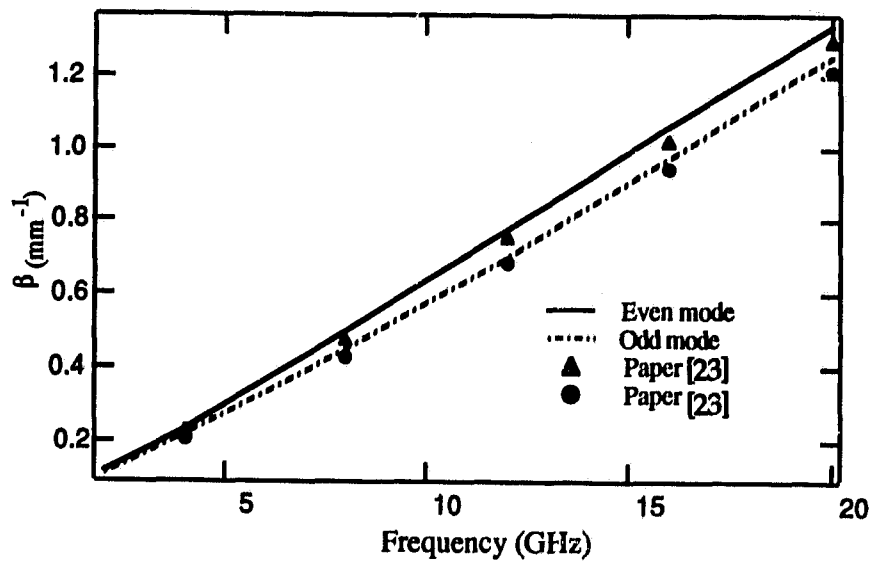
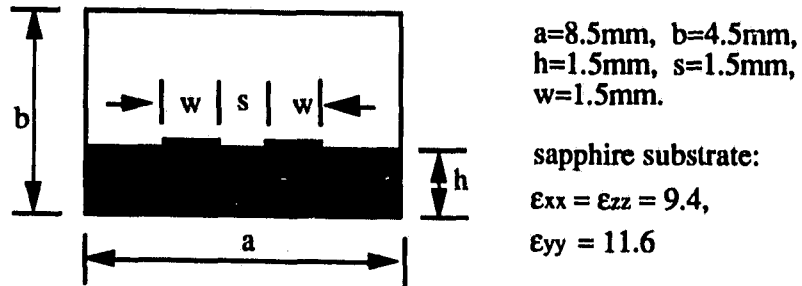


Fig. 4.2(a) Dispersion diagram for even and odd fundamental modes of coupled microstrip line

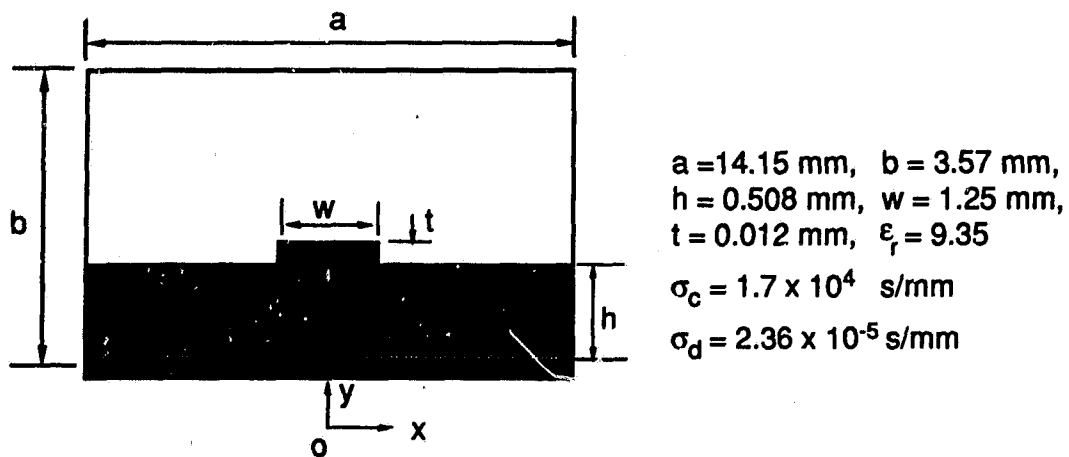


Fig. 4.2(b) Microstrip with finite metallization thickness

Table 4.1

*Dispersion and loss characteristics of a microstrip with finite metallization thickness*

F (GHz)	Results of the FDTLM		Results of the SDA		Measured data
	$\epsilon_{\text{eff}}$	$\alpha$ (dB/cm)	$\epsilon_{\text{eff}}$	$\alpha$ (dB/cm)	$\alpha$ (dB/cm)
1.0	6.781	0.0125	6.752	0.0131	0.0135
2.0	6.904	0.0175	6.809	0.0182	0.0190
3.0	6.904	0.0234	6.872	0.0241	0.0251
4.0	6.993	0.0270	6.932	0.0282	0.0298
5.0	7.053	0.0342	6.987	0.0355	0.0367

## **4.2 The FDTLM Simulation of Periodic Structures in Microwave and Integrated Optical Circuits**

Periodic structures have received considerable attention in microwave and integrated optical circuits. For example, corrugated waveguides are used as feed horns, waveguide filters, mode converters, slow-wave matching networks. Planar periodic structures have also been applied to realize velocity-matching between the modes of the microwave electrode and the optical guide in the interaction region of traveling wave integrated electro-optic modulators. However, a lack of reliable and accurate algorithms to analyze modal fields and propagation properties has restricted the development of rigorous and efficient design methods for these components. The mode-matching technique[25], for example, leads to complex analytical procedures and slow convergence behaviour.

In contrast to the above method, the frequency-domain TLM method is ideally suited for the simulation of periodic structures for several reasons: First, the TLM method discretizes the space into an equivalent periodic transmission line network. This feature is particularly appropriate to analyze arbitrarily shaped periodic waveguide structures. Second, the FDTLM node can be constructed independently of its environment and characterized by a scattering matrix. As a result, the diakoptics technique can be easily combined into the FDTLM algorithm, which alleviates significantly the large memory requirements known from other space discretization methods. Third, extensive calculations [21,24] have shown that the FDTLM algorithm is quite robust with respect to the mesh size. The ratio of the mesh sizes of adjacent nodes may change in a wide range (for example from 0.1 to 100). Such a large ratio is often required in cases where the structure has widely varying dimensions such as the coplanar slow-wave electrode structure (Fig.4.5). Such structures can not be easily analyzed with time-domain methods (TDTLM or FDTD). This is so, because if node sizes vary greatly, a small time step may be required to satisfy the stability criterion. Fourth, as a consequence of Floquet's theorem, only one unit cell (one period of the structure) must be analyzed. The problem of determining the dispersion characteristics on periodic structures reduces to the solution of an eigenvalue

equation for one unit cell. At the same time, the transverse field distribution is also determined by the eigenvectors of the eigenvalue equation.

In the following, the analysis method will be demonstrated for arbitrary microwave or optical waveguide structures. The study of electromagnetic wave propagation in periodic structures is performed using Floquet's theorem, which reduces the considerations to a single unit cell as shown in Fig.4.3(a) for the vane-type periodic structure. The unit cell of the periodic structure is defined between reference planes AA' and BB'.  $d$  denotes the size of structural periodicity in the propagation direction.

The first step is to evaluate the intrinsic scattering matrix of the unit cell. The process is somewhat similar to section 3.2. The difference to the normal uniform waveguide is that each unit cell is of different cross-section. Therefore, the unit cell is first cut into slices along the propagation direction and the intrinsic scattering matrix for each slice is calculated. Then the overall intrinsic scattering matrix of the unit cell is calculated by progressively cascading these slices. For example, in cascading two slices (scattering matrices  $S^I$  and  $S^{II}$ ), the elements of the combined matrix  $S$  becomes

$$\begin{aligned} S_{11} &= S_{12}^I \cdot [I - S_{11}^{II} \cdot S_{22}^I]^{-1} \cdot S_{11}^{II} \cdot S_{21}^I + S_{11}^I \\ S_{12} &= S_{12}^I \cdot [I - S_{11}^{II} \cdot S_{22}^I]^{-1} \cdot S_{12}^{II} \\ S_{21} &= S_{21}^{II} \cdot [I - S_{22}^I \cdot S_{11}^{II}]^{-1} \cdot S_{21}^I \\ S_{22} &= S_{21}^{II} \cdot [I - S_{22}^I \cdot S_{11}^{II}]^{-1} \cdot S_{22}^I \cdot S_{12}^{II} + S_{22}^{II} \end{aligned} \quad (4.1)$$

where  $I$  is a unit matrix. Thus, beginning with the reference plane AA', we continue this procedure repeatedly through the unit cell until finally arriving at the reference plane BB'. If it is assumed that the overall intrinsic scattering matrix between the reference planes AA' and BB' is

$$\begin{bmatrix} V_A^r \\ V_B^r \end{bmatrix} = \begin{bmatrix} S_{AA} & S_{AB} \\ S_{AB} & S_{AA} \end{bmatrix} \begin{bmatrix} V_A^i \\ V_B^i \end{bmatrix} \quad (4.2)$$

then, to determine the propagation constants, a transfer matrix must be determined from the scattering matrix, *i.e.*

$$\begin{bmatrix} V_A \\ I_A \end{bmatrix} = \begin{bmatrix} SR^{-1} & SR^{-1}S - R \\ R^{-1} & R^{-1}S \end{bmatrix} \begin{bmatrix} V_B \\ I_B \end{bmatrix} \quad (4.3)$$

where

$$S = [(1 - S_{AA}) - S_{AB}(1 - S_{AA})^{-1}S_{AB}]^{-1}(1 + S_{AA}) - [(1 - S_{AA})S_{AB}^{-1}(1 - S_{AA}) - S_{AB}]^{-1}S_{AB}$$

$$R = [(1 - S_{AA}) - S_{AB}(1 - S_{AA})^{-1}S_{AB}]^{-1}S_{AB} - [(1 - S_{AA})S_{AB}^{-1}(1 - S_{AA}) - S_{AB}]^{-1}(1 + S_{AA})$$

Let the propagation constant in z-direction be  $\gamma$ , then the periodic boundary conditions based on Floquet's theorem are

$$\begin{bmatrix} V_B \\ I_B \end{bmatrix} = e^{\gamma d} \cdot \begin{bmatrix} V_A \\ I_A \end{bmatrix} \quad (4.4)$$

Combining equations (4.3) and (4.4), and considering the analytical properties of the transfer matrix, we have

$$(SR^{-1}) \cdot V_A = \cosh(\gamma d) \cdot V_A \quad (4.5)$$

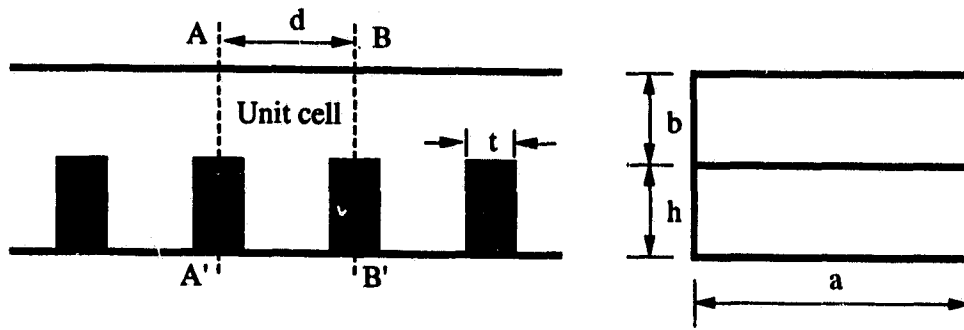
Equation (4.5) is the standard form of an eigenvalue problem to be solved for the propagation constants of the periodic waveguide modes. The eigenvectors correspond to the transverse field distributions. In general, only a few of the propagation constants  $\gamma$  are imaginary, and these are associated with propagating modes. The modes with real propagation constants are evanescent modes and are analogous to the evanescent modes which occur in a normal uniform guide at a discontinuity.

To confirm the validity and effectiveness of the proposed analysis method, a periodic vane-type slow-wave structure (Fig.4.3a) is analyzed. The dispersion diagram shown in Fig.4.3(b) illustrates good agreement with the mode-matching technique [25]. It should be noted that all propagation modes could conveniently be separated because of the characteristics of the eigenvalue equation.

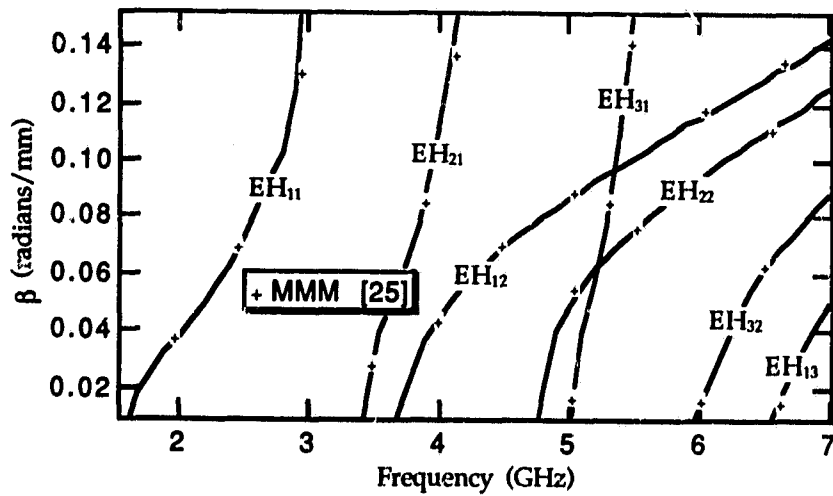
As a rather general case, a corrugated waveguide with plain corrugations is shown in Fig.4.4(a). Fig.4.4(b) shows numerical results for propagation phase constant characteristics against frequency. Results in [26] and measured data [26] are shown in the same figure. It is evident that the results of the FDTLM simulation are in better agreement with measured data than the mode-matching

results. The CPU-time of the FDTLM algorithm is 0.24 second for each frequency point. Fig.4.4(c) shows isometric representations of the normalised transverse electrical field distribution of the cross-section in the small waveguide ( $a \times b$ ). One quarter of the structure is used by considering the symmetry with a mesh layout of  $13 \times 13$ . The discretizing transverse field distribution, which is located at the beginning ( $z=0$  in Fig. 4.4a) of the periodic structure, is obtained by the eigenvector of the matrix  $SR^{-1}$ . It is noted that  $y$ -variation of the field is hyperbolic, but  $x$ -variation is trigonometric for the first slow mode ( $\beta/k_0 > 1$ ) at frequency 7.5 GHz. For the second fast mode ( $\beta/k_0 < 1$ ) at 10 GHz, the variations in both  $x$ - and  $y$ -directions are trigonometric, which correspond those of the normal rectangular waveguide with the same transverse dimensions.

The FDTLM analysis has been extended to the geometry of coplanar slow-wave electrode structures on GaAs substrate suitable for integrated traveling-wave electro-optic modulators [27]. The structure under consideration is schematically illustrated in Fig.4.5(a). It is a conventional coplanar waveguide with slots cut periodically into both ground plane electrodes. These slots periodically change the inductance and capacitance per unit length of the line. The phase velocity  $v_{ph}$  is reduced because the inductance and capacitance per unit length has been increased. The  $v_{ph}$  results for a slotted line and a smooth coplanar line are shown in Fig.4.5(b). The measured data are mapped into the same figure to allow a good comparison. As shown the slots have reduced the  $v_{ph}$  from 11.5 cm/ns to 8.9 cm/ns, which is the  $v_{ph}$  of an AlGaAs/GaAs ridge optical guide operating at 1.3  $\mu\text{m}$  free space wavelength.



(a)



(b)

Fig.4.3 (a) A vane-type periodic structure. (b) Dispersion diagram  
 ( $a=90.0, h = 24.6, b = 20.0, d = 14.175, t = 3.175, a = 90.0$  mm).

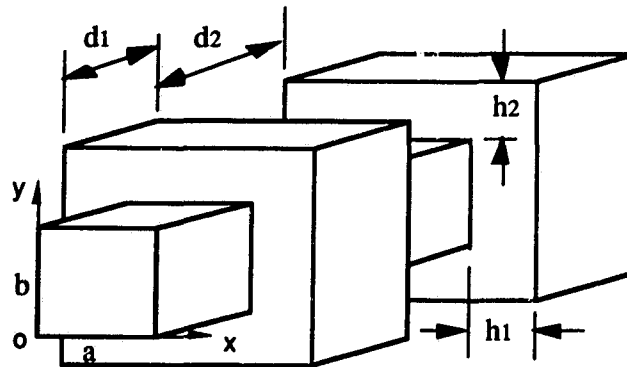


Fig. 4.4a Rectangular corrugated waveguide ( $a=b=25.0$ ,  
 $h_1=h_2=8.2$ ,  $d_1=3.0$ ,  $d_2=1.0$  (mm))

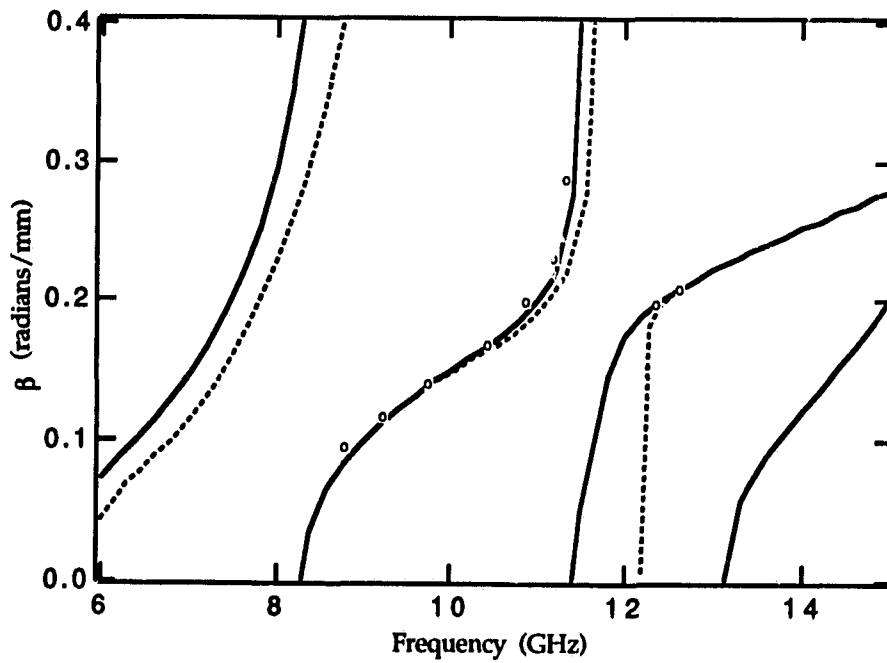
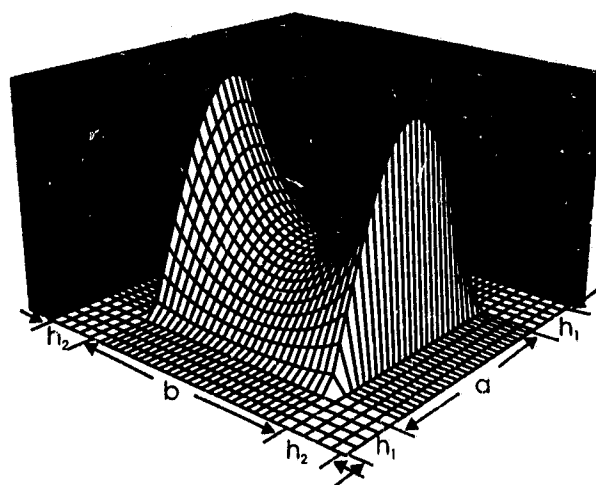
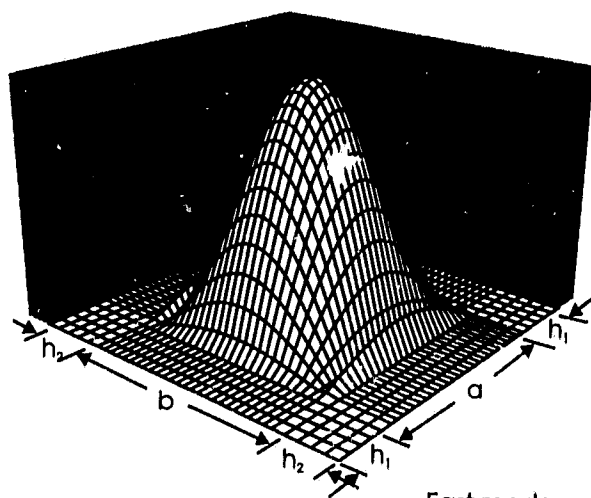


Fig. 4.4b Dispersion diagram (— this method; ---- mode-matching method; oooo measured data[26])

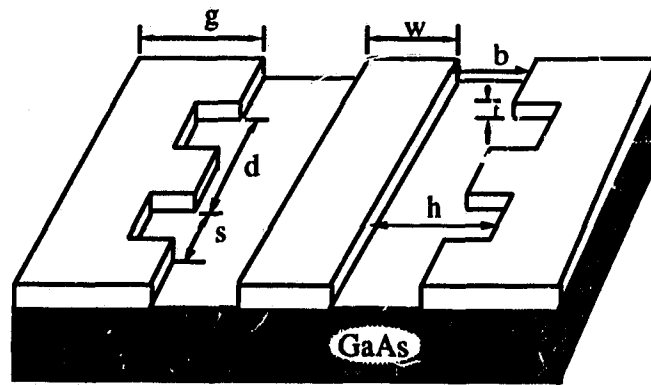


Slow mode

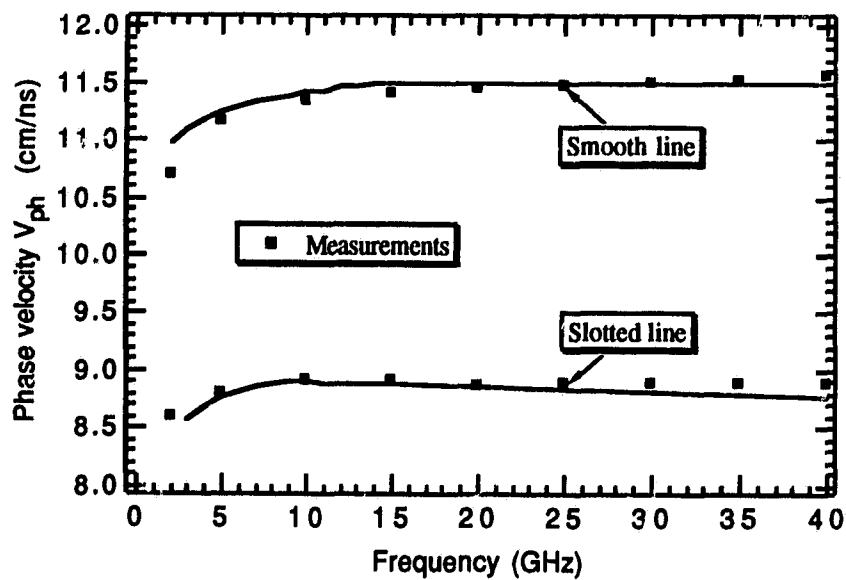


Fast mode

*Fig. 4.4c Isometric configurations of normalised transverse electrical fields of both the first slow mode and the second fast mode.*



(a)



(b)

Fig. 4.5 (a) Schematic diagram of coplanar slow-wave structure. (b) Effect of slots on phase velocity ( Slotted line has dimensions  $b=9 \mu\text{m}$ ,  $d=50 \mu\text{m}$ ,  $g=200 \mu\text{m}$ ,  $h=80 \mu\text{m}$ , and  $w=28 \mu\text{m}$ ; the smooth line has no slots with gap  $b=h=9 \mu\text{m}$ . ). • Measurements[27]

### 4.3 S-Parameter Calculation of Arbitrary Waveguide Discontinuities

The scattering parameters of 3D discontinuities are related to the modal fields at both sides of a discontinuity. Since the field components for the different modes can be separated in the FDTLM method, the reference plane for the s-parameter calculation may be located right in the discontinuity interface. No additional line length is required to ensure fundamental mode propagation left and right from a discontinuity. This is an important advantage of this new method. Furthermore, since each node scattering matrix is an independent algebraic block, the diakoptics technique can be readily applied to subdivide a large structure into smaller sub-structures, which are characterized independently and then cascaded with the other sub-structures. This alleviates the large memory requirements known from other space discretization methods significantly.

As a first example for S-parameter calculations, Fig.4.6 presents the investigation of the transition between a rectangular waveguide and a dielectric slab loaded waveguide of finite length. The input reflection coefficient calculated by the presented method is compared with measurements [28] performed in the x-band. Both results are in excellent agreement. The typical computation time on an IBM RISC 6000(530) is less than one second per frequency sample point.

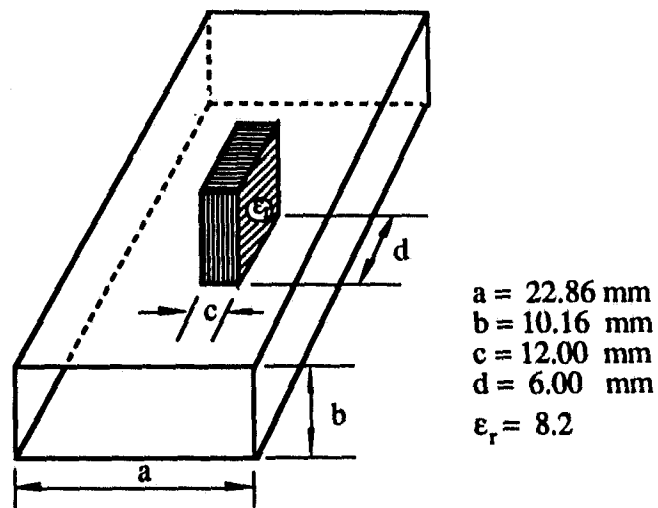
The computation for an E-plane filter is shown in Fig.4.7. The whole structure is divided into three regions: two attached rectangular waveguides which serve as the input and output ports, and the discontinuity section which consists of four-section homogeneous waveguide and four-section inserted metal septums. The discontinuity section is first cut into slices along the propagation direction and the intrinsic scattering matrix for each slice is calculated. The length of each slice is around a tenth of the waveguide wavelength. Then the overall intrinsic scattering matrix for the discontinuity section is calculated by cascading these slices. The CPU-time in this case is about 0.43 second per frequency point. Fig.4.7(b) shows the good agreement between the FDTLM method, the mode-matching method and experiment [29].

The scattering parameters of hybrid modes at discontinuities is important for accurate circuit design. As an application of the FDTLM method for the computation of scattering parameters of hybrid modes, we choose a typical example of a microstrip step discontinuity(Fig.4.8). The strip thickness is assumed to be zero. The results are quite flat over a large frequency range and again in good agreement with the results from the mode-matching technique[30].

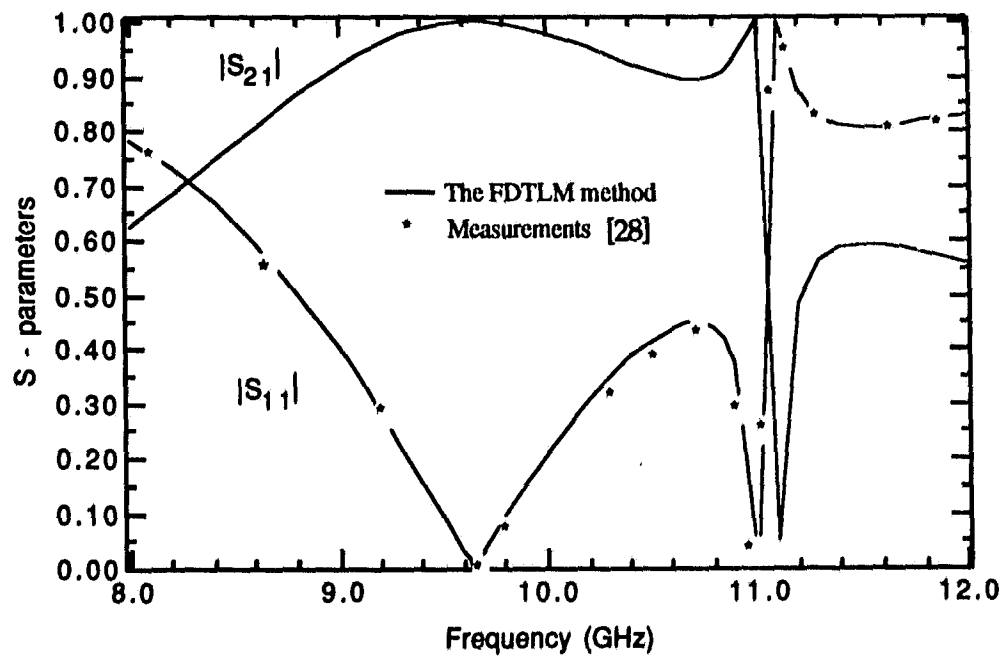
A more complicated 3D electromagnetic field analysis of interconnections in a multichip module structure is presented. Fig.4.9(a) shows a 3D view of the multichip modul. The pads of the GaAs chip die bonded to the alumina ceramic substrate are interconnected with substrate electrode pads by tape automated bonding (TAB). Fig.4.9(b) shows a simulation model of the chip interconnection using a TAB technique. The chip interconnection is assumed to be terminated by 50- $\Omega$  transmission lines at both the input and output terminals. The model can be considered as a set of planar transmission line structures containing abrupt changes in the dielectric constant, height, and width, as well as cascaded discontinuities on different heights of substrate.

The transmission character of TAB leads is simulated for several mounting conditions. Fig.4.10 illustrates the frequency-dependent s-parameters for a transition from a microstrip motherboard to a GaAs chip module, here simplified as a transition from an alumina substrate carrier to a microstrip line on GaAs substrate. The reflection from such an interconnect increases significantly with frequency. This is so, because the interconnect assembly may be modeled as a low-pass  $\pi$ -network that consists of two shunt capacitors (microstrip steps between both ends of the TAB) and a series inductor (TAB leads). It is noted that the signal transmission range can be increased by shortening the TAB leads.

Fig.4.11 illustrates the effect of the lateral substrate dimensions of the chip on the s-parameters of the interconnect. Due to the small substrate width of the chip, one could also regard this junction as a transition from a microstrip to a microstrip rib structure. The s-parameters are calculated with two different rib widths. Both results deviate only slightly towards higher frequencies.

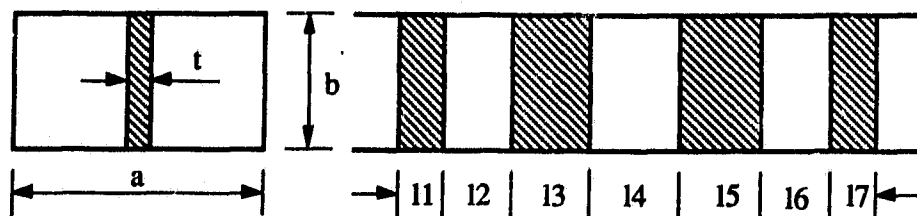


(a)



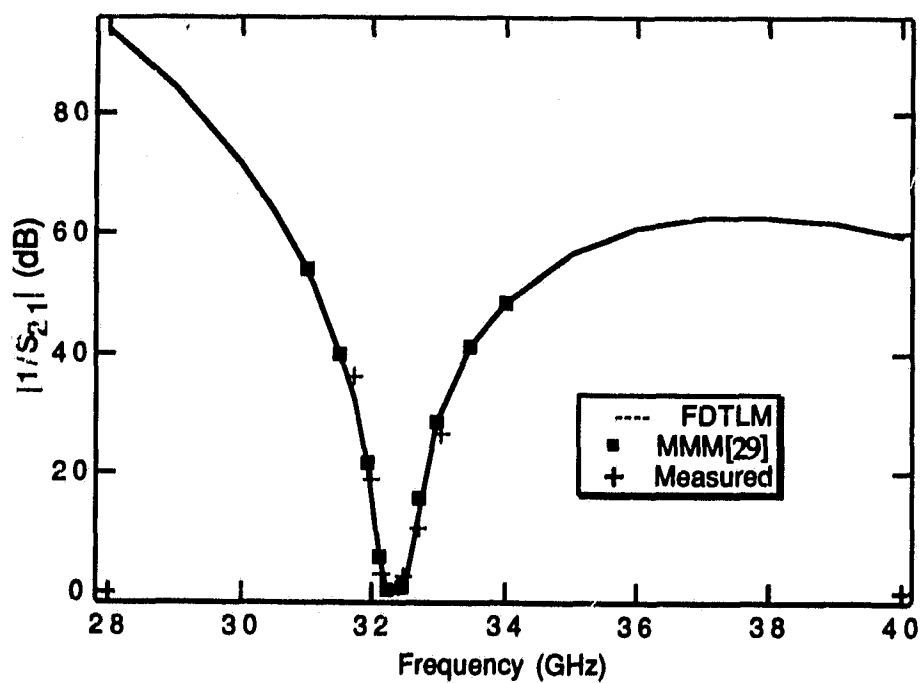
(b)

**Fig. 4.6 (a) Dielectric slab loaded waveguide of finite length. (b) S-parameters of the transition rectangular waveguide to dielectric slab loaded waveguide.**



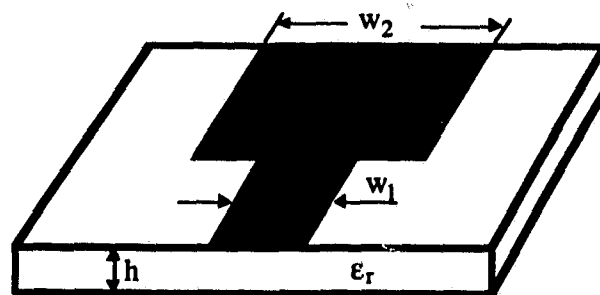
( $a=7.112$ ,  $b=3.556$ ,  $t=0.51$ ,  $l_1=l_7=1.009$ ,  $l_2=l_6=4.778$ ,  $l_3=l_5=3.87$ ,  $l_4=4.796$  mm)

(a)



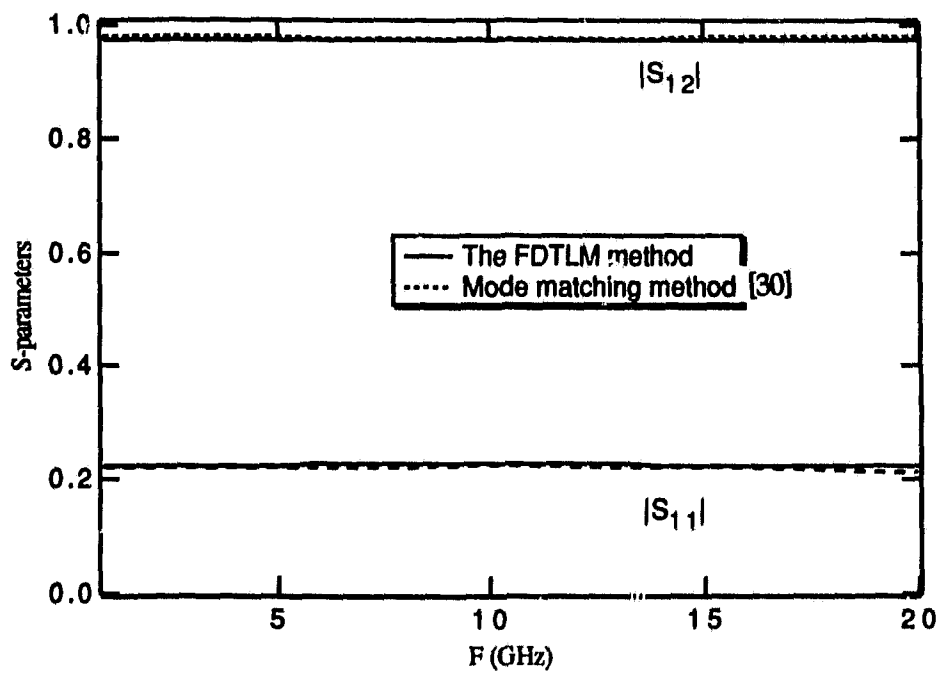
(b)

**Fig. 4.7** Calculated and measured insertion-loss as a function of frequency of a Ka-band 3 resonator E-plane filter.



$$w_1=0.6, w_2=2w_1, h=0.6 \text{ (mm)}, \epsilon_r=10$$

(a)



(b)

Fig. 4.8 Frequency-dependent S-parameters of the microstrip step-in-width

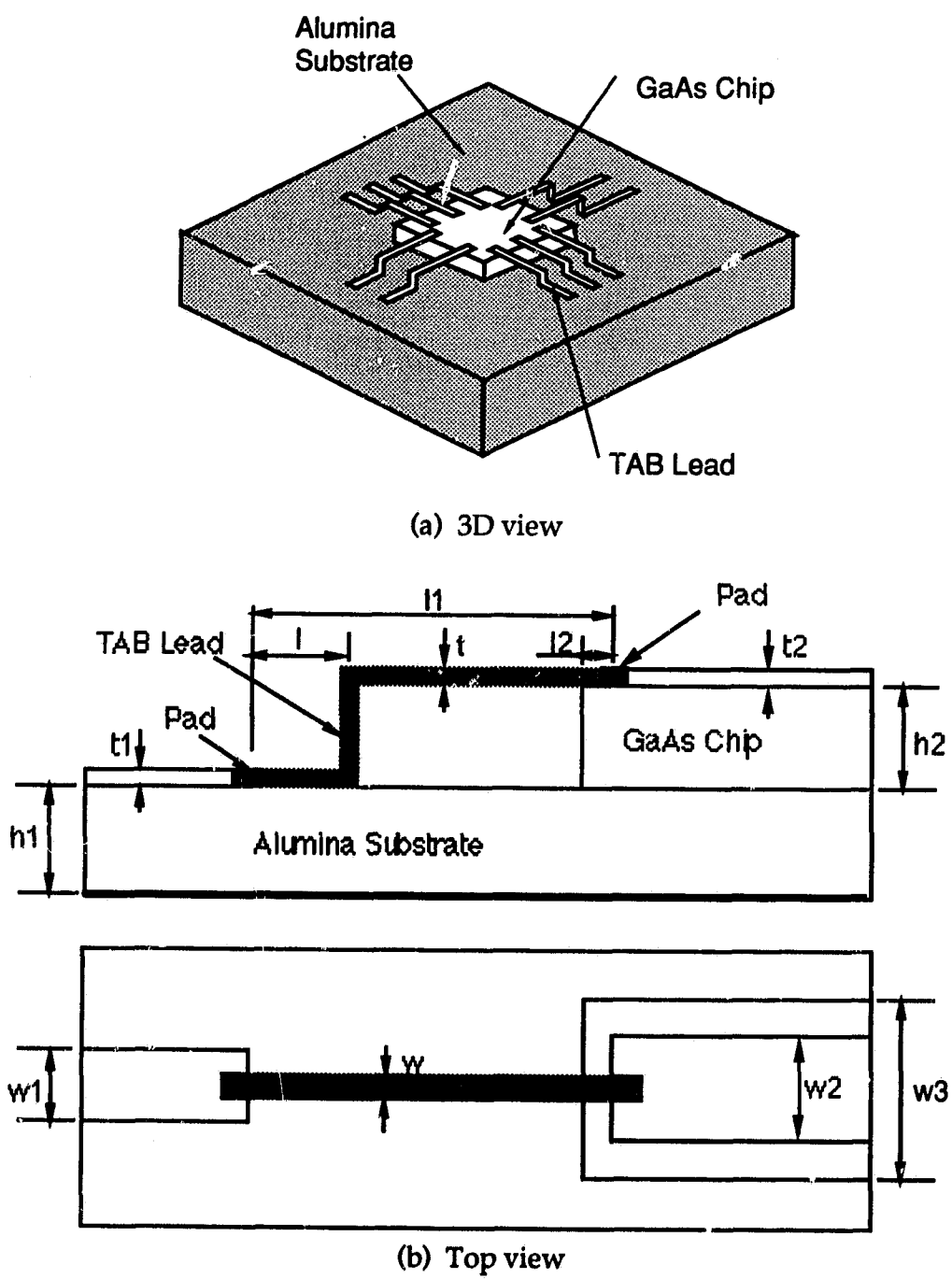


*Fig. 4.9 A multichip module structure and simulation model of the chip interconnection using TAB technique*

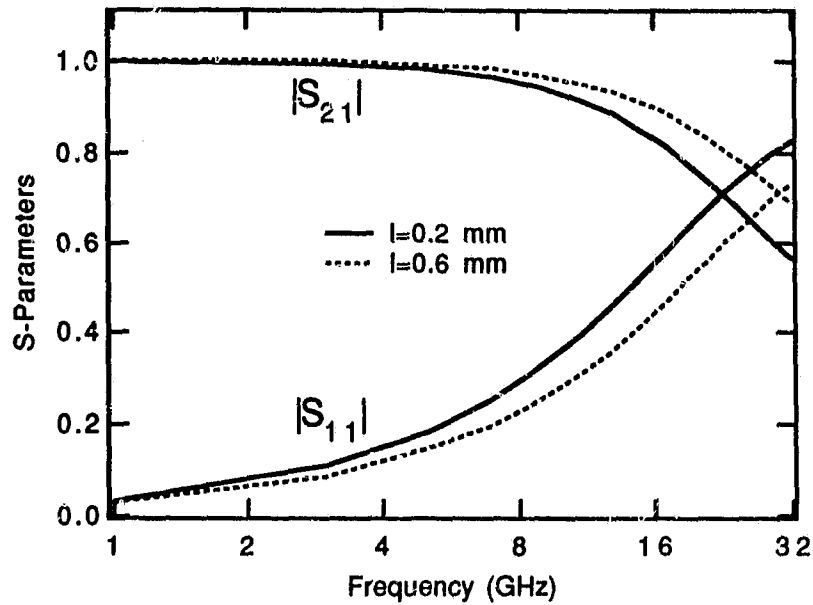


Fig.4.10 Frequency-dependent S-parameters of the interconnect shown in Fig.4.9 with different distance between pads ( $h_1=0.2\text{mm}$ ,  $h_2=0.4\text{mm}$ ,  $w=0.1\text{mm}$ ,  $w_1=0.2\text{mm}$ ,  $w_2=0.5\text{mm}$ ,  $w_3=1.0\text{mm}$ ,  $l_1=1.6\text{mm}$ ,  $l_2=0.2\text{mm}$ ,  $t_1=t_2=t=0$ ,  $\epsilon_{r1}=9.8$ ,  $\epsilon_{r2}=12.9$ ).

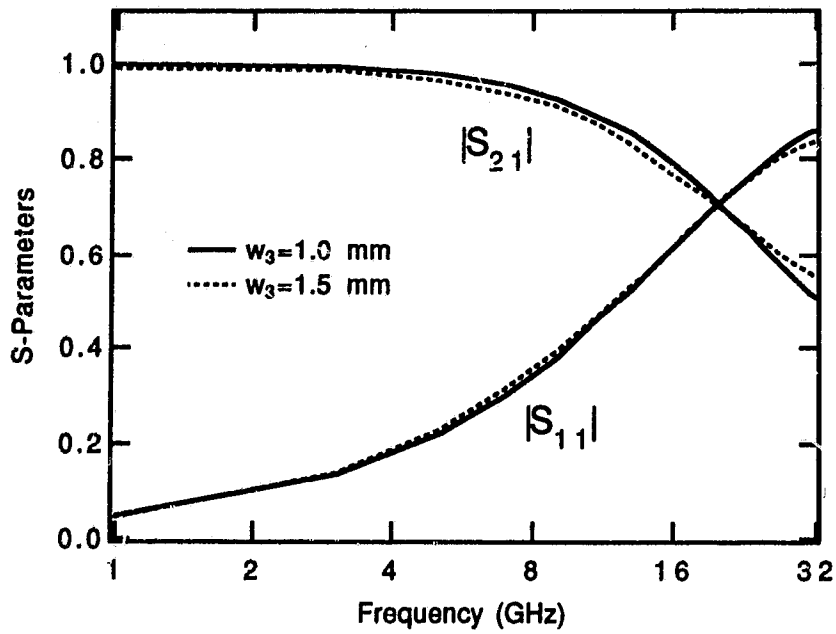


Fig.4.11 Frequency-dependent S-parameters of the interconnect shown in Fig.4.9 with different rib widths. ( $h_1=0.2\text{mm}$ ,  $h_2=0.4\text{mm}$ ,  $w=0.1\text{mm}$ ,  $w_1=0.2\text{mm}$ ,  $w_2=0.5\text{mm}$ ,  $l=0.2\text{mm}$ ,  $l_1=1.6\text{mm}$ ,  $l_2=0.2\text{mm}$ ,  $t_1=t_2=t=0$ ,  $\epsilon_{r1}=9.8$ ,  $\epsilon_{r2}=12.9$ )

#### **4.4 Frequency-Domain TLM Analysis of the Transition from Rectangular to Circular Waveguide**

Short, compact and wideband transitions between rectangular and circular waveguides are often required in filters, multiplexers and orthomode transducers. Although smooth transitions, gradually opening up to the circular waveguide dimensions are commercially available and provide excellent wideband performance, they also require more space than sometimes acceptable. Between the smooth transition on one hand and the abrupt single-step transition on the other hand there are two possible solutions to obtain the shortest transition for the bandwidth required: The stepped transformer in which circular waveguide sections of approximately  $\lambda/4$  lengths and increasing radii are cascaded (Fig.4.12c) and the ridged waveguide transformer (Fig.4.12b) which is known from rectangular waveguides. In particular the latter transition is of interest since the two waveguides can easily be fabricated as split-block housings and the stepped metal septum can be sandwiched between both halves. If the septum thickness is below  $200\mu\text{m}$  thickness, the transformer dimensions can be photo etched accurately and, if fine tuning is required, only the septum needs to be redone and not the waveguide housing, which is in most cases the more expensive part. A further advantage of the ridged waveguide transition is the fact that the polarization of the circular waveguide mode is clearly determined by the orientation of the ridges.

In the following the FDTLM algorithm is used to analyze rigorously such composite transitions: an abrupt transition, a tapered transition consisting of cascaded sections of circular waveguide with increasing (decreasing) radii, and a ridged waveguide transition.

Although the circular ridged waveguide as well as related discontinuities within the circular coordinate system can be analyzed using the FDTLM algorithm and a cylindrical mesh (details will be given in chapter V), the interconnection between nodes in the rectangular mesh and nodes in the cylindrical mesh is impossible so far. Hence, both structures are discretized with a rectangular mesh which requires that the waveguide walls of the circular guide are approximated by a rectangular step function. To get a feeling for the size of the mesh configuration necessary to obtain good accuracy, a comparison between

numerical and analytical results is shown in Fig.4.13. Due to the symmetry of the structure only one-fourth needs to be considered. The results for the propagation constant of the  $TE_{11}$  mode shows excellent agreement for 8x8 nodes over the cross-section.

Another comparison is shown in Fig.4.14. Since the slot coupled transition (Fig.4.12a) between a rectangular and a circular waveguide has been investigated numerically and experimentally by a number of researchers (i.e. [31,32]), we have chosen this transition to compare the FDTLM simulation results. As illustrated in Fig.4.14 the agreement between measurements, the moment method solution [31] and the FDTLM results is very good.

Fig.4.15 shows the calculated  $|S_{11}|$  in dB as a function of frequency for three- and five-step ridged transitions. The transformer dimensions are given in Table 4.2. As expected, in comparison to an abrupt transition, the return loss is reduced significantly and can even be further improved by increasing the number of steps. On the other hand, the results are not quite as good as expected. The reason for this is the fact that this type of transformer is very sensitive to variations of section lengths and heights. The results shown in Fig.4.15 and the corresponding dimensions have been found. It is expected that the use of an efficient optimization routine will improve the performance significantly.

Fig.4.16 shows a transformer with steps in the radius of the circular waveguide sections. Obviously, the results are better than for the ridged waveguide transformer. On the other hand, this transformer allows a smoother transition between the  $TE_{10}$  mode of the rectangular waveguide and the  $TE_{11}$  mode of the circular waveguide as illustrated in Fig. 4.12(c). The disadvantage, however, is that in this case the transformer sections must be milled individually.

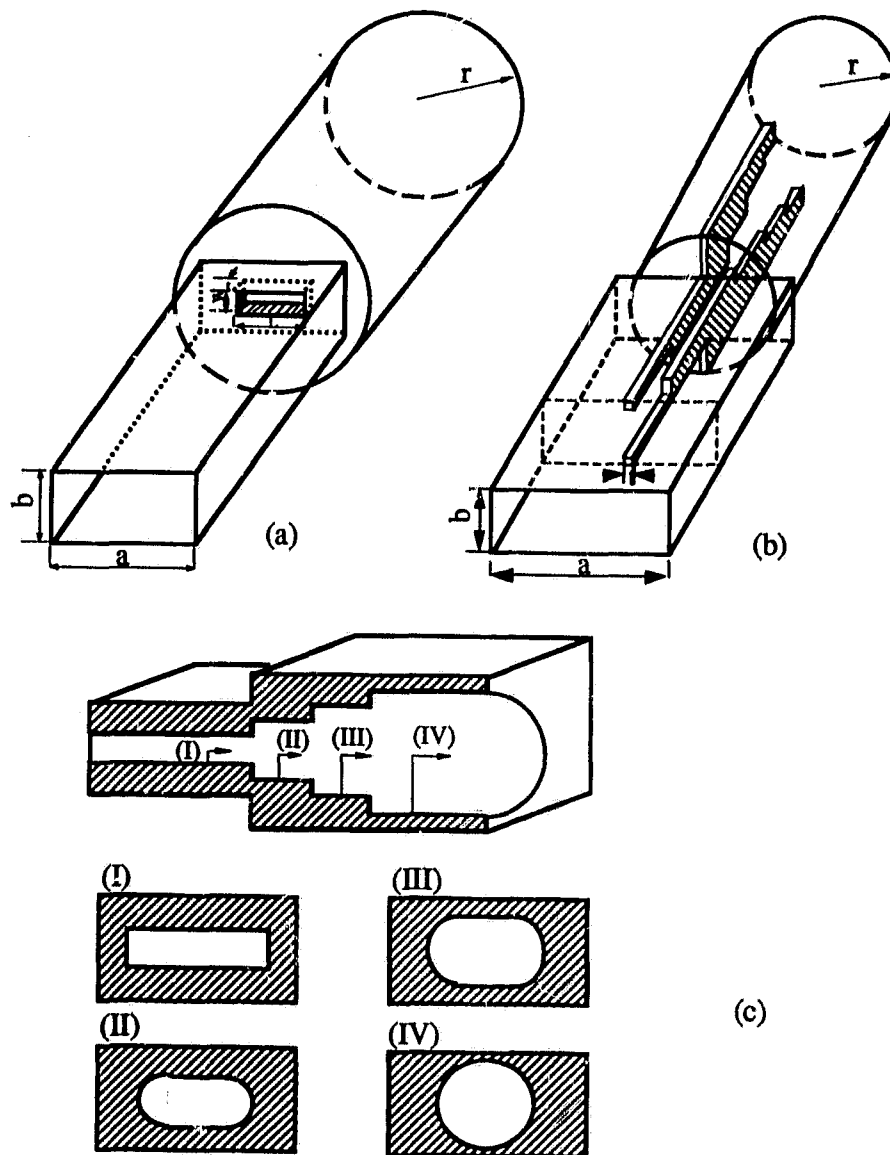


**Fig.4.12** Three types of transitions from rectangular to circular waveguides.  
 (a) Slot coupled transition. (b) Ridged waveguide step transformer structure. (c) Direct stepped transformer structure.



F (GHz)	$\epsilon_{\text{eff}} (\text{TE}_{11}^{\circ})$		
	Exact	Cylindrical Mesh	Rectangular Mesh
30.0	0.1475	0.1480	0.1482
32.0	0.2507	0.2511	0.2513
34.0	0.3363	0.3368	0.3370
36.0	0.4080	0.4087	0.4090

*Fig.4.13 Geometry and the effective dielectric constant of an empty C330 circular waveguide using a stepped approximation.*

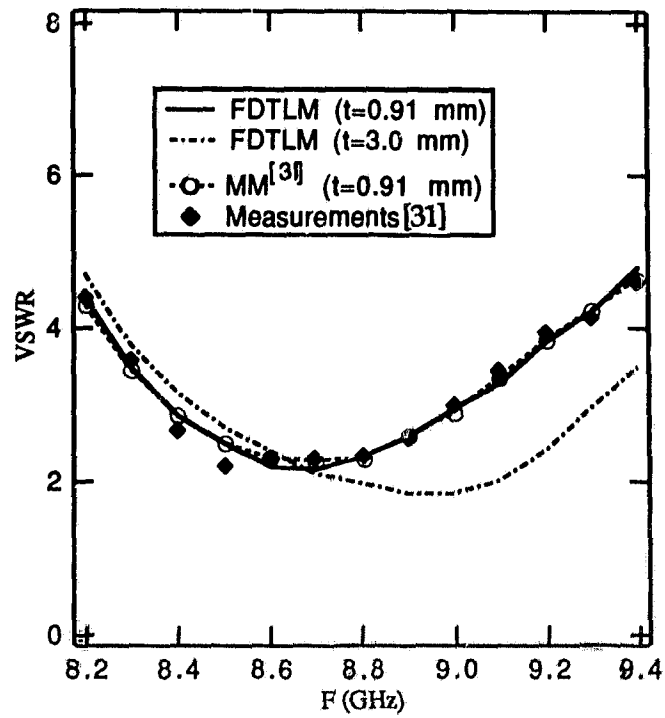
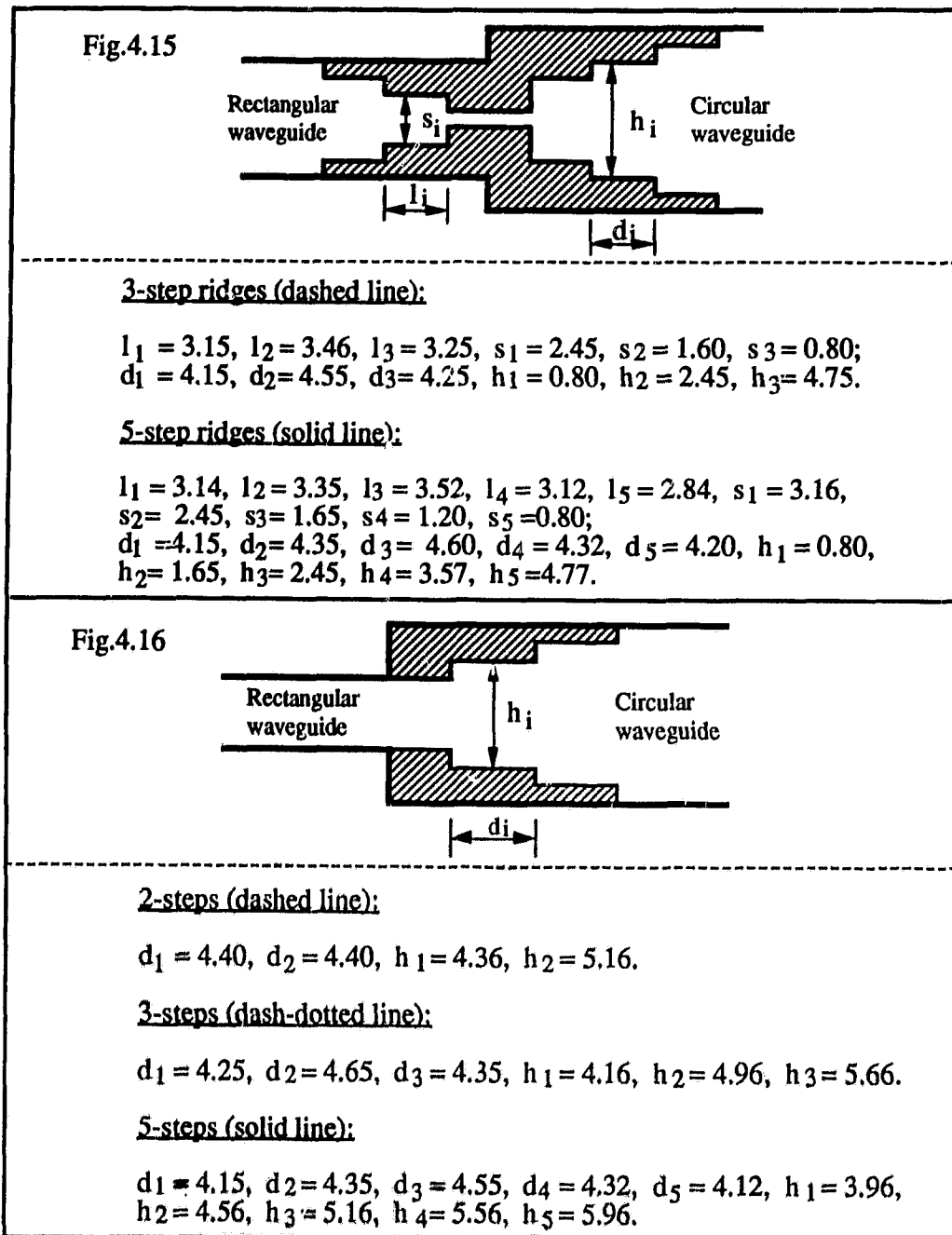


Fig.4.14 Variation of VSWR with frequency for Fig.4.12(a) structure  
(  $L=17.00\text{mm}$ ,  $W=1.07\text{ mm}$ ,  $a=22.86\text{ mm}$ ,  $b=10.16\text{ mm}$ ,  
and  $r=11.85\text{ mm}$  ).

Table 4.2

The dimensions of transformers (unit: mm)



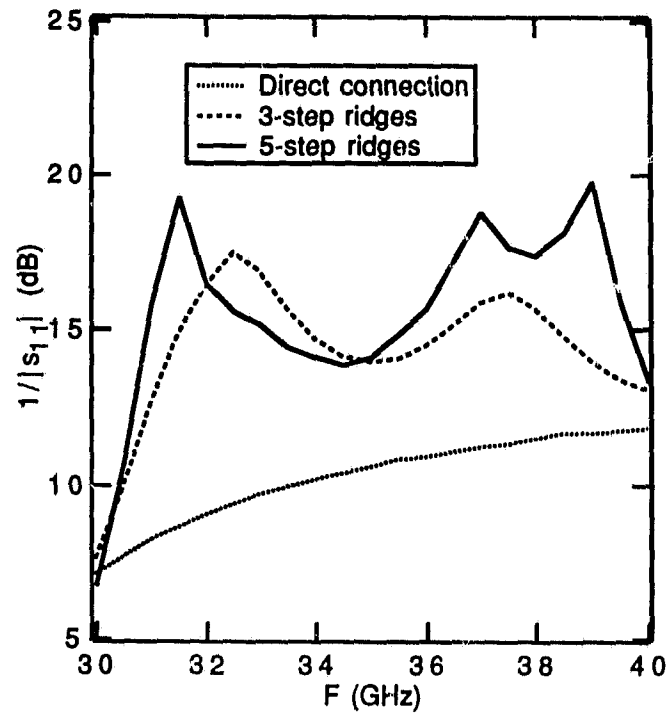
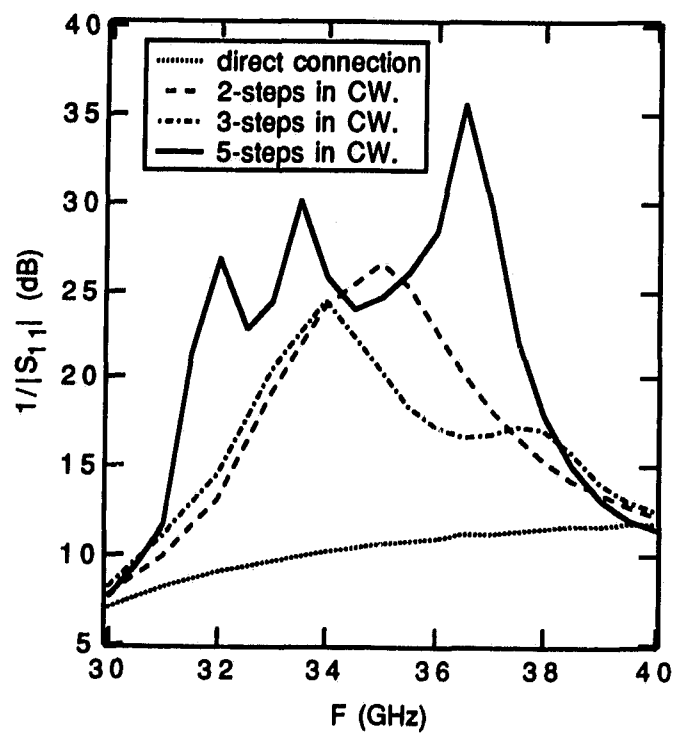


Fig.4.15 Input return loss of the transition shown in Fig.4.12(b).  
( WR-28 and C330 standard waveguides; Ridge thickness  
 $t = 0.2$  mm; For transformer dimensions, see Table 4.1.)



*Fig.4.16 Input return loss of the transition shown in Fig.4.12(c).  
(WR-28 and C330 standard waveguides; For transformer  
dimensions, see Table 4.1.)*

## Chapter 5

# THE FDTLM METHOD IN 3D CYLINDRICAL COORDINATES

### 5.1 Introduction

Cylindrical transmission lines like coaxial lines and circular waveguides find applications where the capability of transmitting or receiving waves having more than one plane of polarization is required. Furthermore, microstrip transmission lines on cylindrical dielectric substrate are of importance as feed lines for radiators on curved surfaces. Therefore, considerable work has been done to develop analysis methods to aid the design of those components. However, microwave discontinuities in 3D cylindrical structures often involve complicated shapes. So far, the theoretical modeling of such structures is still limited to the calculation of propagation characteristics. Furthermore, most of the data available is based on quasi-static analysis and does not taken into account dispersion effects.

As shown in the previous chapters, the FDTLM method is a universal full-wave frequency-domain simulation tool. In this chapter, the FDTLM algorithm is expanded to the cylindrical coordinate system. First, the development of the symmetrical condensed FDTLM node for cylindrical mesh will be exploited. Then, the numerical procedure of the FDTLM algorithm for cylindrical structures is also described. Finally, two applications are presented for s-parameter analysis of microstrip discontinuities on cylindrical dielectric surfaces and the field-theory-based CAD of circular ridged waveguide evanescent-mode bandpass filters.

## 5.2 Cylindrical SCN and FDTLM Algorithm

Fig. 5.1 illustrates a typical cylindrical coordinate system and the location of a single node with interconnecting transmission lines. The dimensions of the node are  $u, \alpha$ , and  $v$  in the  $r, \theta$ , and  $z$  directions, respectively. The approximate differential equations that govern the behavior of voltages and currents at a single FDTLM node are given in time-harmonic form:

$$\begin{aligned}
 \alpha \frac{\partial I_z}{\partial \theta} - v \frac{\partial I_\theta}{\partial z} &= j\omega C_r V_r \\
 v \frac{\partial I_r}{\partial z} - u \frac{\partial I_z}{\partial r} &= j\omega C_\theta V_\theta \\
 u \frac{\partial I_\theta}{\partial r} - \alpha \frac{\partial I_r}{\partial \theta} &= j\omega C_z V_z \\
 \alpha \frac{\partial V_r}{\partial \theta} - v \frac{\partial V_\theta}{\partial z} &= -j\omega L_r I_r \\
 v \frac{\partial V_r}{\partial z} - u \frac{\partial V_z}{\partial r} &= -j\omega L_\theta I_\theta \\
 u \frac{\partial V_\theta}{\partial r} - \alpha \frac{\partial V_z}{\partial \theta} &= -j\omega L_z I_z
 \end{aligned} \tag{5.1}$$

where  $L_r, L_\theta$ , and  $L_z$  are the total inductances associated with the  $r, \theta$ , and  $z$  directed transmission lines and  $C_r, C_\theta$ , and  $C_z$  are the total capacitances.  $I_r, I_\theta$ , and  $I_z$  are the net currents flowing in the  $r, \theta$ , and  $z$  directions. The voltages  $V_r, V_\theta$ , and  $V_z$  are defined to be the total  $r, \theta$  and  $z$  directed voltages at the node. Now the following equivalences are established relating voltages and currents to the electric and magnetic fields:

$$\begin{aligned}
 E_r &\equiv V_r / u & H_r &\equiv I_r / u \\
 E_\theta &\equiv V_\theta / r\alpha & H_\theta &\equiv I_\theta / r\alpha \\
 E_z &\equiv V_z / v & H_z &\equiv I_z / v
 \end{aligned} \tag{5.2}$$

Substituting these into (5.1), the following set of differential equations is obtained:

$$\begin{aligned}
\frac{1}{r} \frac{\partial H_z}{\partial \theta} - \frac{\partial H_\theta}{\partial z} &= j\omega \frac{u}{vr\alpha} C_r E_r \\
\frac{\partial H_r}{\partial z} - \frac{\partial H_z}{\partial r} &= j\omega \frac{r\alpha}{uv} C_\theta E_\theta \\
\frac{1}{r} \frac{\partial}{\partial r} (rH_\theta) - \frac{1}{r} \frac{\partial H_r}{\partial \theta} &= j\omega \frac{v}{ur\alpha} C_z E_z \\
\frac{1}{r} \frac{\partial E_z}{\partial \theta} - \frac{\partial E_\theta}{\partial z} &= -j\omega \frac{u}{vr\alpha} L_r H_r \\
\frac{\partial E_r}{\partial z} - \frac{\partial E_z}{\partial r} &= -j\omega \frac{r\alpha}{uv} L_\theta H_\theta \\
\frac{1}{r} \frac{\partial}{\partial r} (rE_\theta) - \frac{1}{r} \frac{\partial E_r}{\partial \theta} &= -j\omega \frac{v}{ur\alpha} L_z H_z
\end{aligned} \tag{5.3}$$

Comparing equation (5.1) with (5.3) yields the following equivalence between the parameters:

$$\begin{aligned}
C_r &\equiv \epsilon \frac{vr\alpha}{u} & L_r &\equiv \mu \frac{vr\alpha}{u} \\
C_\theta &\equiv \epsilon \frac{uv}{r\alpha} & L_\theta &\equiv \mu \frac{uv}{r\alpha} \\
C_z &\equiv \epsilon \frac{ur\alpha}{v} & L_z &\equiv \mu \frac{ur\alpha}{v}
\end{aligned} \tag{5.4}$$

Then equation (5.3) exactly corresponds to the time-harmonic Maxwell's curl equations, *i.e.*,

$$\begin{aligned}
\nabla \times \vec{E} &= -j\omega\mu\vec{H} \\
\nabla \times \vec{H} &= j\omega\epsilon\vec{E}
\end{aligned} \tag{5.5}$$

In the following, the determination of the node link line parameters and scattering matrix is the same as the section 2.3.3. For example, a characteristic admittance node can be established by assuming that the characteristic admittance of each link line is the same and also equals the intrinsic admittance of the medium occupying the node. The complete scattering matrix of the single symmetrical condensed FDTLM node is shown as follows:



in Fig.5.1(c), always produces elementary cells which are nonuniform, *i.e.* they increase in size away from the centre. Thus the modified time domain stub-loaded SCN is found to be not very useful for such an application, because it would require to have very large stub impedances near the centre and at the outer circumference. This would increase the velocity error and reduce the workable frequency range. It is also noted that when the centre of a cylindrical waveguide needs to be discretized by using the cylindrical mesh, all radial lines are terminated at the centre of the waveguide, which is a circle of infinitesimal small circumference. Therefore, the centre point ( $r=0$ ) is one of the boundary conditions to the  $r\theta$  -plane. In our calculation, this point is usually taken as a short-circuit or open-circuit boundary, depending on the plot of modal field distribution in cylindrical waveguides. For example, for the  $TM_{01}$  mode of a circular waveguide, the center point is the magnetic wall (open-circuit boundary). Whereas for the  $TE_{01}$  mode, the centre point is the electrical wall (short-circuit boundary). If an asymmetrical modal field distribution is formed with respect to the cylindrical centre, the present FDTLM model fails to simulate this case. This is because it is impossible to consider an appropriate boundary condition such as electrical or magnetic wall at such a point. This is unfortunately a limitation of the present model.

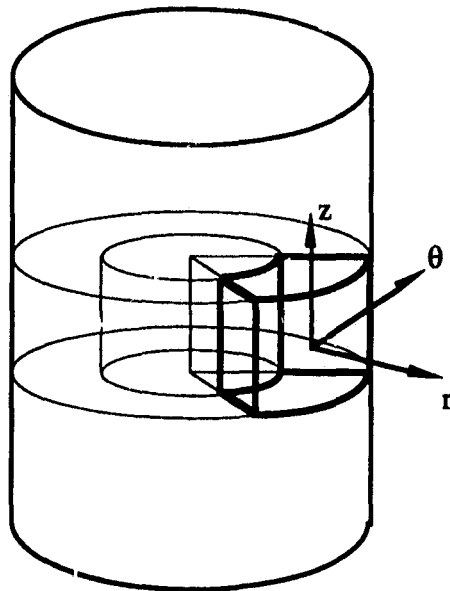


**Fig. 5.1(a)** *The cylindrical coordinate system and location of a node*

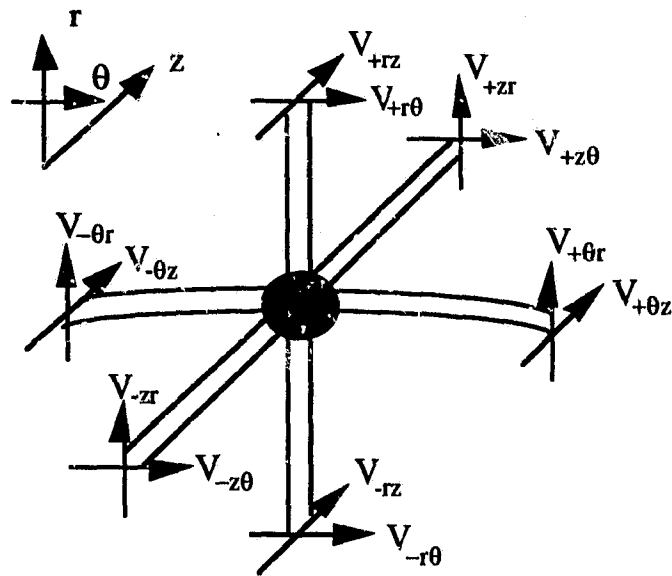


Fig. 5.1(b) Symmetrical condensed FDTLM node for cylindrical geometry

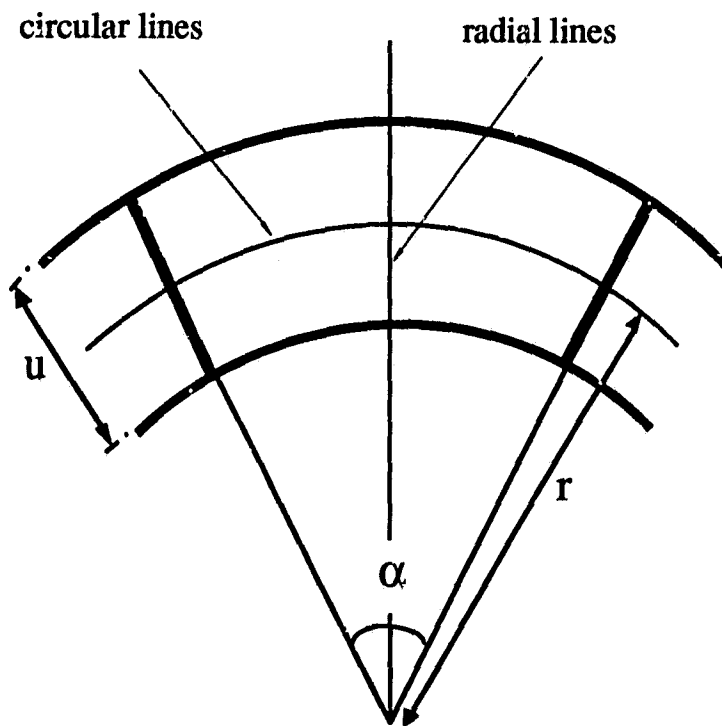


Fig. 5.1(c)  $r\theta$  - plane mesh of the symmetrical condensed FDTLM node

## 5.3 Applications

In the preceding section, we have described how the cylindrical SCN may be used to model the electromagnetic properties of a cylindrical space. The technique has been computer-coded and applied to the problem of determining s-parameters of microstrip discontinuities on cylindrical surfaces and field-theory-based CAD of circular waveguide bandpass filters.

### 5.3.1 Microstrip discontinuities on cylindrical surfaces

Microstrip transmission lines on curved surfaces have found wide application in the design of cylindrical radiating structures. Recently, several novel cylindrical microstrip line structures [33,34] have been proposed for saving dielectric material and reducing conductor losses. However, the work is limited to the calculation of propagation constant and characteristic impedance.

The cylindrical FDTLM algorithm is now utilized to present a rigorous s-parameter calculation of cylindrical microstrip step and gap discontinuities on the same side of the substrate as well as overlay coupling of two microstrip lines on opposite sides of the substrate. The S-parameter extraction technique is the same as in section 3.3.

Fig.5.2 shows the calculated S-parameters of a step discontinuity with different ratios of angles occupied by two strip conductors. The microstrip is deposited on a half-circular rod substrate with radius  $r=2.0$  mm, and relative dielectric constant  $\epsilon_r=12.9$ . Like in a planar structure, the frequency response is quite flat over a wide frequency range. The typical computation time in this case is approximately 15 seconds for one frequency point on a SUN SPARCII station.

Fig.5.3 shows the calculated s-parameters for microstrip step discontinuities which consist of a conductor strip on the surface of a dielectric rod partially embedded in a conducting ground plane. A comparison between Fig.5.2 and Fig.5.3 indicates that the frequency-dependent s-parameters for circular rod substrate is more sensitive when the frequency increases.

Fig. 5.4 shows a gap discontinuity on a substrate with inner and outer radii  $r_1=10.0$  mm and  $r_2=10.635$  mm, respectively. The gap width is  $g=0.2$  mm. Also here the s-parameters behave similar to the structure on a plane substrate.

Fig.5.5 shows the frequency-dependent s-parameters for a transition of magnetically coupled microstrip lines on opposite sides of the substrate. Three different overlap lengths are considered:  $d=0.5$  mm,  $d=1.5$  mm, and  $d=3.0$  mm. As expected, the longer the overlap length the lower the frequency at which the optimum match occurs. For example, for  $d=3$  mm the minimum  $S_{11}$  occurs at about 15GHz, while for  $d=0.5$  mm, it occurs at frequencies higher than 40 GHz.

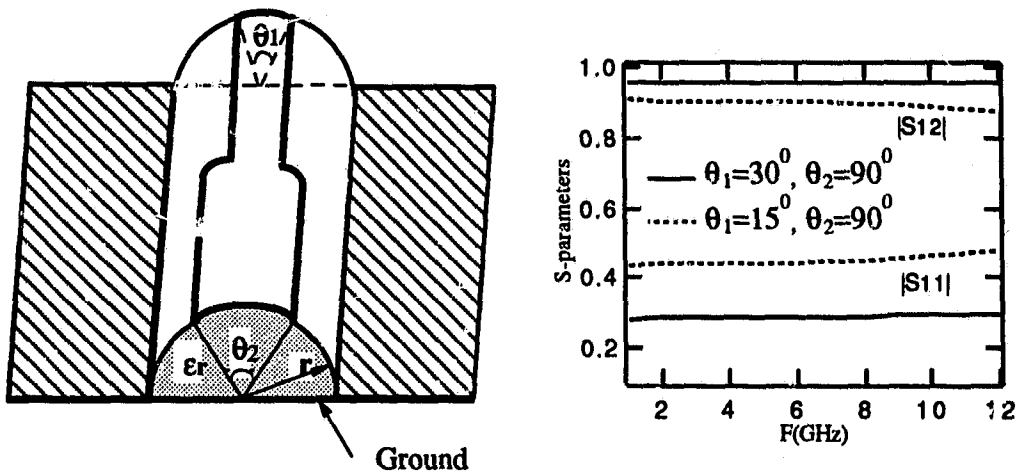


Fig.5.2 Frequency-dependent s-parameters of microstrip step-in-width on a half-circular rod substrate ( $r=2.0$  mm,  $\epsilon_r=12.9$ ).

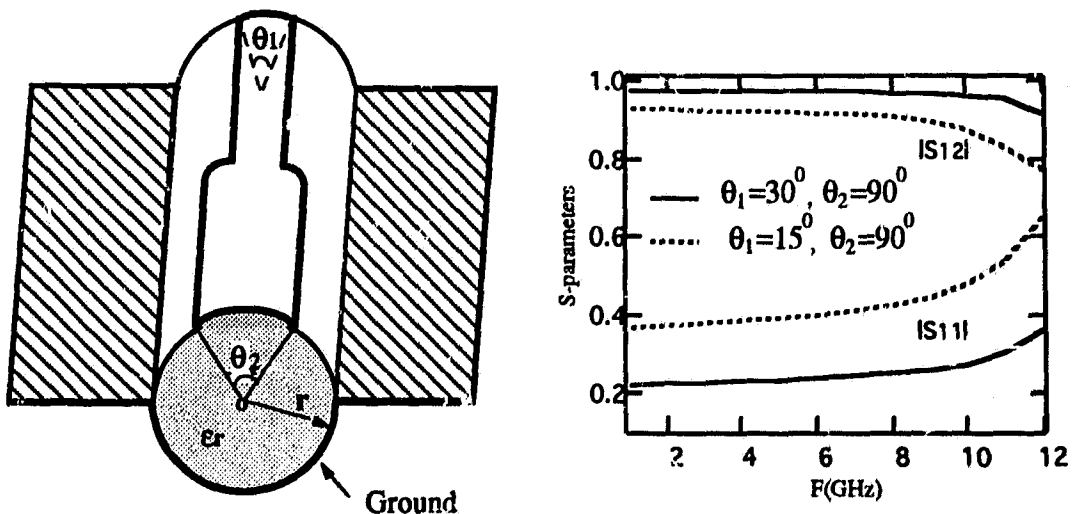
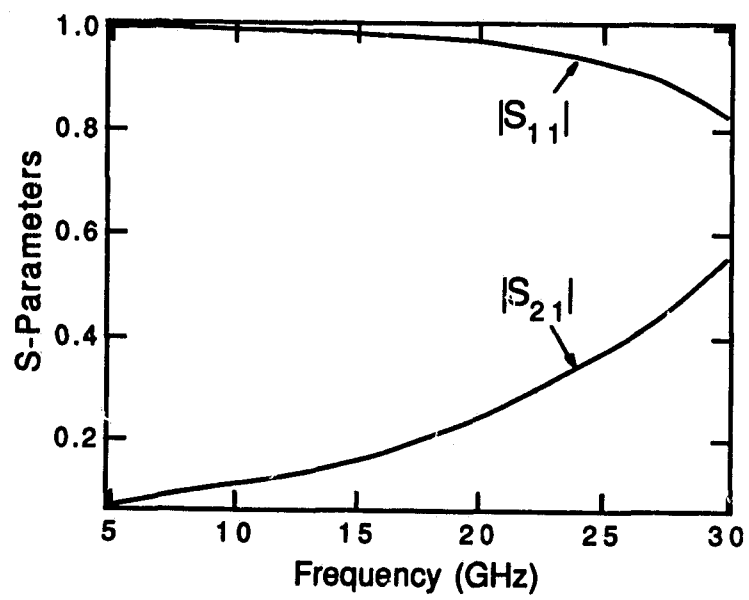
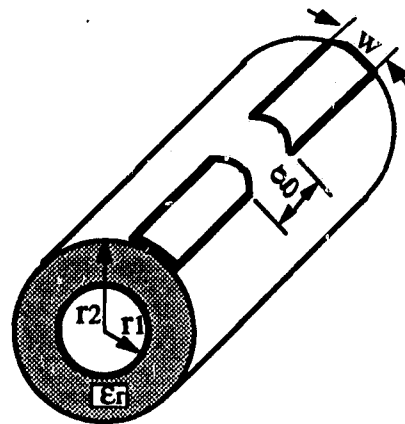


Fig. 5.3 Frequency-dependent s-parameters of microstrip step-in-width on a circular rod substrate embedded in a conducting ground plane ( $r=2.0$  mm,  $\epsilon_r=12.9$ ).



**Fig. 5.4** Frequency-dependent S-parameters of microstrip gap discontinuity ( $r_1=10$  mm,  $r_2=10.625$  mm,  $w=0.635$  mm,  $g=0.2$  mm,  $\epsilon_r=10$ )

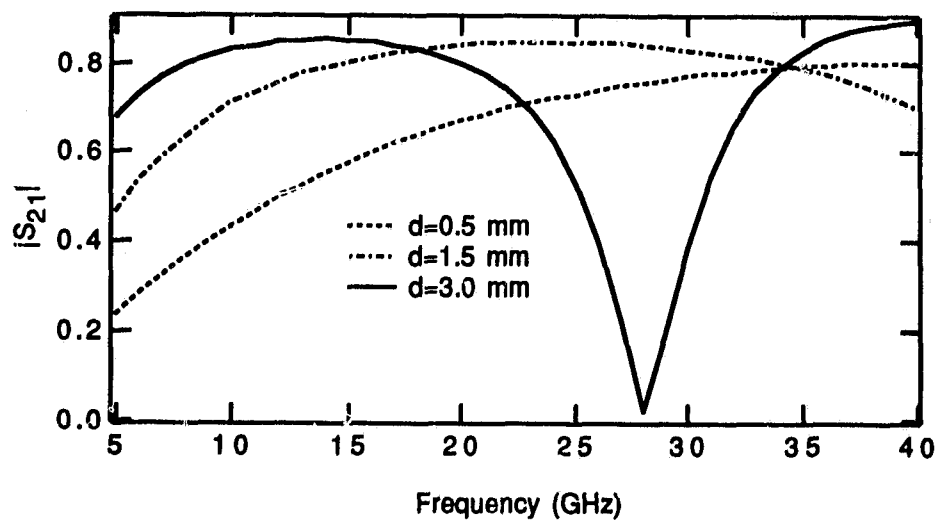
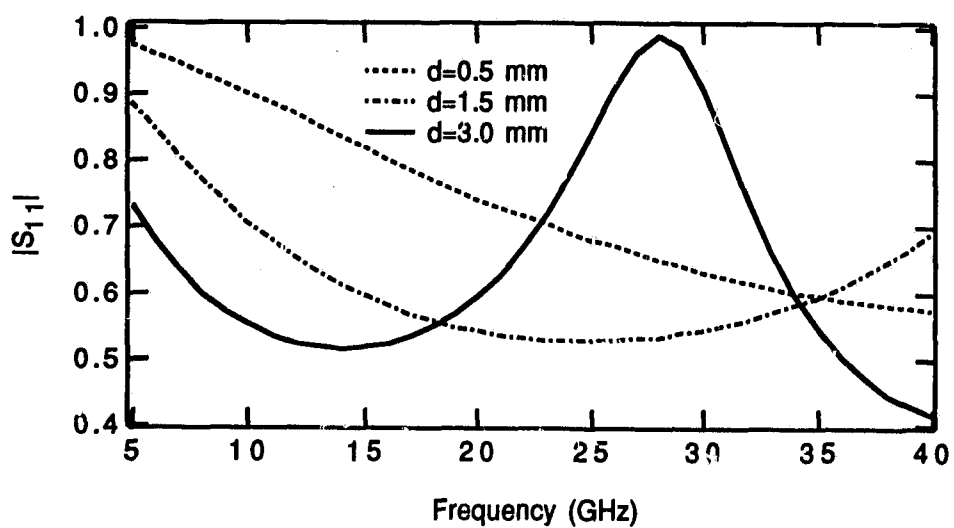
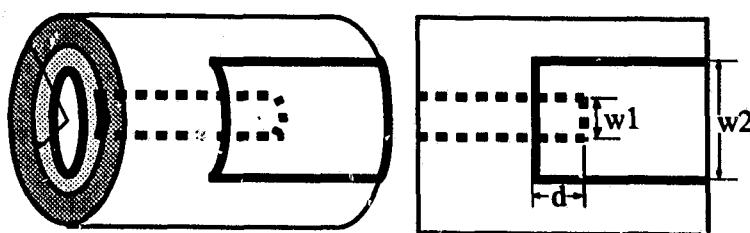


Fig. 5.5 Frequency-dependent S-parameters of microstrip transition on two sides of the substrate ( $r_1=4$  mm,  $r_2=4.25$  mm,  $\epsilon_r=2.2$ ,  $w_1/(r_2-r_1)=1.0$ ,  $w_2/w_1=4.1$ )

### **5.3.2 Field-theory-based analysis of circular waveguide bandpass filters**

Ridged waveguide filters are well known as compact devices with high power handling capability and large passband separation. Although mostly used in rectangular waveguide housings, ridged waveguide filters can also have an advantage when used in circular waveguides. For this application, this section introduces a rigorous field theoretical analysis of circular waveguide bandpass filters. In this approach the circular coordinate system is discretized by a transmission line matrix network. The structures investigated here are symmetrical and the modes can be separated into TE and TM modes. Therefore, only one quadrant of the double-ridged circular waveguide need to be discretized. The centre of the waveguide is implemented by a circle of infinitesimal circumference at which all radial lines are terminated. This circle is taken as a short-circuit or open-circuit boundary, depending on the choice of mode. The filter design is extremely fast and takes into account mode interaction between cascaded discontinuities as well as the finite metallization thickness of the ridges. Furthermore, in comparison to the mode-matching technique, the FDTLM algorithm is extremely flexible because the filter structure can be changed without changing the algorithm.

In order to verify the theoretical approach, a bow-tie shaped [35] metal septum loaded 3-resonator circular waveguide bandpass filter is first calculated and compared with the results from a mode-matching analysis. As shown in Fig.5.6, excellent agreement is found between both methods and measurements[35].

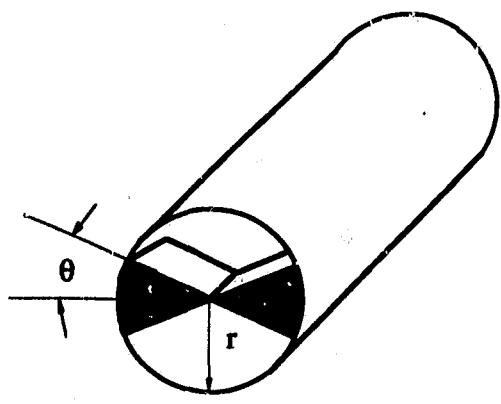
The design of a circular ridged waveguide evanescent-mode bandpass filter follows next. As shown in Fig.5.7, the discontinuities for a complete filter structure can be divided into three sections: the step junction between two circular waveguides with different diameters; the double-ridged circular waveguide; and the below cutoff-circular waveguide. Two semi-infinite waveguides are attached as input and output ports. Firstly, each section of the filter is characterized by its corresponding  $s$ -matrix. Then the overall intrinsic  $s$ -matrix, which characterizes the discontinuity region of the filter, can be determined from these  $s$ -matrices by cascading the individual  $s$ -matrices. Finally,

we establish the relationship between the reflected waves of the two ports and the incident wave at the input port. The corresponding scattering parameters can be obtained from the coefficient matrix relating the reflected and incident waves.

In the Ka-band, the input and output ports of the circular waveguides are 8 mm in diameter. A 4 mm diameter circular waveguide is chosen as evanescent-mode waveguide connecting the resonator ridged waveguide sections. The center frequency is the most important quantity in the design of a bandpass filter. Attention is first directed to how the diameter and width of the single double-ridge and the distance between the edge of the ridge and the step junction affect the centre frequency of the evanescent filter. Fig.5.8 illustrates the effect of changes in the ridge diameter on the center frequency. As known from the rectangular ridge waveguide filter, reducing the ridge diameter increases the center frequency. The inverse effect can be observed in Fig.5.9 when the length of the ridge section increases. Fig.5.10 demonstrates the influence of the distance  $T$  between a single ridged waveguide section and the attached above cutoff waveguide. The closer the ridge section is located to the input waveguide, *i.e.* the stronger the coupling into the resonator sections, the higher the loading and the flatter the resonant curves. It can also be seen from Fig.5.10 that, of course, the resonant frequency changes depending on the loading.

With the data presented above, it is now possible to design a filter. Fig.5.11 shows the calculated response of a filter that consists of three-equal ridge elements in circular waveguide below cutoff. The height of the ridge, the distance from the edge of the ridge to the step junction, and the spacing of the two ridges are the design parameters. Insertion loss is typically below 1dB and return loss is better than 20dB on the average. It is noted that the steepness of the out-of-band insertion loss curve on the higher frequency side is almost equal to the one on the lower frequency side. This happens because the waveguide below its cutoff frequency acts like a lumped reactance.

In general, wider bandwidth and better transmission performance can be achieved by increasing the number of ridges. For a multi-ridge structure, an optimization procedure may be used to optimize the performance of the filter.



3-resonator filter  
 $r=4.0$  mm,  $\theta=2.0$  deg.

Septum length :  $T_1=T_4=0.844$  mm  
 $T_2=T_3=2.985$  mm

Resonator length :  $L_1=L_3=5.683$  mm  
 $L_2=5.768$  mm

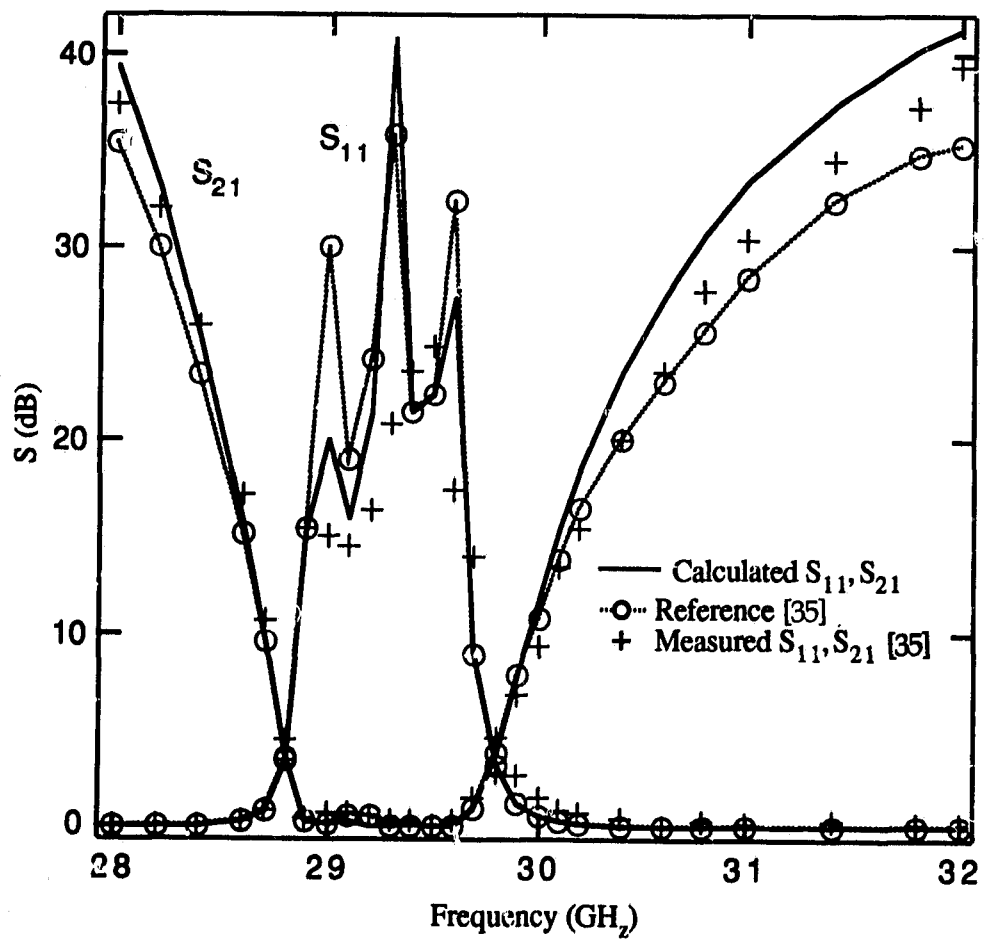
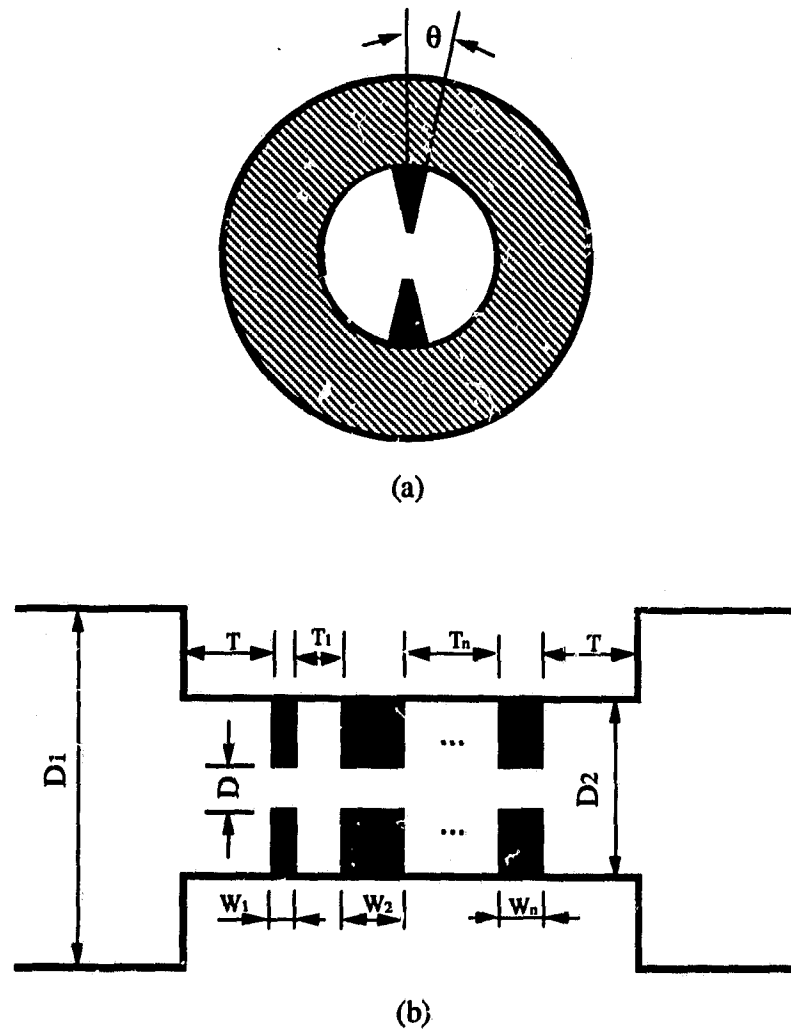
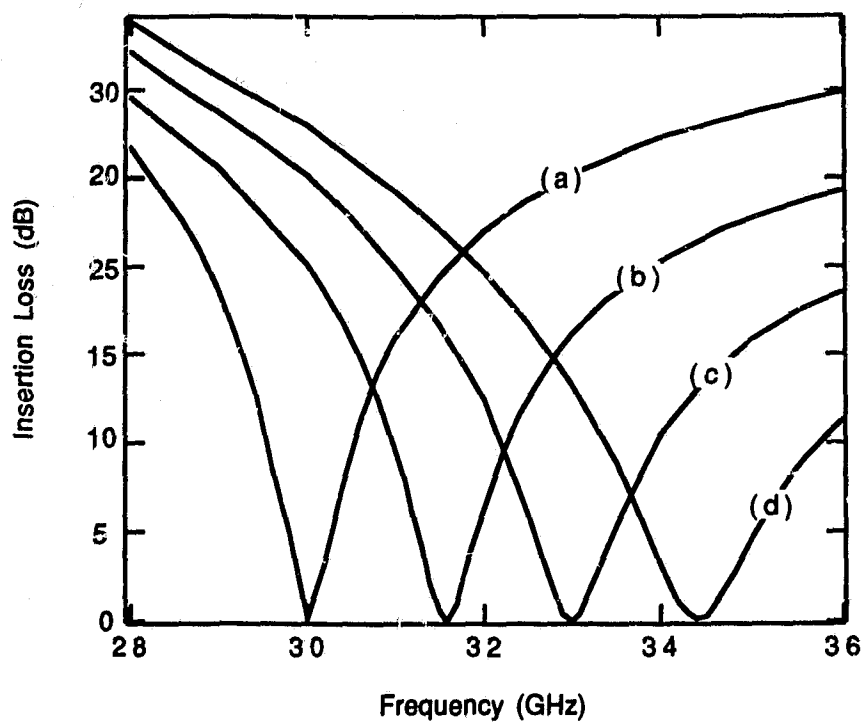


Fig. 5.6 Performance versus frequency of a 3-resonator circular waveguide filter



*Fig.5.7 Evanescent-mode double-ridged circular waveguide bandpass filter  
(a) Cross sectional view; (b) Longitudinal section dimensions.*



**Fig. 5.8** Insertion loss of the filter versus frequency for different diameters  $D$  of the ridge  $D_1=8.0$  mm,  $D_2=4.0$  mm,  $T=2.0$  mm,  $W_1=0.3$  mm,  $\theta=2.0$  deg.; (a):  $D=0.4$  mm, (b):  $D=0.6$  mm, (c):  $D=0.8$  mm, (d):  $D=1.0$  mm.

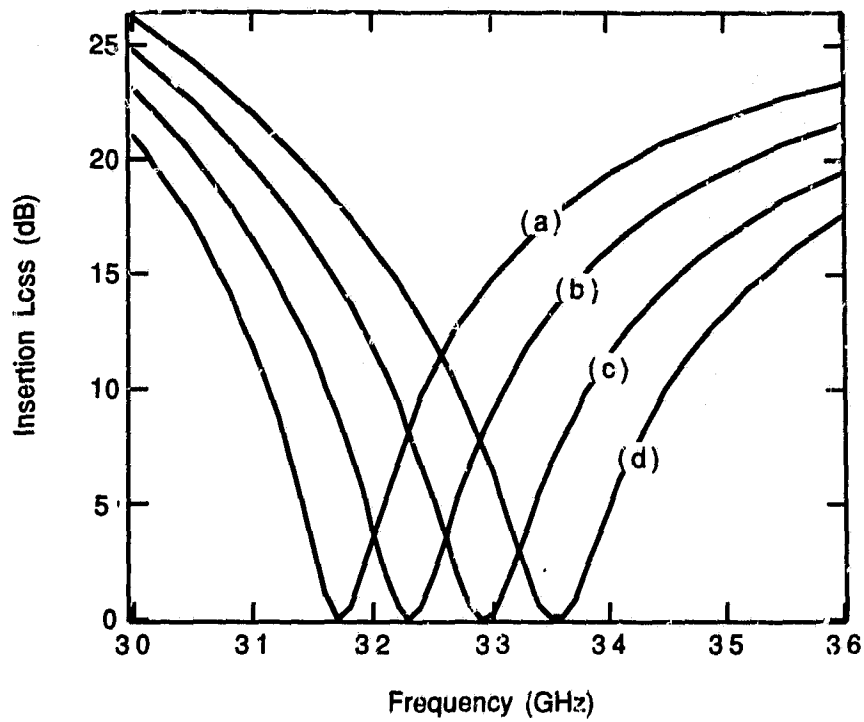
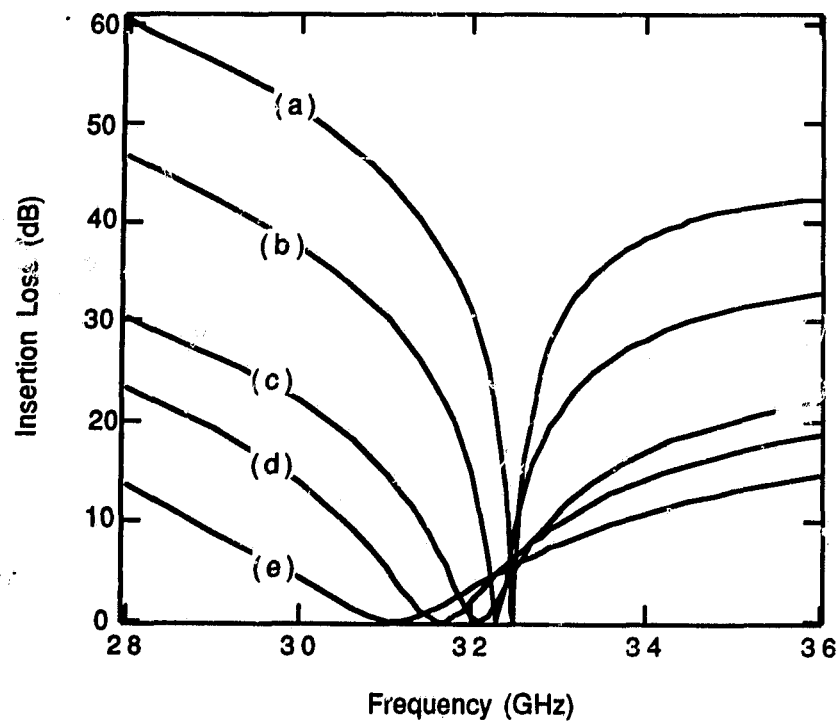
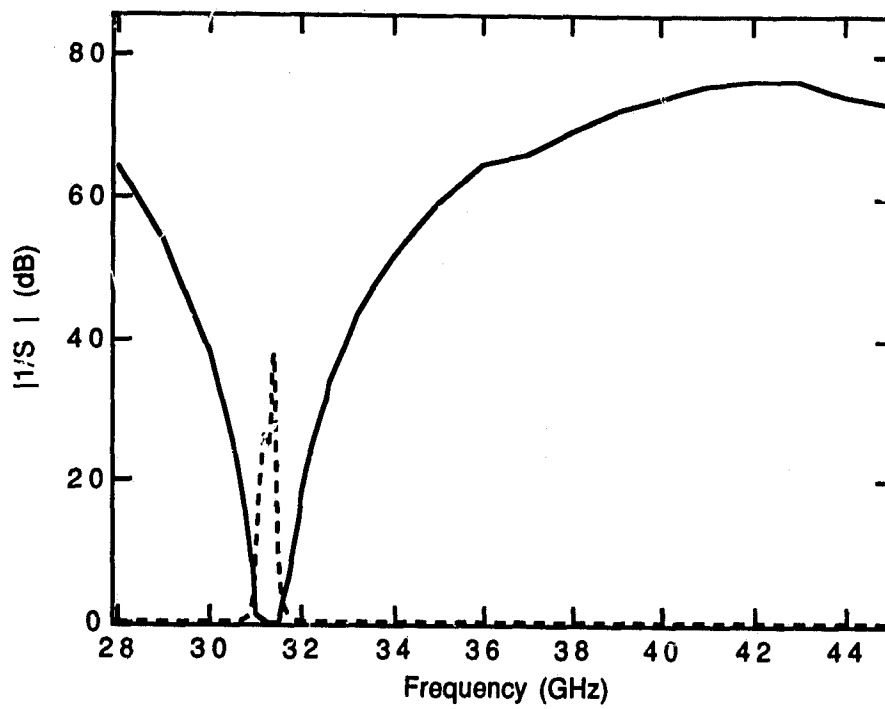


Fig. 5.9 Insertion loss of the filter versus frequency for different widths  $W$  of the ridge.  $D_1=8.0$  mm,  $D_2=4.0$  mm,  $T=2.0$  mm,  $D=0.7$  mm,  $\theta=2.0$  deg.; (a):  $w=0.4$  mm, (b):  $w=0.3$  mm, (c):  $w=0.2$  mm, (d):  $w=0.1$  mm.



**Fig.5.10** Insertion loss of the filter versus frequency for different distances  $T$ .  $D_1=8.0$  mm,  $D_2=4.0$  mm,  $W=0.3$  mm,  $D=0.7$  mm,  $\theta=2.0$  deg.; (a):  $T=4.0$  mm, (b):  $T=3.0$  mm, (c):  $T=2.0$  mm, (d):  $T=1.5$  mm, (e):  $T=1.0$  mm.



**Fig. 5.11** Insertion loss for the evanescent-mode circular waveguide filter loaded with two or three double-ridges ( $D_1=8.0$  mm,  $D_2=4.0$  mm,  $D=0.7$  mm,  $\theta=2.0$  deg.; Three double-ridges:  $T=1.55$  mm,  $T_1=T_2=4.6$  mm,  $W_1=W_2=W_3=0.41$  mm).

## Chapter 6

# CONCLUSIONS

### 6.1 Discussion

The objective of this thesis was to develop a methodology to extend the 3D FDTLM method such that complex electromagnetic structures can be analyzed. This has been accomplished through two main processes. First a new family of frequency-domain symmetrical condensed nodes were developed. The dominant feature of all these nodes is that a local electromagnetic field can be represented on the surface of each node in terms of reflected and incident wave voltages, i.e. each node can be established independently of its environment and described by a scattering matrix. The elements of the node scattering matrix can be derived by using the concepts of energy, voltage and current conservation laws. In order to demonstrate the performance of the different nodes, an accuracy assessment and comparison of the available nodes was performed.

The second goal was to establish the FDTLM algorithm, which is based on the concept of the intrinsic scattering matrix. By establishing the intrinsic scattering matrix, the original large discretized network problem is transformed into the matrix algebra one, and all properties of the structure can be readily computed through matrix operations. This forms the FDTLM algorithm. The algorithm for the eigenvalue problem solution requires only one slice of waveguide which contains only one node in the propagation direction. This technique yields the standard eigenvalue equation which, when solved, provides all modes of interest very efficiently. The eigenvalue equation has inherently good convergence and stability properties even if the number of nodes over the cross-section of the guided structure is increased. This is a very important and advantageous feature of the FDTLM method. For the s-parameter calculation, a novel s-parameter extraction technique for the FDTLM network has been utilized successfully. Furthermore, based on the decoupled symmetrical condensed node technique, a

new FDTLM algorithm has been developed to reduce the computer memory and CPU-time.

To support the main developments outlined above, a general-purpose 3D FDTLM program has been developed such that arbitrarily complicated structures can be simulated with the FDTLM algorithm. This program has great flexibility since only the structure parameters need to be entered into the program. For the 2D eigenvalue problem, two typical structures, the rectangular waveguide filled with a lossy dielectric and the coupled microstrip line on anisotropic substrate, were computed for frequency-dependent dispersion characteristics. Moreover, a routine is added to the general 3D FDTLM program that analyzes the periodic structures in microwave and optical integrated circuits. The rather general corrugated waveguide with plain corrugations and the coplanar slow-wave electrode structure on GaAs substrate have been investigated to confirm the validity and effectiveness of the proposed analysis method.

For the 3D discontinuity problem, several waveguide discontinuities have been investigated. These include: transition between rectangular waveguide to the dielectric slab loaded waveguide of finite length as a simple example; E-plane bandpass filter as cascaded discontinuity problem; microstrip step discontinuity computation as a hybrid mode problem; transition from rectangular to circular waveguides as composite structure problem; and a set of planar transmission line interconnects as mixed discontinuity problem. The objective of all these examples was to demonstrate the applicability and capability of the FDTLM technique to handle rather complex circuit geometries.

Finally, the FDTLM method has been extended to a 3D cylindrical coordinate system. The cylindrical SCN and FDTLM algorithm have also been well established to facilitate modeling of the cylindrical structures. The algorithm has been programmed and applied to the problems of determining s-parameters of the microstrip discontinuities on cylindrical surfaces and field-theory-based analysis of circular waveguide bandpass filters.

In conclusion, the work presented in this thesis is a step towards more efficient numerical computations of general electromagnetic problems in the frequency domain. It represents not only an enhancement and an extension of

previously known works, but also paves the way for a more general solution of the FDTLM method.

## 6.2 Future Research

This thesis has systematically described the FDTLM method. The flexibility, versatility, and generality of this numerical technique has been demonstrated. Although the application of the FDTLM method here has been limited to electromagnetic field problems, many more applications can be found in other fields such as electrical machines, optics, and acoustics.

In order to expand the scope, accuracy, and computational speed of this method, future work should include the following aspects:

- The physical model of the FDTLM algorithm is a large-scale network. In practice the network is sparsely connected by node scattering matrices. Based on this consideration, we can present a solution algorithm suitable to incorporate sparse matrix technique. In sparse matrix computation, operations involving zero are not performed. Thus a significantly faster algorithm than the existing one can be obtained.
- Although the FDTLM algorithm has been developed only for two-port network problems in this thesis, it can also be used to model and solve multi-port network problems.
- The current time-domain TLM algorithm requires that the constitutive parameters  $\mu$ ,  $\epsilon$ , and  $\sigma$  of the medium must be specified as constants, which is a serious limitation. For many media such as water, plasma, and radar-absorbing materials, these parameters will vary significantly with frequency (dispersive materials). In contrast, the FDTLM algorithm will allow the computation of electromagnetic interaction with virtually any material and geometry at a single frequency with sinusoidal wave excitation. Therefore, the extension of the method to include also dispersive materials is straightforward.

## BIBLIOGRAPHY

- [1] P. Silvester and R. L. Ferrari, *Finite Elements for Electrical Engineers*, Cambridge University Press, Cambridge 1983.
- [2] T. Itoh, Ed., *Numerical Techniques For Microwave and Millimeter-Wave Passive Structures*. New York: Wiley, 1989.
- [3] A. R. Mitchell and D. F. Griffiths, *The Finite Difference Method in Partial Differential Equations*, New York: Wiley, 1980.
- [4] K. S. Yee, " Numerical solution of initial boundary value problems involving Maxwell's equations in isotropic media," *IEEE Trans. Antennas Propagat.*, vol. AP-14, pp.302-307, May 1966.
- [5] X. Zhang, J. Fang, and K. K. Mei, " Calculations of the dispersive characteristics of microstrips by the time-domain finite difference method," *IEEE Trans. Microwave Theory Tech.*, vol. MTT-36, pp. 261-267, Feb. 1988.
- [6] A. Christ and H. Hartnagel, " Three-dimensional finite-difference method for the analysis of microwave-device embedding," *IEEE Trans. Microwave Theory Tech.*, vol. MTT-35, pp. 688-696, Aug. 1987.
- [7] P. B. Johns and R. L. Beurle, " Numerical solution of two dimensional scattering problems using a transmission line matrix," *Proc. Inst. Electr. Eng.*, vol. 118, pp.1203-1208, Sept. 1971.
- [8] W. J. R. Hoefer, " The transmission-line matrix method: Theory and applications," *IEEE Trans. Microwave Theory Tech.*, vol. MTT-33, pp. 882-893, Oct. 1985.
- [9] P. B. Johns, " On the relationship between TLM and finite-difference methods for Maxwell's equations," *IEEE Trans. Microwave Theory Tech.*, vol. MTT-35, pp. 60-61, Jan. 1987.
- [10] G. Kron, " Equivalent circuit of the field equations of Maxwell-I," *Proc. IRE*, vol. 32, pp. 289-299, May 1944.
- [11] J. R. Whinnery and S. Ramo, "A new approach to the solution of high frequency field problems," *Proc. IRE*, vol. 32, pp. 284-288, May 1944.
- [12] P. B. Johns, " Use of condensed and symmetrical TLM nodes in computer-aided electromagnetic design," *Proc. IEE, Pt.H*, vol. 133, pp.368-374, 1986.

- [13] P. B. Johns, and K. Akhtarzad, " The use of time domain diakoptics in time discrete models of fields," *Int. J. Num. Methods Eng.*, vol. 17, pp. 1-14, 1981.
- [14] A.C. Cangellaris, C. Lin and K.K. Mei, " Point-matched time domain finite element methods for electromagnetic radiation and scattering", *IEEE Trans. Antennas propagat.*, vol. AP-35, No. 10, Oct. 1987.
- [15] P. P. M. So, Eswarappa, and W. J. R. Hoefler, " A two-dimensional TLM microwave field simulator using new concepts and procedure," *IEEE Trans. Microwave Theory Tech.*, vol. MTT-37, pp. 1877-1884, Dec. 1989.
- [16] H. Jin and R. Vahldieck, " The frequency-domain TLM method - A new concept ", *IEEE Trans. Microwave Theory and Tech.* vol. 40, pp. 2207-2218, Dec. 1992.
- [17] P. B. Johns, " A symmetrical condensed node for the TLM method," *IEEE Trans. Microwave Theory Tech.*, vol. MTT-35, pp. 370-377, April 1987.
- [18] H. Jin, R. Vahldieck and J. Huang, " Direct derivation of symmetrical condensed node from Maxwell's equation using centered differencing and averaging" in *1994 IEEE MTT-S Int. Microwave Symp. Dig.*, pp. 35-38.
- [19] R. Scaramuzza and A. J. Lowery, " Hybrid symmetrical condensed node for the TLM method," *Electron. Lett.*, vol. 26, pp. 1947-1948, Nov. 1990.
- [20] D.P. Johns and C. Christopoulos, " Dispersion characteristics of 3D frequency domain TLM," *Electron. Lett.*, vol. 29, pp. 1536-1537, Aug. 1993.
- [21] J. Huang, R. Vahldieck and H. Jin, " Fast frequency-domain TLM analysis of 3D circuit discontinuities," *In the 9th Annual Review of Progress in Applied Computational Electromagnetics Symposium*, Monterey, CA, March 22-26, 1993.
- [22] A.J.Wlodarczyk, " Representation of symmetrical condensed TLM node," *Electron. Lett.*, vol. 28, pp. 1686-1687, Sept. 1992.
- [23] G. E. Mariki and C. Yeh, " Dynamic three-dimensional TLM analysis of microstrip lines on anisotropic substrates," *IEEE Trans. Microwave Theory Tech.*, vol. MTT-33, pp. 789-799, Sept. 1985.
- [24] H. Jin, R. Vahldieck, J. Huang and P. Russer, " Rigorous analysis of mixed transmission line interconnects using the frequency domain TLM method," *IEEE Trans. Microwave Theory Tech.*, vol. MTT-41, pp. 2248-2255, Dec. 1993.

- [25] A. Sangster and H. McDonald, "An analysis of an abrupt transition from a uniform empty waveguide to a periodically loaded waveguide," *Int. J. Electronics*, vol. 55, No. 2, pp. 213-227, 1983.
- [26] L. Silva and S. Ghosh, "Analysis of rectangular corrugated structures," *IEE Proc. Pt. H*, vol. 138, pp. 335-341, Mar. 1991.
- [27] R. Spickermann and N. Dagli, "Millimetre wave coplanar slow wave structure on GaAs suitable for use in electro-optic modulators", *Electron. Lett.*, vol. 29, pp. 774-775, Apr. 1993.
- [28] H. Chaloupka, "A coupled-line model for the scattering by dielectric and ferrimagnetic obstacles in waveguides," *Arch. Elek. Uebertragung*, vol. 34, pp. 145-151, Apr. 1980.
- [29] J. Bornemann, R. Vahldieck, F. Arndt, and D. Grauerholz, "Optimized low-insertion-loss millimetre-wave finline and metal insert filters," *The Radio and Electronic Engineer*, vol.52, No.11/12, pp. 513-521, 1982.
- [30] N.L. Koster and R.H. Jansen, "The microstrip step discontinuity: A revised description," *IEEE Trans. Microwave Theory Tech.*, vol. MTT-34, pp. 213-223, Feb. 1986.
- [31] B.N.Das and P.Somasekhar Rao, "Analysis of a transition between rectangular and circular waveguides," *IEEE Trans.Microwave Theory and Tech.* vol. 39, pp. 357-359, Feb. 1991.
- [32] Ph.Guillot, P.Couffignal, H.Baudrand, and B.Theron, "Improvement in calculation of some surface integrals: Application to junction characterization in cavity filter design," in *1993 IEEE MTT-S Int. Microwave Symp. Dig.*, pp. 455-458.
- [33] Lei Zhu and E. Yamashita, "Full-wave analysis of strip transmission line on circular dielectric rod," *IEEE Microwave and Guided Wave Lett.*, vol. 2, pp. 478-479, Dec. 1992.
- [34] H.A.Auda, "Cylindrical microstrip partially embedded in a perfectly conducting ground plane", *IEEE Trans. Microwave Theory and Techniques*, vol. 39, pp. 1662-1666, Sept. 1991.
- [35] B.Varailhon de la Filolie, "Field theory analysis of rectangular and circular waveguide discontinuities for filters, multiplexers and matching networks," Ph.D.dissertation, Univ. of Victoria, B.C., Canada, 1992.
- [36] R.A. Pucel, D.J.Masse, and C.P. Hartwig, "Losses in microstrip," *IEEE Trans. Microwave Theory and Techniques*, vol. 16, pp. 342-350, June 1968.

- [37] P. Russer and M. Krumpholz, "The Hilbert space formulation of the TLM method," *International Journal of Numerical Modelling: Electronic Networks, Devices and Fields*, Vol. 6, pp. 29-45, 1993.
- [38] J. Mlakar, "Circuit model for a symmetrical condensed TLM node," *International Journal of Numerical Modelling: Electronic Networks, Devices and Fields*, Vol. 6, pp. 183-193, 1993.
- [39] J. Huang, "The Study of Integrated Finline and Its Circuits," *Thesis of Master Degree*, Southeast University, Jan. 1988.

## Appendix

### Energy Conservation

$$Y_{d1}(a_1^2 + c_1^2) + 2Y_{d6}b_1^2 + 2Y_{d4}d_1^2 = Y_{d1}$$

$$Y_{d1}a_1c_1 + Y_{d6}b_1^2 - Y_{d4}d_1^2 = 0$$

$$Y_{d1}(a_1 - c_1)d_4 + Y_{d4}(a_4 - c_4)d_1 = 0$$

$$Y_{d1}(a_1 + c_1)b_6 + Y_{d6}(a_6 + c_6)b_1 = 0$$

$$Y_{d2}(a_2^2 + c_2^2) + 2Y_{d3}b_2^2 + 2Y_{d5}d_2^2 = Y_{d2}$$

$$Y_{d2}a_2c_2 + Y_{d3}b_2^2 - Y_{d5}d_2^2 = 0$$

$$Y_{d2}(a_2 + c_2)b_3 + Y_{d3}(a_3 + c_3)b_2 = 0$$

$$Y_{d2}(a_2 - c_2)d_5 + Y_{d5}(a_5 - c_5)d_2 = 0$$

$$Y_{d3}(a_3^2 + c_3^2) + 2Y_{d2}b_3^2 + 2Y_{d6}d_3^2 = Y_{d3}$$

$$Y_{d3}a_3c_3 + Y_{d2}b_3^2 - Y_{d6}d_3^2 = 0$$

$$Y_{d3}(a_3 - c_3)d_6 + Y_{d6}(a_6 - c_6)d_3 = 0$$

$$Y_{d4}(a_4^2 + c_4^2) + 2Y_{d5}b_4^2 + 2Y_{d1}d_4^2 = Y_{d4}$$

$$Y_{d4}a_4c_4 + Y_{d5}b_4^2 - Y_{d1}d_4^2 = 0$$

$$Y_{d4}(a_4 + c_4)b_5 + Y_{d5}(a_5 + c_5)b_4 = 0$$

$$Y_{d5}(a_5^2 + c_5^2) + 2Y_{d4}b_5^2 + 2Y_{d2}d_5^2 = Y_{d5}$$

$$Y_{d5}a_5c_5 + Y_{d4}b_5^2 - Y_{d2}d_5^2 = 0$$

$$Y_{d6}(a_6^2 + c_6^2) + 2Y_{d1}b_6^2 + 2Y_{d3}d_6^2 = Y_{d6}$$

$$Y_{d6}a_6c_6 + Y_{d1}b_6^2 - Y_{d3}d_6^2 = 0$$

### Voltage Conservation

$$Y_{d1}(a_1 + c_1) + 2Y_{d6}b_1 = Y_{d1}$$

$$Y_{d2}(a_2 + c_2) + 2Y_{d3}b_2 = Y_{d2}$$

$$Y_{d3}(a_3 + c_3) + 2Y_{d2}b_3 = Y_{d3}$$

$$Y_{d4}(a_4 + c_4) + 2Y_{d5}b_4 = Y_{d4}$$

$$Y_{d5}(a_5 + c_5) + 2Y_{d4}b_5 = Y_{d5}$$

$$Y_{d6}(a_6 + c_6) + 2Y_{d1}b_6 = Y_{d6}$$

### Current Conservation

$$Y_{d1}(a_1 - c_1) + 2Y_{d4}d_1 = Y_{d1}$$

$$Y_{d2}(a_2 - c_2) + 2Y_{d5}d_2 = Y_{d2}$$

$$Y_{d3}(a_3 - c_3) + 2Y_{d6}d_3 = Y_{d3}$$

$$Y_{d4}(a_4 - c_4) + 2Y_{d1}d_4 = Y_{d4}$$

$$Y_{d5}(a_5 - c_5) + 2Y_{d2}d_5 = Y_{d5}$$

$$Y_{d6}(a_6 - c_6) + 2Y_{d3}d_6 = Y_{d6}$$

## VITA

Surname: Huang

Given Name: Jifu

Place of Birth: Jiangsu, China

Date of Birth: July 03, 1960

### Educational Institutions Attended:

University of Victoria, Canada

1991 to 1995

Southeast University, Nanjing, China

1978 to 1987

### Degrees Awarded:

- M.S. in Radio Engineering, July 1987, Southeast University, Nanjing, China  
*Thesis: Integrated Finline and its Applications*
- B.S. in Radio Engineering, July 1982, Southeast University, Nanjing, China

### Honors and Awards:

- Graduate Studies Fellowship, University of Victoria (1992-1993)
- Graduate Teaching Award, University of Victoria (1992-1993)
- Science and Technology Award, China (1990,1991)

### Publications:

- 1) J. Huang and R. Vahldieck, " Fast Frequency-Domain TLM Analysis of 3D Circuit Discontinuities " (Invited Paper), *in the 9th Annual Review of Progress in Applied Computational Electromagnetics Symp.*, Monterey, CA, March 1993, PP.475-481.
- 2) H. Jin, R. Vahldieck, J. Huang and P. Russer, " Rigorous Analysis of Mixed Transmissio. Line Interconnects Using the Frequency-Domain TLM Method", *IEEE Trans. Microwave Theory Tech.*, Vol.41, No.12, Dec. 1993, PP.2248-2255.
- 3) J. Huang, R. Vahldieck, and H. Jin, " A new frequency-domain TLM algorithm using a decoupled symmetrical condensed node ", *in 1994 IEEE MTT-S Int. Microwave Symp. Dig.*, PP. 1535-1538.
- 4) J. Huang and R. Vahldieck, " FDTLM Modelling of slow-wave microwave electrodes on travelling wave electro-optic modulators," *Progress in Electromagnetics Research Symposium*, 24-28 July 1995, Seattle, Washington, USA.

